Tailoring Chirality in Carbon Dots

Florence Victoria

A Thesis

in

The Department

of

Chemistry and Biochemistry

Presented in Partial Fulfillment of the Requirements

For the Degree of Master of Science (Chemistry) at

Concordia University

Montreal, Quebec, Canada

March 2020

CONCORDIA UNIVERSITY

School of Graduate Studies

This is to certify that the thesis prepared

By: Florence Victoria

Entitled: Tailoring Chirality in Carbon Dots

and submitted in partial fulfillment of the requirements for the degree of

Master of Science (Chemistry)

complies with the regulations of the University and meets the accepted standards with respect to originality and quality.

Signed by the final examining committee:

Yves Gelinas   Chair

Chair's Name

Louis Cuccia   Examiner

Examiner's Name

Xavier Ottenwalder   Examiner

Examiner's Name

Rafik Naccache   Supervisor

Supervisor's Name

Approved by   Yves Gelinas

Chair of Department or Graduate Program Director

April 17 2020   Pascale Sicotte

Dean of Faculty

Abstract

Tailoring Chirality in Carbon Dots

Florence Victoria

Carbon dots are an emerging class of fluorescent nanoparticles within the carbon allotrope family. They have garnered significant interest in the field due to their cost-effective and sustainable synthesis, versatile optical and chemical properties, as well as low chemical toxicity. Typically, carbon dots possess a mean size of nearly 10 nm and are comprised primarily of sp^2 carbons alongside oxygen, hydrogen and other heteroatoms. A variety of carbon sources ranging from simple molecules to more complex and heterogenous ones can be used to prepare these dots speaking to their sustainability and cost effectiveness. Their properties and surface chemistry are governed by the synthesis approach and starting precursors allowing us to endow them with various physico-optical properties including chirality, a property of interest due to its ubiquitous nature. Chirality has tremendous implications in drug development and design, as well as in applications such as catalysis, enantioselective recognition and sensing.

In this work, we explore the microwave-assisted synthesis of chiral carbon dots prepared from reactions of the achiral carbon-based molecule, citric acid, and the chiral amino acid, cysteine, in water. The effects of the synthesis parameters on inducing chirality in the dots were investigated in order to tailor the chiral and fluorescent properties of the dots. Separation techniques were used to glean additional insights into the formation mechanism of the dots. Finally, in order to better understand the importance of stereoselectivity in biological systems, we also utilized the chiral carbon dots as potential anti-microbials against various strains of bacteria. Our findings show promising results towards generating new insights and ideas in the field of antibiotics especially given the growing concern of global antibiotic resistance.

Acknowledgements

"Ability is what you're capable of doing. Motivation determines what you do.

Attitude determines how well you do it."

– Lou Holtz

First, I would like to thank my supervisor, Dr. Rafik Naccache, who has always reminded me of my ability through his endless motivation and his positive attitude towards scientific research. I have been incredibly lucky to have had the opportunity to work in his lab under his supervision. He has always guided me through this thesis with an extraordinary effort, support and patience. I will always remember that the "Lab is that way!".

I am also grateful to my committee members, Dr. Louis Cuccia and Dr. Xavier Ottenwaelder for their insightful comments and advice to help progress my project. But I am also thankful for the occasional coffee, sweet treats and yoga tips that I have received throughout the years.

One cannot make this far without the help of some wonderful and supportive lab technicians, administrative staff, fellow lab mates and friends. Thank you all for making this an enjoyable and memorable journey. I'd especially like to thank my friends, Tayline de Medeiros and Alexia Macina who have always been there for me, whether it was inside or outside the lab. I am forever grateful for your friendship.

Finally, I would like to thank my mom, my dad and my brother. Words cannot express the gratitude I have towards them. Thank you for always encouraging me when I was doubtful, for always loving me when I was being difficult and for always supporting me to achieve my best. I am who I am because of you.

Contribution of Authors

The work in chapter 3.4 was carried out in collaboration with Ms. Liana Zaroubi and Dr. Brandon Findlay at Concordia University.

Table of Contents

List of Figures

List of Tables

List of Appendix Figures

List of Abbreviations

1 D- CYS : 2 CA	1 D-Cysteine : 2 Citric Acid - Carbon Dots
1 D-CYS : 1 CA	1 D-Cysteine : 1 Citric Acid - Carbon Dots
1 L-CYS : 1 CA	1 L-Cysteine : 1 Citric Acid - Carbon Dots
1 L-CYS : 2 CA	1 L-Cysteine : 2 Citric Acid - Carbon Dots
2 D-CYS : 1 CA	2 D-Cysteine : 1 Citric Acid - Carbon Dots
2 L-CYS : 1 CA	2 L-Cysteine : 1 Citric Acid - Carbon Dots
CDs	Carbon Dots
cysCDs	Cysteine-Citric Acid Carbon Dots
D-cysCDs	D-Cysteine-Citric Acid Carbon Dots
FT-IR	Fourier Transform Infrared Spectroscopy
L-cysCDS	L-Cysteine-Citric Acid Carbon Dots
MIC	Minimal Inhibitory Concentration
ROS	Reactive Oxygen Species
TEM	Transmission Electron Microscopy
TGA	Thermo Gravimetric Analysis
XPS	X-ray photoelectron Spectroscopy
XRD	X-ray Powder Diffraction

Chapter 1: Introduction

1.1   The Nanoscale World

1.1.1   Defining "Nano"

We exist in a macroscopic world but within it exists a smaller nanoscale domain; objects within this size range are undetectable to the human eye. In 1947, the prefix "*nano*" was inaugurated at the Union Internationale de Chimie to mean a unit that is one billionth part of a given measurement (10^{-9}). Objects within the nanoscale are even smaller than microscopic red blood cells and bacteria; a singular red-blood cell or bacterium are over 1000 nm in size.[1,2] To further contextualize this definition, a strand of human hair is approximately 60,000 nanometers wide (Figure 1), highlighting how staggeringly small objects within the nanoscale are. However, even though the discovery of nanosized objects was only realized in recent decades, their uses in human civilization can be traced many centuries and millennia ago.
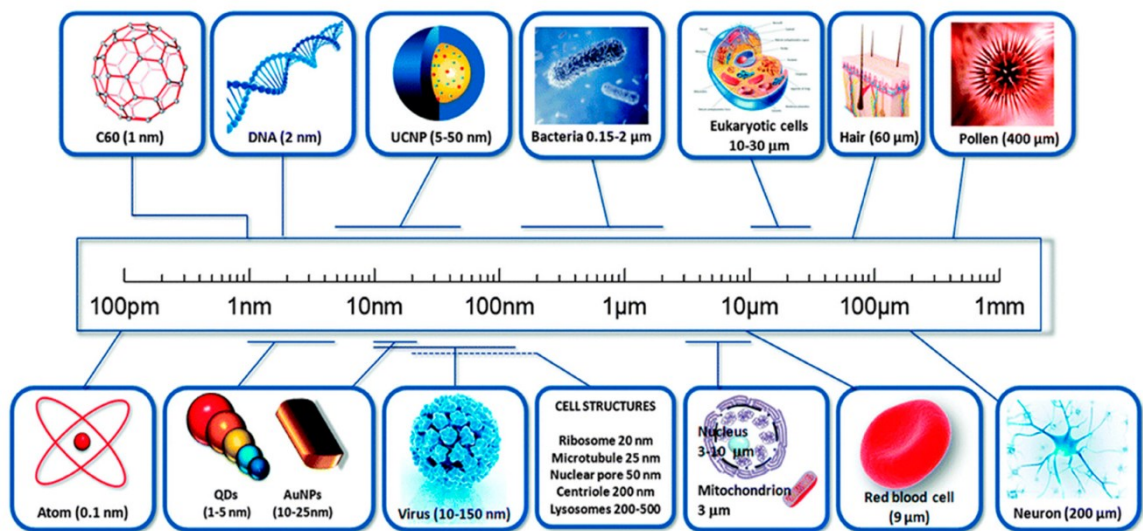
Figure 1. A perspective of the nanoscale. Macroscopic objects like human hair and microscopic biological molecules like red blood cells highlight the minuscule scale of nanosized objects. (Bayda et al., Molecules, 2019, 25, 112.)

1.1.2 The Historical Past of "*Nano*"

In the modern-day world, the word "*nano*" has gained universalization primarily due to its popularity in the technology and cosmetic industries and with the emergence of products and services such as the iPod nano and nano-emulsions. Of course, the iPod nano is not in itself a nanosized music player, but it does certainly house highly miniaturized nanoscale electronics. However, nanotechnology has existed long before the term was invented, dating back to 4th century Rome. The Lycurgus Cup is a prime example of the historic use of nanotechnology.[1–4] The cup is constructed from dichroic glass such that it appears green in the absence of light; however, when light shines through the cup, it is a translucent red colour (Figure 2a, b). The shift in appearance observed in the dichroic glass is generated by the
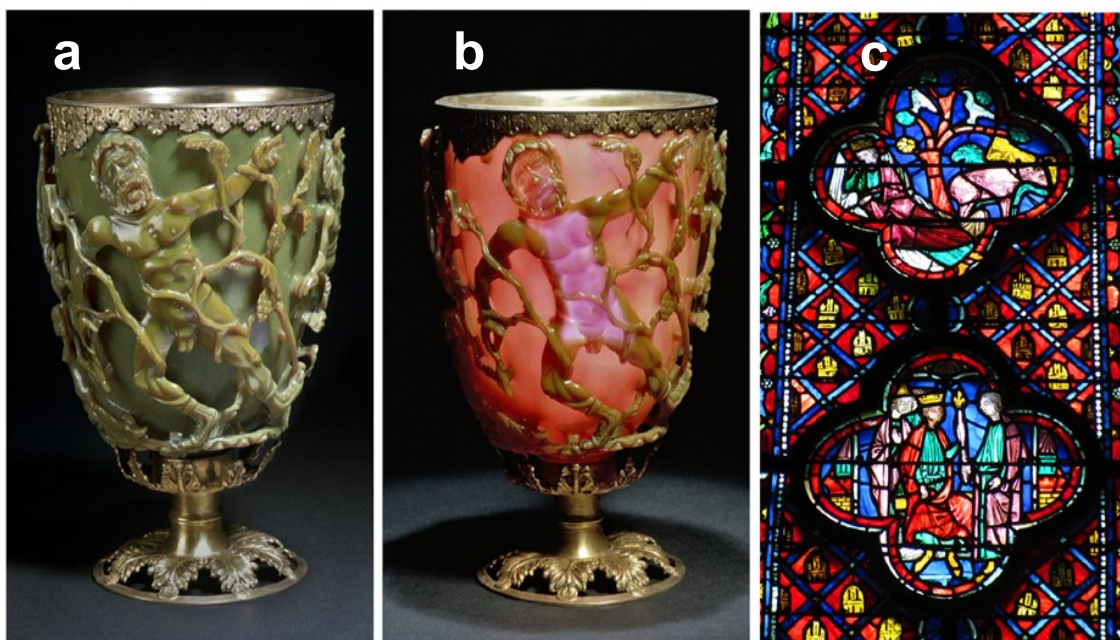
Figure 2. Historical examples of nanotechnology. The Lycurgus Cup fabricated in ancient Rome is one of the earliest findings. It appears to be an opaque green cup (a) however, when light shines through the cup, it becomes a translucent red (b). The colour of the cup changes as the process required to fabricate the cup introduced a dispersion of metallic nanoparticles. Later, this technique of nanoparticle incorporation was used to create artistic stained glass in European cathedrals (c). (Bayda et al., Molecules, 2019, 25, 112.)

various metallic nanoparticles dispersed in the glass. Centuries after its construction, an analysis of the cup by an atomic force microscope revealed that it was comprised of silver, gold and copper nanoparticles with sizes up to 100 nm. The appearance of the green colour within the cup is caused by light scattering of larger colloidal silver nanoparticles, whereas the shift to red occurs following absorbance of light by the gold nanoparticles in the cup at a wavelength of approximately 520 nm. During the 10th century and onwards, the concept of incorporating metallic nanoparticles in materials was exploited to obtain luster in ceramics and the colorful stained glass in many European cathedrals (Figure 2c).

More recently, the concept of the term "*nano*" stems from the annual American Physical Society meeting in 1959, where physicist and Nobel Prize Laureate Richard Feynman gave his famous talk "There's Plenty of Room at the Bottom."[1–5] Feynman believed that circuits, microscopes and computers could be miniaturized and manipulated on an atomic scale. Due to these revolutionary ideas, Feynman is considered to be father of modern nanotechnology. In 1974, Norio Taniguchi, a Japanese scientist, coined the term nanotechnology to describe the findings of his research on semiconductors in the nanoscale.[6] The revolutionary research and ideas by Professor Taniguchi and Rich Feynman created the field of nanotechnology and inspired the discoveries of the scanning tunneling[7] and atomic force microscopes,[8] allowing scientists to visualize and manipulate single atoms. These findings validated Feynman's beliefs, influencing and promoting the growth of nanotechnology as we know it today.

1.1.3 Nanotechnology, Nanomaterial, Nanoparticle?

Nanotechnology is defined as the control of science, technology and engineering of nanoscaled materials. The terms nanomaterial and nanoparticle are often used interchangeably because their definition is quite broad and often refers to objects (particles, materials, crystals, *etc.)* that are smaller than 100 nm in a single dimension.[1–3] Nanoparticles have gained significant interest, in the past two decades, from researchers due to their many unique properties, which often differ

from the bulk phase. These unique properties have been found to be useful in a myriad of applications such as biomedicine,[9–11] environmental science,[12,13] catalysis[14,15] and optoelectronics,[16,17] among others.

1.1.4 Nanoparticle Properties

Nanoparticles exist in various shapes and sizes with diverse electronic, optical, magnetic, physical and chemical properties; however, the different types of nanoparticles are unified by the fact that their properties are determined by their reduced size.[4,18–20] These size-dependent properties include but are not limited to optical properties, magnetism and increased surface area to volume ratio.

For example, metallic gold that makes up jewelry is bright, yellow and lustrous. However, colloidal dispersions of gold nanoparticles posses' unique optical properties absent from the bulk phase (*i.e.* μm and beyond) (Figure 3). The classic example of such properties is the Lycurgus Cup containing a dispersion of gold nanoparticles in its glass (Figure 2 a, b). The emergence of such optical properties is caused by the interaction of the gold nanoparticles with the oscillating electromagnetic wave known as surface plasmon resonance.[21] The interaction of the light at specific wavelength causes the electrons in the surface of the nanoparticle to oscillate in an aligned manner and enhance optical properties such as absorbance of the nanoparticle. Interestingly, the optical properties of these colloidal dispersions can be tuned according to their size and shape, aspect ratios (ratio of the length versus the width in the case of nanorods), as well as shell thickness in the case of core/shell nanoparticles (Figure 3). The changes in physical attributes impact the absorption spectra of the nanoparticles, which in turn impacts their optical properties.[18] Gold nanospheres prepared at a size of ~15 nm absorb light at 525 nm, while an additional 30 nm in the diameter red-shifts their absorption to 575 nm. [20,22] The same can be observed for nanorods where the optical properties can be tuned from 500 to 1500 nm by varying the aspect ratio during synthesis.[22]
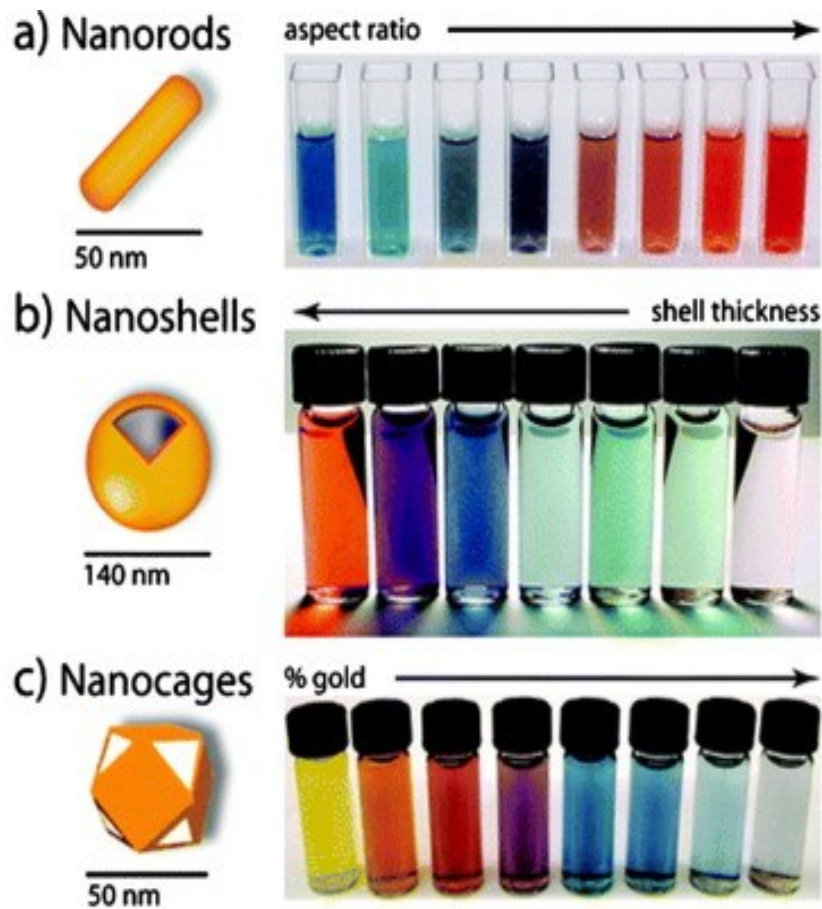
Figure 3. Morphology dependant properties of gold nanoparticles. Gold nanoparticles, unlike their bulk counterpart, can change the colour of their dispersion depending on their size and shape. The colour of the gold nanoparticle dispersion is tuned by varying the aspect ratio (a), shell thickness (b) and percentage of gold (c). The colour changes as a result of a change in the absorption properties of the nanoparticle. (Khan et al., J. Chem., 2019, 12, 908–931.)

Not only can a multitude of optical properties be derived from these reduced size materials, they have also been shown to enhance electromagnetic properties such as paramagnetism.[4,18] At the macroscale, ferromagnetic materials, such as iron and iron (III) oxide, are attracted to magnets and form permanent magnets.[23] But ferromagnetism is temperature dependent, at temperatures greater than the Curie temperature, they become paramagnetic. As such, they become weakly magnetic and are only magnetic in the presence of externally applied magnetic field. Nanoparticles from ferromagnetic materials such as iron (III) oxide become

superparamagnetic such that they exhibit enhanced qualities of paramagnetism even at temperatures lower than the Curie temperature.[4,18]
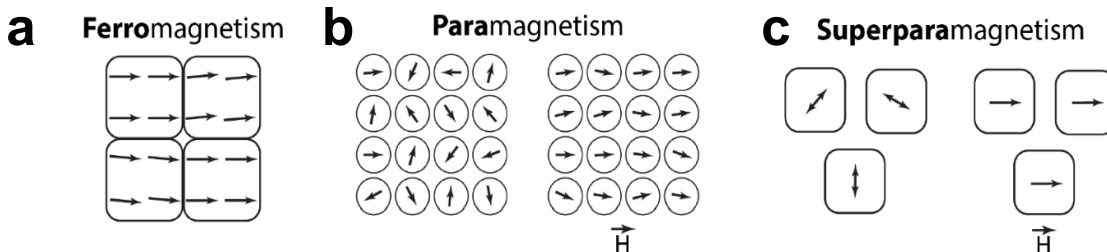
Figure 4. The different types of magnetism. Ferromagnetism are materials that contain dipoles arranged spontaneously into magnetic domains (as shown by the squares) (a). Even in the absence of an externally applied magnetic field, they are easily attracted to magnets and form permanent magnets (a). Paramagnets are materials with dipoles but lack domains; furthermore, they require an external magnetic field to act as weak magnets (b). Superparamagnetism is a property of ferromagnetic nanomaterials that due to its size contain a single magnetic domain (c). In the absence of an external magnetic field, this domain alternates spontaneously; however, in the presence of a field, it can become magnetised. (M. Bloemen, Katholieke Universiteit Leuven, 2015.)

This phenomenon occurs due to the arrangement of the dipole moment in the nanomaterial. Typically, bulk ferromagnetic materials are made up of dipoles that spontaneously align with each other into magnetic domains in a uniform direction (Figure 4a).[23] But bulk paramagnetic materials lack this spontaneous ordering of its dipole unless they are subjected to an external magnetic field (Figure 4b). At the nanoscale, as size decreases, materials possess one single magnetic domain (Figure 4c). This single domain can rapidly alternate the direction of its dipole such that it appears as non-magnetic. However, in the presence of an externally applied magnetic field, these magnetic nanoparticles can behave like paramagnets with a greater degree of magnetization under a weaker magnetic field. Furthermore, the paramagnetic nature of nanomaterials occurs at temperatures lower than the Curie temperature and as such, superparamagnetic nanomaterials have been touted as having potential uses in biological applications including MRI imaging agents in medical diagnostics, [24–27] and drug delivery.[24,25,28]

A fundamental property of nanomaterials is their high surface area to volume ratio (Figure 5).[4,18–20] At the nanoscale, materials with same volume as a single macroscale material possess a significantly larger surface area. For example, a cube of 1 cm in size has a volume of 1 cm^3 and surface area of 6 cm^2. If the same cube was halved in size, so it was 0.5 cm, it would have a volume of 0.125 cm^3 surface area of 1.5 cm^2. In order to obtain a volume of 1 cm^3, we would need 8 cubes with 0.5 cm in dimension and these cubes would result in a total surface area of 12 cm^2. Now imagine the same cube with dimension of 1 nm, it would have a volume of 1 x 10^{-21} cm^3 and a surface area of 6 x 10^{-14} cm^2. So once again to obtain a volume of 1 cm^3, we would need 1 x 10^{21} cubes with 1 nm in dimension and these cubes would result in a total surface area of 6 x 10^7 cm^2 (60 million cm^2). The increased surface area of the nanoparticles results in many advantages and have been largely studied and exploited in several fields of research.[4,18,20] With such properties, only a small quantity of nanoparticles is required for many biological[9–11] and catalytic applications.[14,15]
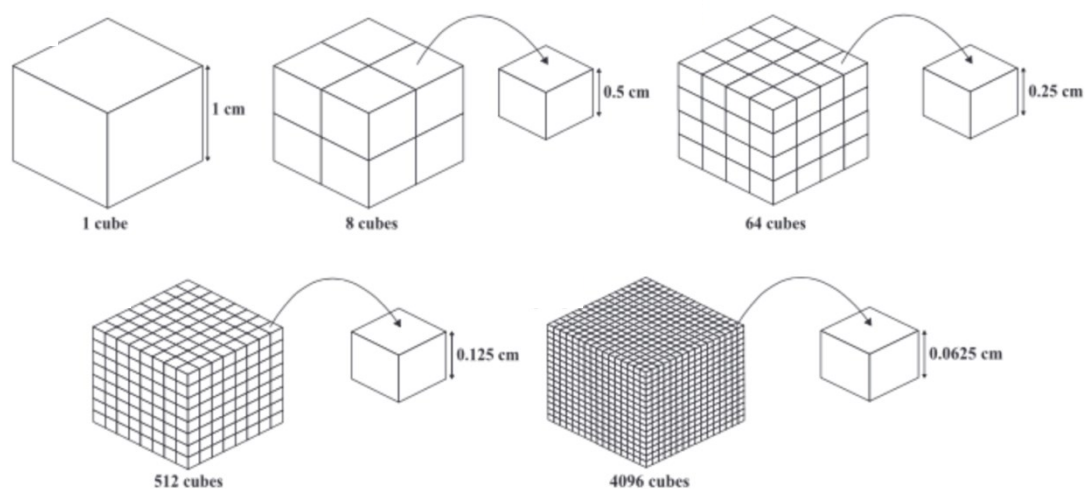
Figure 5. The effect of size on surface area. As the size of a material is decreased, the ratio of its surface area to volume increases. So, for the same volume of a macroscopic material, nanoparticles have a much larger surface area. (M. Loos, Elsevier, 2015, pp. 1–36.)

Apart of shape and size, nanoparticle properties are also dictated by their composition.[4,18,19] Nanoparticles are often classified by their composition be it metallic (*e.g.* quantum dots, lanthanides, metal nanoparticles), organic (*e.g.* polymer nanoparticles, graphene, carbon dots, carbon nanotubes) or hybrids thereof often comprised of core/shell structures. As such, these materials can be prepared from a myriad of elements present in the periodic table with combinations that can offer tremendous possibilities including the ability to endow materials with novel properties that were often observed only at the molecular level.

1.2 The Chiral World

1.2.1 Defining Chirality

One such novel property in nanoparticles is chirality. In the simplest definition, chirality is a geometrical property of objects where an object and its mirror image are non-superimposable due to their spatial arrangement (Figure 6a). [29–32] The term chirality originates from the Greek word *χείρ (cheir)* for hand, as such, the classic example of chiral objects are our very own hands (Figure 6b). Chiral objects lack a plane of symmetry or a center of symmetry. So, a carbon molecule is considered to be chiral if it is connected to four different groups.

Two mirror-image molecules are known as enantiomers, or optical isomers, because they are composed of the same elements with the same connectivity.[29–32] Enantiomers differ only in the arrangement of their bonds in the 3D orientation. Therefore, chiral molecules have the same chemical and physical properties such as boiling point, melting point, polarity, density *etc.* However, they have a different optical activity, such that it is equal and opposite in magnitude. This is a consequence of the enantiomers interacting differently with plane-polarized light and the electric field.
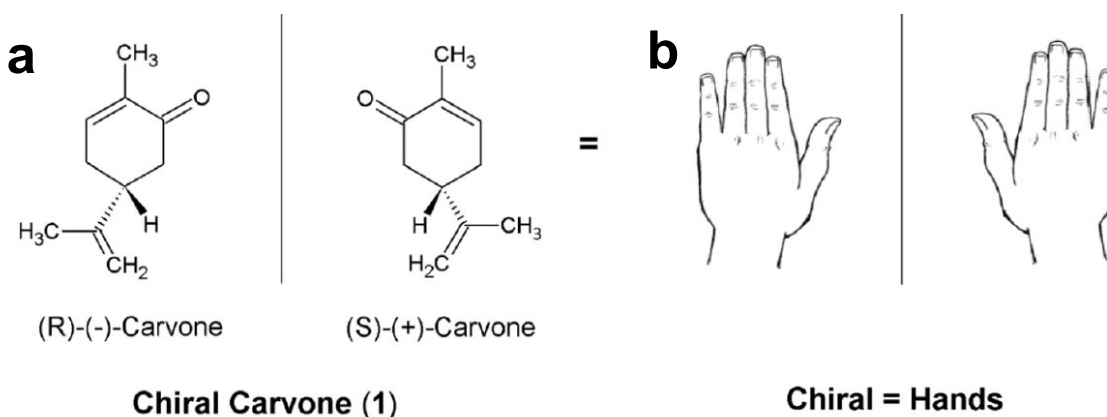
Figure 6. Mirror images. Carvone is a chiral essential oil (a), the enantiomers are mirror images to each other like the two hands (b). The chemical composition of the enantiomeric oils is identical; however, the 3-D orientations are opposite. (Sadgrove et Jones, Agriculture, 2015, 5, 48–102.)

1.2.2 Discovery of Chirality

These astonishing characteristics of chirality has always left scientists pondering its origins. It is safe to say that chirality has existed since the beginning of time and its origin remains of one of world's greatest mysteries. Chirality was first stumbled upon by French physicist and astronomer Jean-Baptiste Biot in 1815. Biot discovered that some natural compounds such as camphor, turpentine, sucrose, and tartaric acid were optically active.[29,30,33,34] He also hypothesized that this optical activity was due to some molecular property specific to these molecules. Later in 1848, French chemist Louis Pasteur discovered molecular chirality through his works in crystallography and optical rotation. Pasteur confirmed Biot's thoughts on molecular chirality by being the first to resolve both enantiomers of the chiral molecule, tartaric acid.[35] Pasteur's experiments and discoveries are considered to be one of the greatest in the history of chemistry.

1.2.3 Importance of Chirality

Since the origins of chirality still remain a mystery, it has evoked the question "*why is life homochiral*?". All living systems are composed of : left-handed amino acids that make up proteins and enzymes; right-handed sugars that construct the backbone of DNA; and DNA that codes for all biological information coiling into right-handed helices (Figure 7).[29,31] Therefore, chirality and stereochemistry contribute to a major role in biochemical recognition including smell and taste, in chemical communication, in signaling pathways and in enzymatic reactions.

For example, the enantiomers of the molecule carvone have identical physical and chemical properties (Figure 6 a). [36] They are both pale yellow essential oils that are insoluble in water and glycerol. The boiling point of these compounds are 230 ºC and they have a specific gravity of 0.96 at 20 ºC. But the receptors in our nose are able to detect the different stereochemistry in the chiral molecules, (+)- carvone is known to smell like caraway and (-)-carvone is known to smell like spearmint.
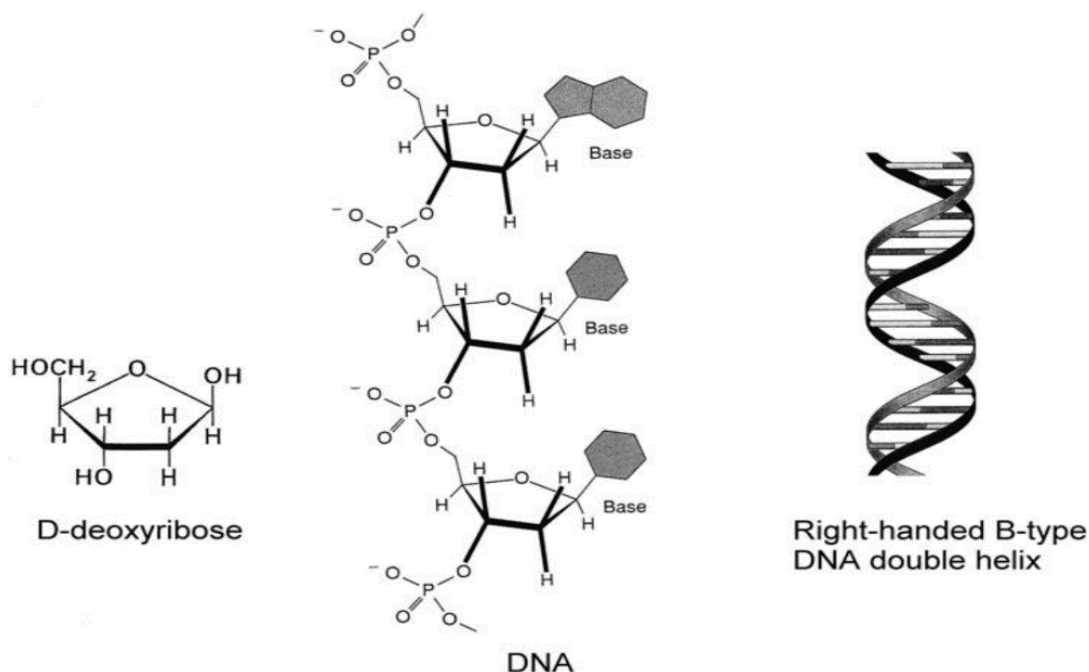
Figure 7. Chiral biological molecules. One of the greatest mysteries in science is the evolution of a homochiral world. Chirality is found everywhere, even within us, in the twists of our DNA and in the stereochemistry of sugars that make-up our DNA. (Barron, Space Sci. Rev., 2008, 135, 187–201.)

As receptors and enzymes in our body are stereospecific, chirality has a significant impact in the pharmaceutical industry.[37,38] A tragic incident occurred in the 1960s, pregnant women were prescribed thalidomide, a chiral drug to reduce morning sickness. However, only one of enantiomers, the (R)-enantiomer had the desired effect. The other (S)- enantiomer caused birth defects underlining the importance of chirality in drugs. Thalidomide is not an uncommon example of a chiral drug. In fact, over 50% of pharmaceutical drugs exist as chiral compounds. In such chiral molecules, only one of the enantiomers exhibits the desired pharmacological activity while the other enantiomer often has adverse effects or reduces the efficacy of the drug.

1.3   Chirality in Nanoscale

1.3.1   Chirality Through Templates

In light of the above, the importance of chirality has also been explored in the nanoscale. What drives scientists around the world to further explore this property is the new dimension of selective interactions that these chiral nanoparticles would offer in biomolecules, in nanodevices and in asymmetric catalysts, among others.[39–41]

Chirality has been explored in various classes of nanomaterials including metallic and semiconductor nanoparticles, as well as polymeric and carbon-based nanosystems. One of the common methods to induce chirality, at the nanoscale, is through chiral organization[39,40]. These methods often use chiral templates to adhere nanoparticles creating an overall chiral structured nanomaterial. DNA is often used as the scaffold to create such nano-chiral systems where it is formed into pyramids[42] or helical structures (Figure 8).[39,43] The nanoparticles are then functionalized to these structures using linkers on the nanoparticle or through modifications in the DNA itself as can be observed in the example with gold nanoparticles in Figure 8.

Similarly, chiral organic ribbons have also been used as a scaffold to attach semi-conducting cadmium sulfide nanoparticle (CdS), creating a single helix through selective attachment on one face of the ribbon.[44,45] After several months of CdS deposition on the organic ribbons, double helix structures were obtained using the same precursors. Chiral helices were also created using zinc sulfide or silica nanoparticles with co-assembly of cholate and Ca^{2+} ions.[46] Furthermore, chiral polymers have also been investigated as templates to host silica nanoparticles resulting in an overall chiral structure.[39]
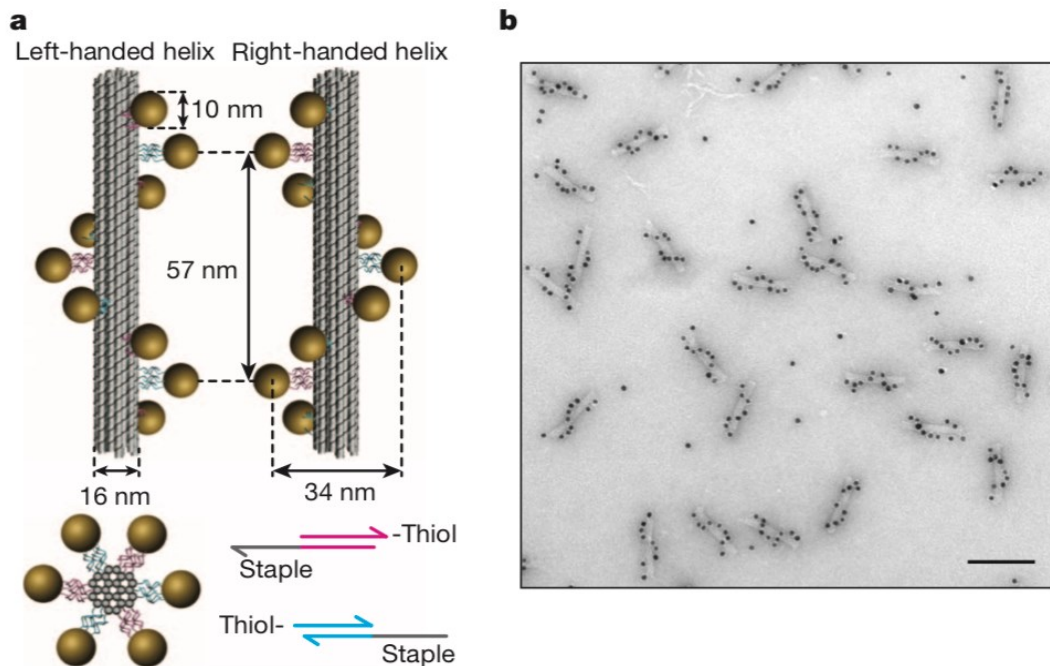
Figure 8. Chiral nanoparticles through DNA scaffolding. Left-handed or right-handed helices made up of modified DNA were used as a template for gold nanoparticles to bind (a). The binding of the nanoparticles to the DNA creates a twist inducing helical chirality in the structure (b). (Kuzyk, et al. Nature, 2012, 483, 311–314.)

1.3.2 Chirality Through Surface Modifications

The aforementioned approaches are not the only way to obtain chiral nanoparticles. In fact, chirality can be endowed through surface modification with chiral ligands (Figure 9). Several studies have been conducted where chiral molecules such as cysteine and its derivatives,[47,48] penicillinamine ,[49] malic acid,[50] tartaric acid,[50] among others, were used as capping agents on achiral quantum dots. In Figure 9, the surface of CdS nanoparticles are modified using chiral L-/D-penicliiamine molecules to render them chiral nanoparticles.   By using one or the other enantiomer to modify the surface, the nanoparticles were rendered chiral evidenced by circular dichroism which showed mirror like images for the opposite enantiomers. These chiral nanoparticles have been used in chiral sensing

application to selectively identify chiral analytes using simple techniques such as fluorescence spectroscopy.
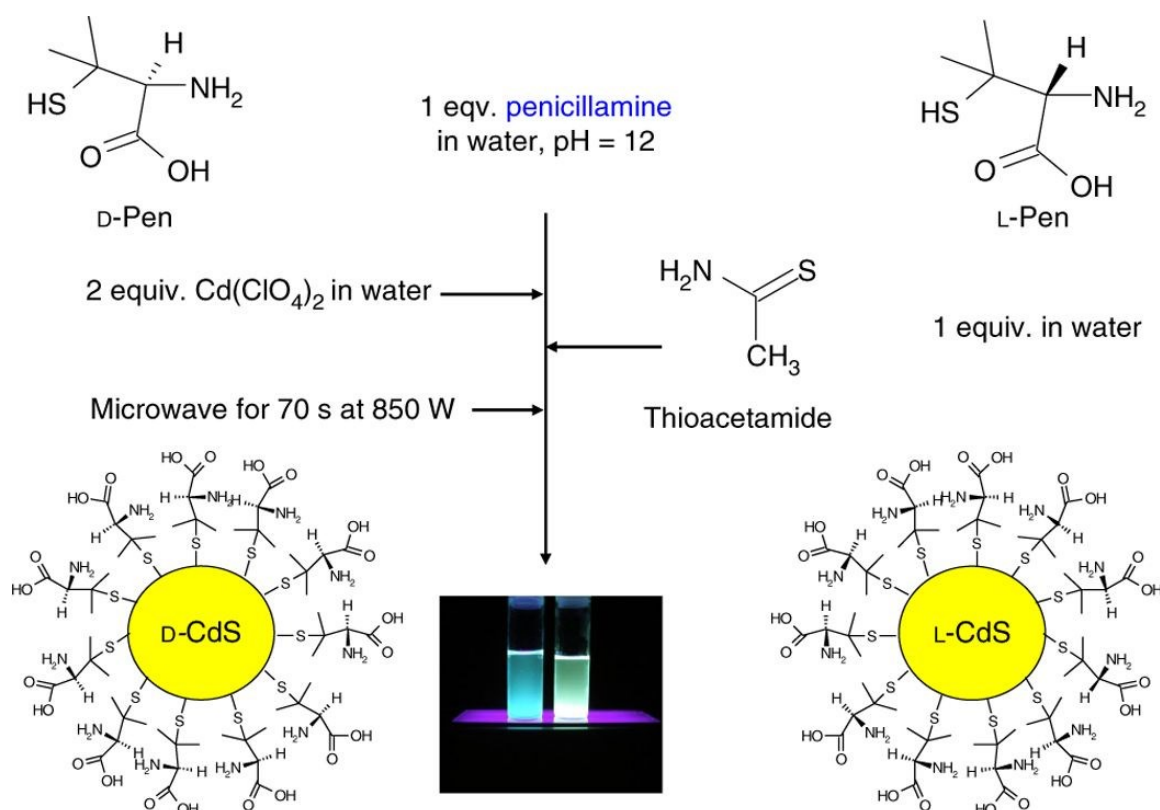
Figure 9. Chirality in quantum dots achieved through surface modification. In this example, a CdS nanoparticle was rendered chiral by modifying its surface with chiral peniclliamine molecules. D-penicllinamine functionalized CdS gave D-CdS nanoparticles and L-penicillamine gave rise to L-CdS nanoparticles. (Moloney et al., Nat. Protoc., 2015, 10, 558–573.)

In metallic nanoparticles, surface modification using similar chiral molecules have also been used.[41,51] Interestingly, enhancement of chiral properties was noted in some of these systems and was attributed to the coupling of the nanoparticle and the molecule.[41] The enhancement was a result of changes in the electromagnetic field caused by the metallic nanoparticle's surface plasmon resonance. For example, the surface of silver nanoparticles was modified using chiral, L-glutathione-bimane and the effective coupling of these materials was evidenced

through the optical properties of L-glutathione-bimane molecules at 390 nm and Ag nanoparticles at 400 nm , which showed an enhanced chiral signal.[51]

In carbon nanoparticles, chirality has also been observed in carbon nanotubes through the rolling axis of the hexagonal graphene sheet.[52] Chirality in this nanoparticle system has garnered interest because depending on its chiral indices, they can be classified as metallic or semi-conductor type nanoparticles.[52] Furthermore, chirality has been also explored in graphene dots through modification of its surface by chiral ligands.[53–56] Recently, chirality has also been observed in carbon dots (CDs), such as those discussed in this thesis, through both surface modification of the nanoparticle through chiral capping agents or through in-situ synthesis of nanoparticles with chiral precursors.[57–64] While these preliminary reports are encouraging and suggest the possibility of preparing chiral CDs, many questions remain unanswered and require further explorations. Prior to elaborating on the current challenges, a brief account of CDs and their properties is provided below.

1.4 The Nano-sized History of Carbon Dots

1.4.1 Discovery of the Carbon Dots

In 2004, a new type of carbon nanomaterials were accidentally discovered by Xu and co-workers during the purification process of carbon nanotubes[65] (Figure 2.10 a) and in 2006, Sun and co-workers coined the term CDs to describe these fluorescent nanoparticles (Figure 10 b).[66] Since then, an exponential growth has been witnessed in the body of work dedicated to CDs.[67] Their popularity has been largely due to their abundant, non-toxic, inexpensive and facile synthesis, and as well as due to their versatile physico-optical and chemical properties.
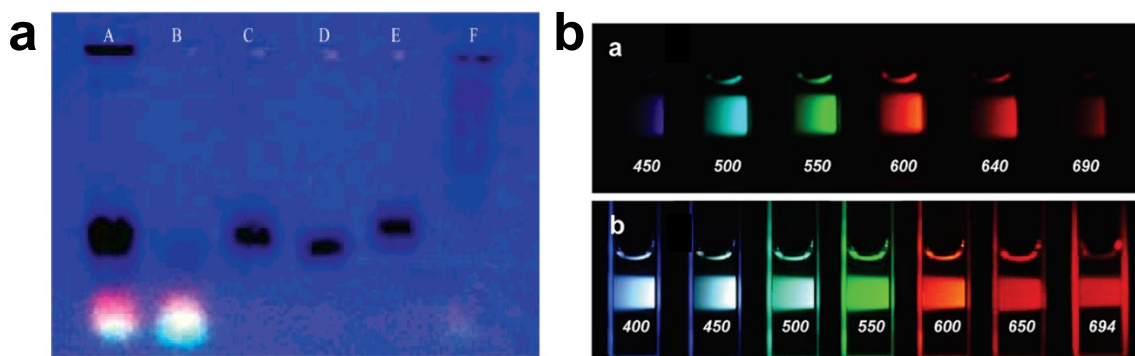
Figure 10. Serendipitous Discovery. In 2004, Xu and coworkers discovered CDs during the purification of carbon nanotubes (a). Later, Sun and co-workers synthesized multi-colored CDs through surface modification with PEG (b). (Xu et al., J. Am. Chem. Soc., 2004, 126, 12736–12737.; Sun et al., J. Am. Chem. Soc., 2006, 128, 7756–7757.)

CDs are quasi spherical, amorphous nanoparticles that are predominantly less than 10 nm in size.[67–70] They can be synthesized from any carbon containing precursors including common household items like coffee,[71,72] table sugar[72–74], orange juice,[75–77] etc., all of which have been reported in the literature and as well as more defined precursors such as amino acids,[78,79] carbohydrates,[80,81] amines,[68,82] to name a few. The exact composition of CDs typically varies depending on the precursors used; however, they are primarily comprised of an sp^2/sp^3 hybridized carbon network in the core of the nanoparticle with functional groups containing nitrogen, sulphur, oxygen and hydrogen decorating the surface.

The possibility of synthesizing CDs from a wide array of precursors gives rise to a nanoparticle system with a large repertoire of interesting and tunable properties.

1.4.2 Physical Properties of Carbon Dots

Typically, elemental or bulk carbon is black in color with low solubility and possesses no interesting optical properties. However, CDs have excellent dispersibility in water due to many polar functional groups decorating the surface.[68,83–86] They can also be prepared with hydrophobic or amphiphilic characteristics by modifying the surface groups on the nanoparticle, or via appropriate selection of the precursors. These dots exhibit low chemical toxicity owing to the absence of heavy metals. Moreover, based on recent literature, CDs have also been shown to have high biocompatibility and low cytotoxicity and as such they may be suitable for myriad of biological applications such as biosensing,[87–89] bio-imaging[90–94] and drug delivery[95–97].

1.4.3 Optical Properties of Carbon Dots

Unlike bulk carbon, CDs also have fascinating optical properties one of which is their tunable fluorescence that can range from the ultra-violet to near-infrared regions of the spectrum.[83,85,89] Other fascinating aspects of their optical properties include low photobleaching and photoblinking in comparison to other fluorescent molecules and nanomaterials including quantum dots for example. Photobleaching is the irreversible modification of covalent bonds in a conjugated system where such an effect results in a loss of the fluorescence properties. CDs have been shown to have resistance to photobleaching on the order of several hours following exposure to intense UV excitation. Moreover, the dots do not undergo photoblinking meaning that they do not equally relax through both radiative and non-radiative pathways. As such, an "on-off" fluorescence is not typically observed. The low propensity for photoblinking stems once again from passivation that decreases non-radiative relaxation pathways. The origins of the fluorescence in CDs is not quite well understood and the fluorescence mechanism(s) of CDs has/have yet to elucidated. However, their optical properties have often been

ascribed to three well-known mechanisms namely quantum confinement, surface states and core states.

1.4.4 The Quantum Confinement Effect

The quantum confinement effect is the classical explanation for fluorescence in most nanoparticle systems.[67,70,87,98] When the size of the nanoparticle is smaller than the Bohr radius, its optical and electronic properties are tuned through changes in the bandgap separating the valence and conduction bands. Following the quantum mechanical explanation of the particle-in-a-box, the bandgap energy is directly related to the size. Therefore, CDs of smaller size have a larger band gap and fluoresce at shorter wavelengths and conversely a red shift in fluorescence is observed as CD size increases. While this mechanism is plausible, it has not been observed for all CD systems and thus is not the only underlying mechanism for fluorescence. Indeed, there exists a body of research showing fluorescence in CDs that is independent of the particle size.[99,100]

1.4.5 The Surface State of Carbon Dots

The failure of the quantum confinement effect to describe fluorescence in many CD systems promoted alternate explanations that have crystallized in a theory regarding surface states and passivation (Figure 11).[67,70,87,98,101] A multitude of surface states can often be found in CDs and can be evidenced through excitation dependent fluorescence (Figure 11 a). This occurs as various surface states of the CDs are excited at the different wavelengths with a change in the fluorescence is observed. Alternatively, excitation independent fluorescence can be induced via surface passivation. This process involves decoration with functional groups that can increase and enhance radiative pathways,[102,103] via reduction of surface defects. It promotes an optically uniform CD surface and as such, the system exhibits excitation independent fluorescence (Figure 11 b). Passivation usually requires the introduction of electron donating atoms/molecules on the surface of the dot. A fortunate consequence of passivation is the decrease in the

number of surface defects and traps, which in turn translates to a higher fluorescence quantum yield.
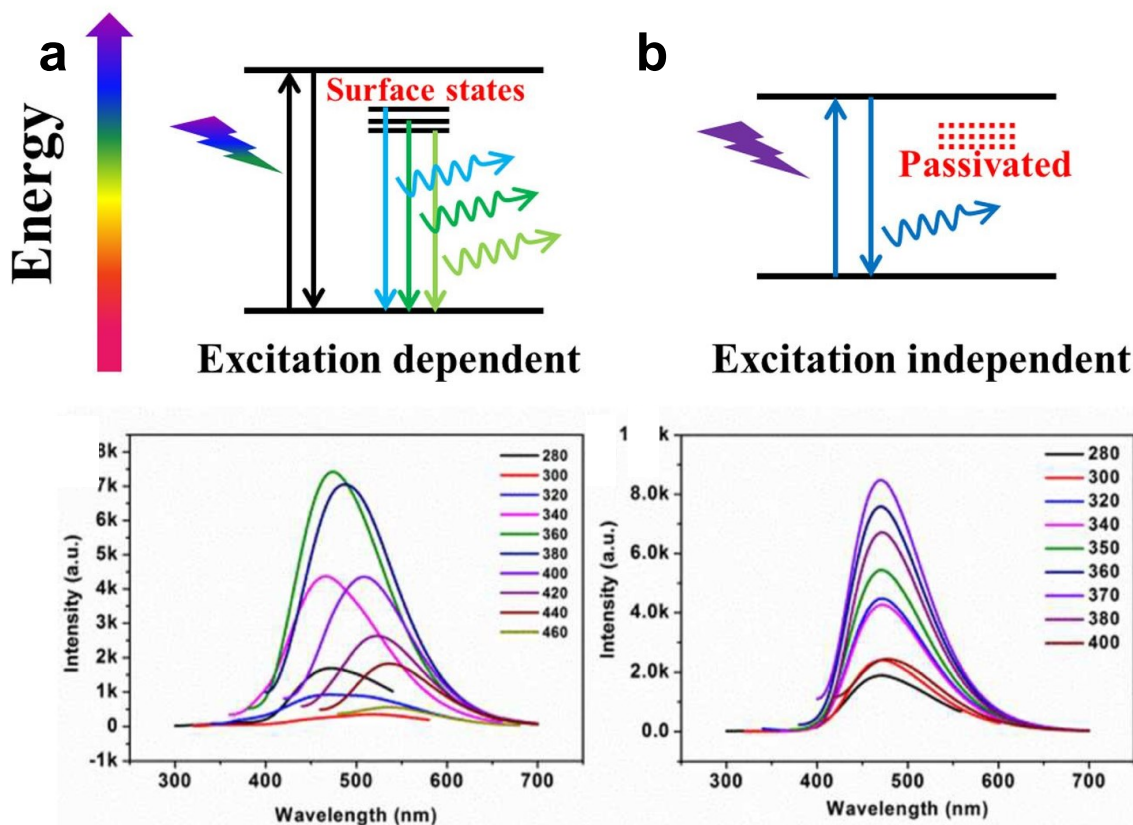
Figure 11. The surface state fluorescence of CDs. Multiple different surface groups can contribute to the observed fluorescence properties (a). Therefore, it is excitation dependent emission. As the excitation wavelength is changed, the CDs display a shift in the fluorescence wavelengths (a). When the CDs are passivated, the surface becomes uniform and as such, one prominent functional group is obtained. Therefore, a single fluorescence band is observed from the nanoparticle surface and remains unshifted (b). (Li et al., *Sci. Rep.*, 2015, 4, 4976.; Wen et al., *RSC Adv.*, 2016, 6, 27829–27835.)

1.4.6 The Core State of Carbon Dots

Similar to the surface emissive states, several works in the literature have also suggested that fluorescence could arise from the core of the CD.[98,104,105] Through

radiative recombination of excitons in the hybridized carbon core, the CDs can exhibit a weak blue fluorescence with low quantum yields. Red shifting of the fluorescence from the core of the CDs can also be observed even when heteroatom doping occurs in the hybridized carbon core system (e.g. formation of a pyridine, thiophene ring). More recently, the fluorescence mechanism exploiting both the core and surface states of the CDs has garnered popularity (Figure 12). This theory speculates that an exciton is generated when the core is excited; the exciton is then transferred to the surface of the dot and a radiative recombination enables the observed fluorescence of the nanoparticle.
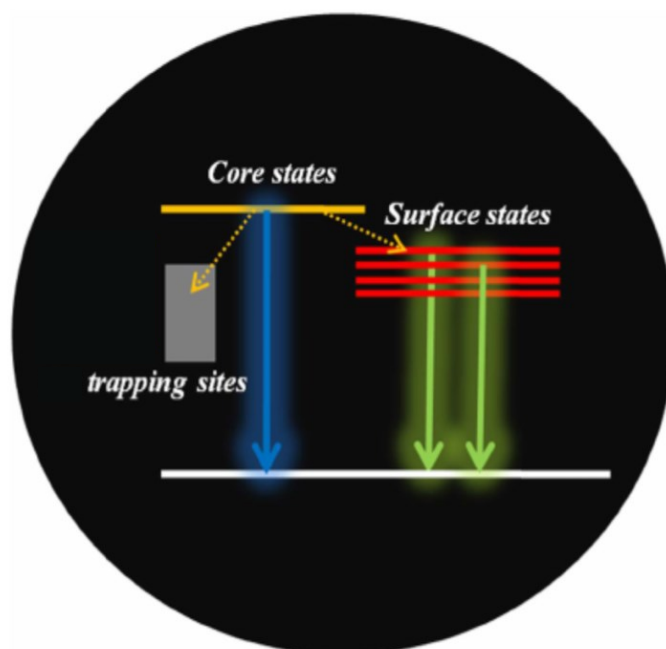
Figure 12. The core state fluorescence of the CDs. A synergy between the core and surface states are known to have an impact on the fluorescence of the CDs. An exciton is generated in the CD core; this exciton can then be transferred to the surface states of the CD. The exciton then undergoes a radiative recombination to produce the observed fluorescence in the dots. (Jiang. Et al., Sci. Rep., 2016, 6, 19991.)

1.4.7 The Synthesis of Carbon Dots

The synthesis of CDs can be achieved through 2 principle approaches classified as top-down or as bottom-up methods (Figure 13).[83,87] In a top-down synthesis, CDs can be prepared by breaking down large carbon materials, such carbon
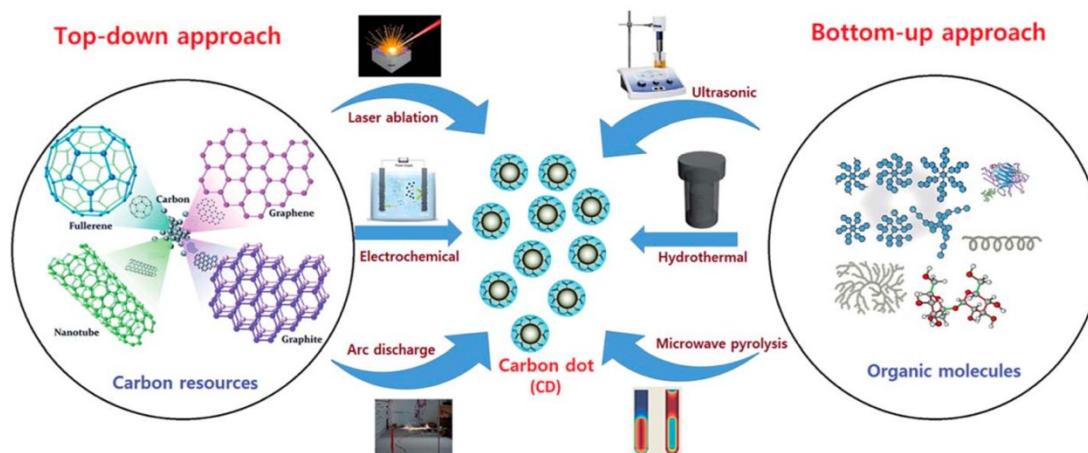
Figure 13. The different approaches to CD synthesis. Top-down synthesis is the breakdown of larger carbon materials, while bottom-up synthesis relies on the combination of small carbon precursors to form CDs. (Sciortinoet al., Carbon N. Y., 2018, 4, 67.)

nanotubes, graphite and graphene oxide, using methods such as arc discharge,[65] laser ablation[106–108] and electrochemical oxidation.[109,110] CDs derived from the top-down synthetic approaches often have structural features that resemble the starting precursors and as such they have simple and well-defined structures. However, these CDs often suffer from large size distributions and low quantum yields (1.1-1.5%) that require surface passivation post synthesis.

In bottom-up synthesis, CDs are prepared from molecular precursors via thermal-mediated reactions (160 - 240°C) such as hydrothermal,[64,77,111] microwave[68,82,86,112,113] and ultrasonic reactions[114,115]. These methods produce CDs via a series of condensation, cyclization, polymerization and carbonization reactions of the precursors. Typically, the resulting CDs are highly fluorescent and do not require post-synthesis modification because the precursors often contain various heteroatoms and functional groups that act as both precursors and surface passivating agents. While the synthesized CDs have high fluorescence quantum yields, the reaction yields are often low (<30 %) and require extensive purification to remove starting materials, fluorophores or other species.

1.4.8 Microwave Assisted Synthesis of Carbon Dots

The work in this thesis was carried out using CDs prepared via microwave chemistry. As such, a brief discussion of the technique is provided. Microwave assisted synthesis of CDs is one of the prevalent methods of bottom-up nanoparticle synthesis owing to the numerous advantages relative to hydrothermal or thermal oxidation assisted syntheses.[68,86] A typical microwave reaction occurs when radiation is absorbed by polar molecules in the reaction mixture. The absorption of radiation produces heat to drive the reaction and contributes towards the formation of the products. The heat is generated in the system as result of dielectric heating where the electric dipole of the polar molecules aligns to the electric field by molecular rotation. When the electric field alternates, the molecules rotate losing polarization and creating friction, which produces heat for the reaction.

In a synthetic microwave, the reaction vials are microwave-transparent and therefore the radiation is absorbed directly by the precursors and converted to heat (Figure 14 a). In contrast, conventional heating requires heat transfer from the heating apparatus to the reaction vessel and then to the molecular precursors. During the course of the reaction, a heat gradient is generated from the outside to the inside of the reaction vessel (Figure 14 b) leading to often incomplete reactions and the formation of many side products. In order to overcome these limitations, reaction temperatures and times are often increased which could degrade the starting materials and minimize product yields. Consequently, microwave-assisted reactions are typically more efficient as heat is distributed in a uniform manner, at shorter reaction times and lower reaction temperatures.

Despite their high efficiency and uniform heating, commercial scale-synthesis of microwaves is not possible as most microwave reactors have small reaction volumes. Moreover, these reactions are often limited by starting materials that are able to absorb microwave radiation or have high boiling points since most microwave reactors have a pressure cut-off around ~300 psi. With a plethora of carbon-based precursors and a wide range of solvents, the limitations of the

microwave assisted synthesis could be easily overcome to produce highly fluorescent CDs.
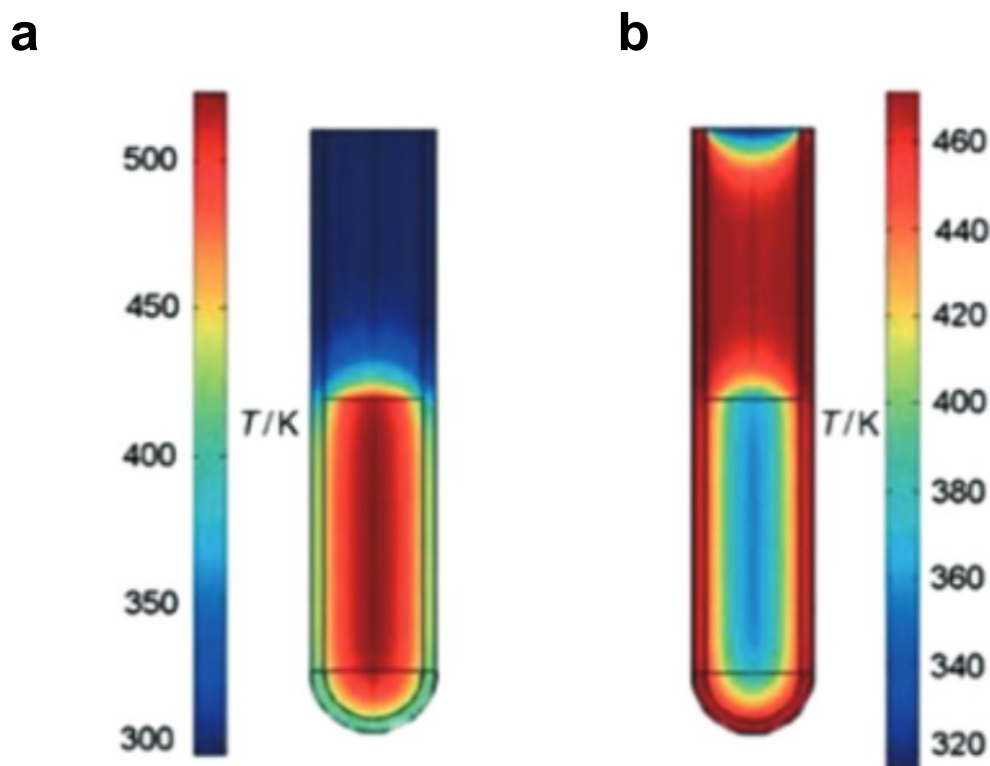
Figure 14. The efficiency of heating by microwave radiation. When the reaction vessel is irradiated by microwave radiation, the sample (in the middle) gets uniformly heated at the right temperature (a). The same sample displays a gradient of temperature when heated using a conventional heating technique (b). (De Medeiros, et al, J. Mater. Chem. C, 2019, 7, 7175–7195.)

1.4.9 Carbon Dot Formation Mechanism

Recent advances in the CD field have attempted to gain an understanding of the mechanism of formation of these nanoparticles (Figure 15).[116–119] In the bottom-up approach, and as the reaction begins, precursors undergo dehydration and condensation reactions. These reactions give rise to molecular species that in some cases could be fluorophores. These molecular species react with each other via polymerization and cyclization reactions. The structures formed from these

reactions can then undergo crosslinking and carbonization reactions to generate CDs. But these reactions don't occur in a linear manner as described. The reality in the CD formation is that these reactions all occur simultaneously such that products from each stage can interact with each other resulting in a large array of structures during synthesis.
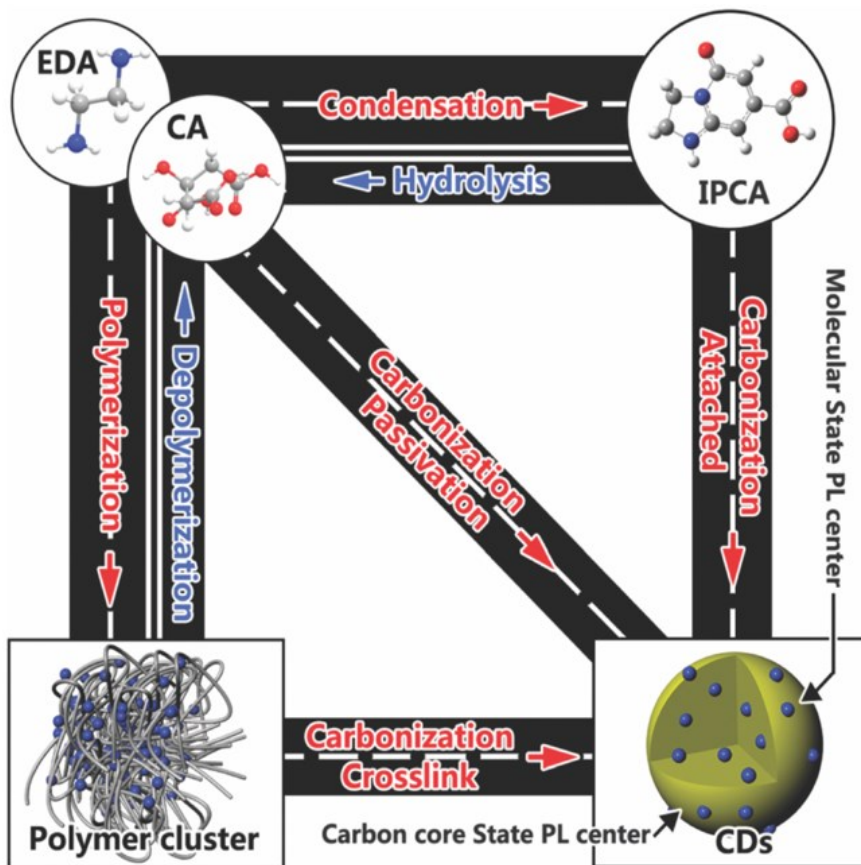
Figure 15. Postulated CD formation mechanism. The CD formation occurs through a series of simultaneous reactions. (Song et al, J. Mater. Chem. C, 2015, 3, 5976–5984.)

1.5 Statement of the Problem

Understanding the importance of chirality in the biological systems and the pharmaceutical industry, our interest laid in synthesizing chiral carbon nanoparticles. Our nanoparticles of interest are CDs, a relatively new member of the carbon allotrope family. The overarching goal of the project was to prepare chiral CDs in a thermal-based approach using chiral precursors. While indeed, few studies have been conducted on chiral carbon dot synthesis, these works often reported long synthesis protocols, lacked sufficient purification protocols and often raised questions as to the origins of chirality in these systems. Furthermore, there remains a general lack of knowledge as to how these chiral nanoparticles are actually formed.

Specifically, the work in this thesis focuses on the synthesis of CDs using a cysteine chiral precursor in a facile one-step microwave reaction. We tuned the synthesis conditions including temperature, time and precursor concentration in order to glean an understanding of how this can impact chirality and how it can be exploited to tailor the optical, physical and chiral properties of the resultant dots. Working in an iterative approach, a spectrum of chiral and optical properties can be dialed in by varying the reaction parameters. Moreover, through chromatographic approaches, we attempted to understand the formation of the CDs in hopes of elucidating their origins of chirality.

Finally, in a proof of concept application that exploits chirality in nature, chiral CDs were examined as potential anti-microbial agents. The CDs were tested against various gram-positive and gram-negative bacterial strains including *Bacillus subtilis* DSM10, *Burkholderia thailandensis* E264, and *Micrococcus luteus* DSM20030, as well as *E. coli* ATCC25922, MG1655 and *Klebsiella aerogenes* ATCC13048. The minimum inhibitory concentrations of the CDs were determined using both broth microdilution and direct colony suspension testing according to Clinical and Laboratory Standards Institute (CLSI) guidelines.

Chapter 2: Experimental Procedure for Synthesis and Optimization Introduction

2.1 Procedure for Synthesis of chiral Carbon Dots

2.1.1 Microwave Synthesis of Carbon Dots

The CDs were synthesized using a synthetic CEM Discover SP microwave. The 1:1 chiral cysteine CDs (cysCDs) were prepared by a one-pot synthesis of 4.0 mL solution containing 0.5 M of cysteine and 0.5 M citric acid in water. This solution was sonicated until a clear dispersion was obtained and placed inside a 35 mL microwave vial. The microwave vial was subjected to microwave irradiation with the various reaction parameters programed into the CEM Discover SP microwave software. Different temperatures and reaction times were tested to optimize the residual chirality observed in the cysCDs. The reactions were examined at temperatures: 160 °C, 180 °C, 200 °C and 220 °C and times: 5, 10 and 15 minutes. All reactions were pre-stirred in the microwave for two minutes and during the course of the reaction.

After optimization of chiral cysCDs, the non-chiral cysCDs were obtained in a similar manner using 4.0 mL of 0.5 M citric acid solution as a control and the solution was subjected to 160 °C at 10 minutes. The 1:2 chiral cysCDs were prepared by decreasing the concentration of cysteine in respect to the citric acid; a solution of 4.0 mL solution containing 0.25 M cysteine and 0.5 M citric acid was microwaved at 160 °C at 10 minutes. Similarly, the 2:1 chiral cysCDs were synthesized using 0.5 M cysteine and 0.25 M citric acid at the same reaction parameters. The L-cysCDs and D-cysCDs were obtained using L-cysteine and D-cysteine respectively.

2.1.2 Purification of Carbon Dots

In order to isolate cysCDs from the reaction mixture, the synthesized cysCDs were purified by dialysis and organic washes prior to characterization (Figure 16). After cooling down the samples to room temperature, they were dialyzed using a cellulose dialysis membrane (cut-off 1000 Da) to remove any unreacted starting materials and organic fluorophores. The dialyzed sample is also subjected to several organic washes with acetone followed by centrifugation. The precipitate was collected after each wash and subjected to acetone washes until the supernatant is non-fluorescent. The precipitate was dried in the oven at 80 °C overnight before further analysis.
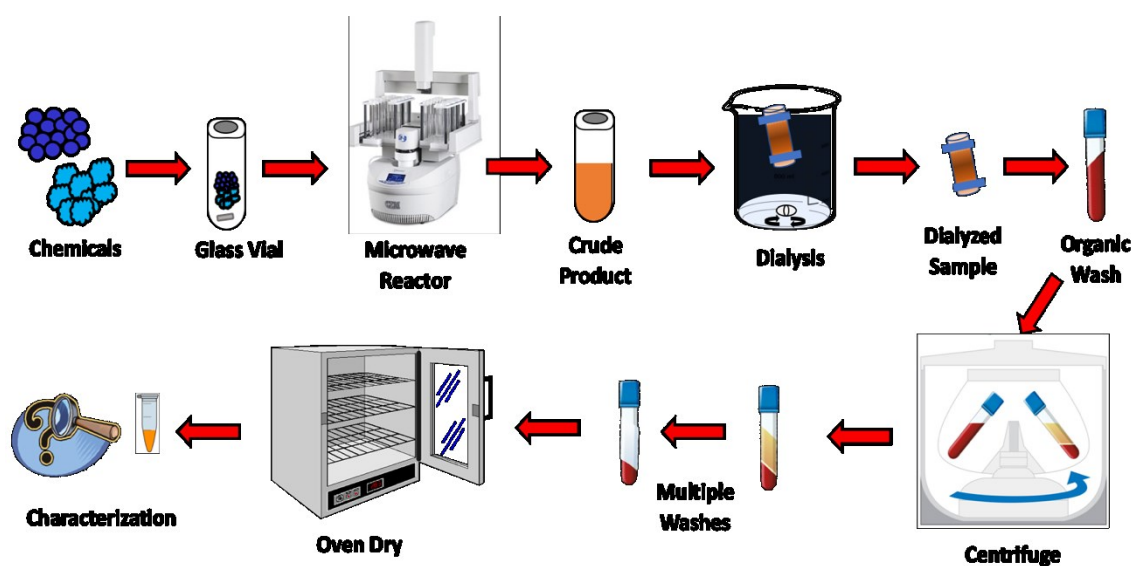
Figure 16. The synthesis and purification process of chiral cysCDs. The chiral CDs were synthesized using a microwave synthesis reaction and purified through several dialysis and organic wash steps.

2.2   Characterization Techniques

2.2.1 Transmission Electron Microscopy (TEM)

For Transmission Electron Microscopy (TEM), CDs were dispersed in water at a concentration of 100 mgmL-1solution and applied to the formvar-coated 200 mesh copper TEM grids (Electron Microscopy Sciences).

2.2.2 X-Ray Diffraction (XRD)

XRD analysis of the CD samples were collected using a 2nd Gen D2 Phaser X-ray diffractometer (Bruker AXS). A Cu Ka source at a generator power of 30 kV and 10 mA, coupled 2y/y scans in the continuous PSD fast scan mode was used to for data acquisition. The scan range was set from 10 to 90.

2.2.3 Elemental Analysis

Elemental analysis was obtained of the dried CD samples using vario MICRO cube elementar. Sample sizes of 3 mg was combusted in the presence of oxygen to aquire data.

2.2.4 Fourier   Transform   Infrared   Spectroscopy–Attenuated   Total Reflectance (FTIR-ATR)

Fourier-Transform Infrared Spectroscopy (FT-IR) spectra were collected using a Thermo Scientific Nicolet iS5 equipped with an iD5 ATR accessory. Spectra were collected using 64 scans with a resolution of 0.4 cm−1, a gain of 1, an optical velocity 0.4747 and an aperture setting of 100. Data was processed using the Thermo Scientific Nicolet Omnic 9 software.

2.2.5 X-Ray Photoelectron Spectroscopy (XPS)

X-ray Photoelectron Spectroscopy (XPS) spectra of the CDs were acquired using a Thermo Scientific K-Alpha X-ray Photoelectron Spectrometer. A total of 10 scans

were collected per analysis and repeated in triplicate. The analysis was done using the Thermo Scientific™ Avantage Data System software.

2.2.6 Thermogravimetric Analysis (TGA)

TGA analysis was conducted on powdered CDs using TGA-Q500 from TA Instruments in platinum pans, under an argon environment. The samples were heated at a rate of 10 °C min^{-1} from 30°C to 1000°C and the data was analyzed using the Thermal Advantage 5.0 software.

2.2.7 Absorbance Spectroscopy

UV-visible absorption spectra were obtained in the spectral range of 200–800 nm using a Cary 5 Series UV-Vis-NIR Spectrophotometer (Agilent Technologies). A 1 cm quartz cuvette was used with a 2.5 nm bandwidth and wavelength changeover at 400 nm. All data collection and processing was carried out with an Agilent Cary Eclipse Scan software package.

2.2.8 Fluorescence Spectroscopy

Fluorescence spectra were recorded using a Cary Eclipse Fluorescence Spectrophotometer (Agilent Technologies). The concentration of the CDs dispersed in water were adjusted to an absorbance value of 0.1 a.u. to minimize inner filter effects. Spectra were acquired in a 1 cm quartz cuvette at λex = 250-550nm (100 nm intervals). The excitation and emission slits were set to a width of 2.5 nm with a PMT voltage at 600V. All data were processed using the Agilent Cary Eclipse application software.

2.2.9 Circular Dichorism Spectroscopy

Circular Dichroism spectra were obtained using a JASCO J-815 spectropolarimeter (JASCO) and a 10 mm quartz cuvette. The data was collected from 180 nm to 500 nm in 3 accumulations. The scans were continuous with a scanning speed of 50 nm/min. The data was processed using Spectra Manager II software.

2.2.10 Bacterial Cultivation

Escherichia coli ATCC25922 and *Klebsiella aerogenes* ATCC13048 were acquired from the American Type Culture Collection (ATCC). *E. coli* MG1655 and *B. thailandensis* E264 were gifts of Eric Déziel, INRS. *M. luteus* DSM20030 and *B. subtilis* DSM10 were obtained from the Leibniz Institute DSMZ-German Collection of Microorganisms and Cell Cultures. Bacteria were grown in Luria-Bertani (LB) media, at either 37 °C (*E. coli*) or 30°C (*M. luteus*, *B. subtilis*, *B. thailandensis*, *K. aerogenes*), rotating at 225 rpm. Bacterial isolates were streaked on 1.5% agar LB plates and placed at 37°C or 30°C for 18-24 h prior to MIC testing.

2.2.11 Minimal Inhibitory Concentration (MIC) Determinations

Following CLSI guidelines for broth microdilution and direct colony suspension testing,[120,121] bacterial cultures were transferred to Mueller Hinton Broth (MHB) (*E. coli*) or LB (*M. luteus, B. subtilis*, *B. thailandensis*, *K. aerogenes*) and adjusted to a final turbidity equivalent to a 0.5 McFarland standard (1.5 X 10^8 **CFU**/ml). Bacteria were diluted to 1.5 X 10^6 **CFU**/ml then mixed 1:1 with the compound of interest in 96-well plates.

Chapter 3: Results and Discussion

3.1 Tailoring Chirality in Carbon Dots

3.1.1 Thermal Decomposition Synthesis of Carbon Dots

The chiral cysCDs were synthesized using a microwave reactor according to the principles of the thermal decomposition reaction. The thermal energy facilitates the breaking of covalent bonds in the starting materials. These fragmented pieces of precursors recombine forming new covalent bonds and resulting in the formation of the nanoparticles. Therefore, by controlling the rate of precursor decomposition, the nanoparticles could essentially be tuned to obtain the desired physico-optical properties. In order to investigate the chiral properties of the cysCDs, we aimed to control the decomposition rate by varying reaction parameters: precursors, reaction temperature, reaction time and relative ratios of the precursors.

3.1.2 Inducing Chirality in Carbon Dots- Precursors

One of the main objectives was to synthesize CDs in a one-step reaction from chiral precursors without the need for post-synthesis modifications. Hence, the chirality in the nanoparticles was induced by using chiral starting materials such as sugars, or amino acids. The enantiomers of amino acids, in particular L- and D-cysteine, were chosen after preliminary testing with chiral sugars and branched amino acids that produced achiral CDs.

In addition to the chiral cysteine precursor, an achiral molecule, citric acid, was combined with the reaction mixture due to its larger carbon backbone. A larger backbone of carbon could facilitate the formation of cysCDs through cyclization and carbonization reactions. The reaction was completed in an aqueous environment due to its ability to efficiently absorb microwave radiation. Furthermore, water, the reaction solvent contains no carbon atoms and is thus passive offering no influence on the chiral properties of the nanoparticle. Below, a synopsis of the synthesis optimization efforts is provided followed by detailed characterization data.

3.1.3 The Effect of Reaction Temperature

The decomposition temperature of the precursors, citric acid and cysteine, are 175 °C[122] and 240 °C [123] respectively. As such, reaction temperatures of 160 °C, 180 °C, 200 °C and 220 °C were investigated to optimize the residual chirality in the nanoparticles. The reaction temperature had a significant impact on the residual chirality observed in the nanoparticles as it determined the degree of decomposition of the precursors.

An increased reaction temperature resulted in an increased energy leading to greater motion and collision of molecules. Consequently, a greater degree of decomposition in the precursors and its reformation into products was observed. However, a decrease in the chirality of the nanoparticle was observed at high reaction temperatures. On the other hand, low reaction temperatures did not have sufficient energy to break covalent bonds in the precursors and form the nanoparticles. Therefore, the reaction temperature was indeed crucial in tailoring chirality on the cysCDs.

3.1.4 The Effect of Reaction Time

Following optimization of reaction temperature, the role of reaction time was also examined. As the synthesis was carried out using a microwave reactor, reaction times of 5, 10 and 15 minutes were experimented to observe the residual chirality.

Similar to the reaction temperature, an increased reaction time increased the likelihood of precursor decomposition as more time was given for the reaction to be completed. The prolonged time allowed for increased motion and collision of precursors resulting in chiral precursors fragmentation. However, if the synthesis time was too short, the reaction does not proceed to completion and nanoparticles cannot be formed as desired with efficient physical and optical properties. Hence, an equilibrium in reaction time was needed to retain the chirality in the cysCDs.

3.1.5 The Effect of Reagent Ratio

The chiral property of the cysCDs was primarily determined from the chiral precursors, L- and D- cysteine. The ratio of cysteine was varied with respect to citric acid to investigate its effects on the overall chirality of the nanoparticle. An increase in cysteine concentration resulted in an increased chirality as more chiral precursors were available to be incorporated into the cysCDs. Likewise, a decrease in cysteine concentration resulted in decreased chirality as fewer chiral precursors were available.

3.2 Physical Characterizations of Chiral Carbon Dots at Various Reaction Parameters

3.2.1 Morphological Characterization of Chiral Carbon Dots

Following the synthesis of cysCDs, TEM was carried out in order to confirm its formation and assess its size and morphological properties. The principles of TEM are similar to that of light microscopy, but this technique uses electrons instead of light to obtain higher resolution images. This image is produced as a result of a high energy beam of electrons transmitted through a thin sample.

The TEM images of the cysCDs evidenced small quasi-spherically shaped nanoparticles with some instances of agglomeration. Figure 17 shows the TEM image for the cysCDs prepared at 160°C and 10 mins. The observed agglomeration of the cysCDs is attributed to solvent evaporation following deposition on the TEM grid. Additionally, the cysCD samples exhibited poor contrast due to the low electron diffraction as they are primarily amorphous in nature.

TEM analysis of the cysCDs, prepared under different reaction parameters of temperature, time and precursor concentration, did not show significantly different sizes, which typically ranged from 13 - 15 nm. The average size distribution of all the cysCD systems prepared was determined to be 15 nm ± 4.0 nm, which is in

accordance with the sizes of similar systems previously reported in the literature.[124,125] The size dispersity was ~25% suggesting that the cysCDs are polydisperse. This large dispersity can be attributed to the agglomeration, which can induce error in the size measurements. The TEM size statistics obtained for all cysCDs, prepared at different reaction parameters, are summarized in Table 1 and the individual TEM images can be found in Appendix Figure A1- A4.
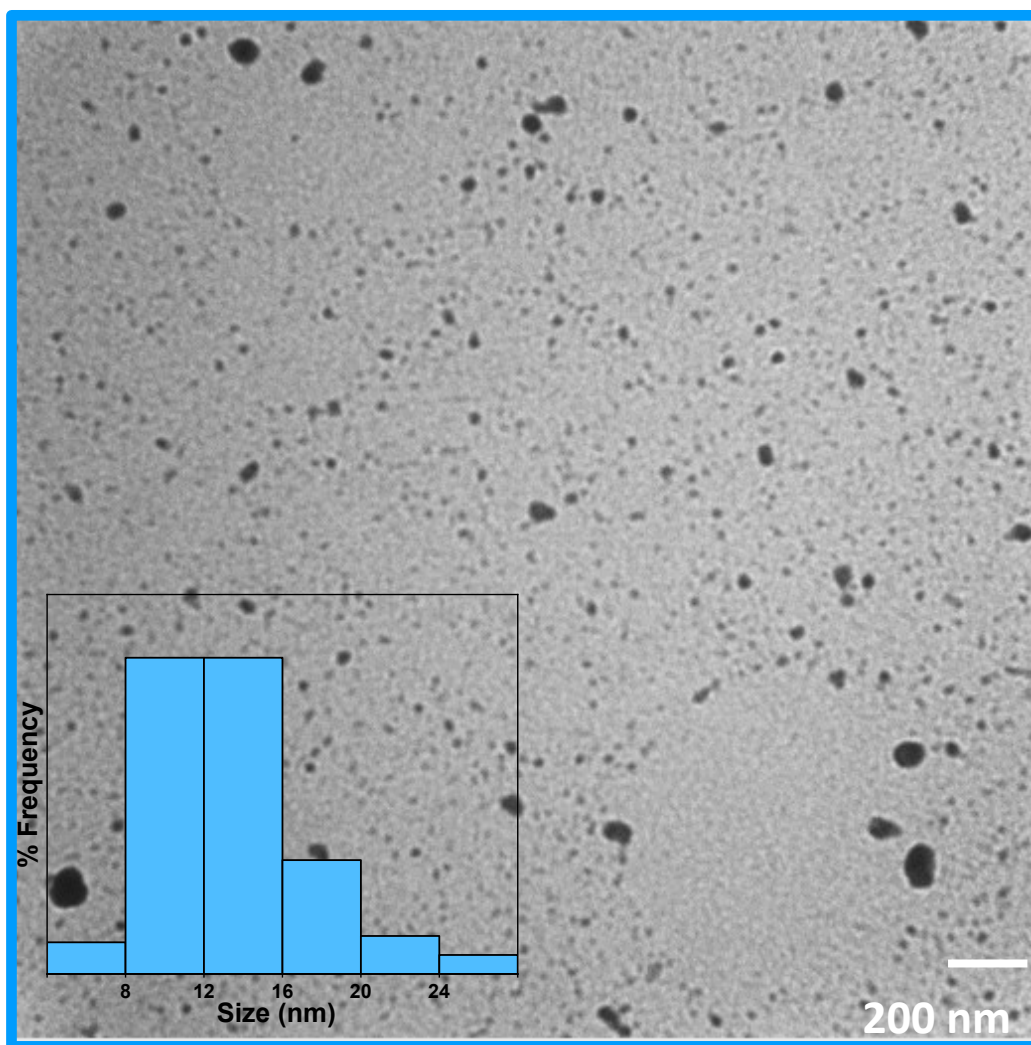
Figure 17. TEM Image of cysCDs prepared at 160°C and 10 mins. The cysCDs are quasi-spherical in shape with an average size of 15.0 ± 4.0 nm. The low contrast of the image is caused by the poor electron diffraction of cysCDs as they are amorphous in nature.

The average particle size seems to slightly increase with an increasing reaction temperature from 160 °C to 200 °C with the exception of the nanoparticles at 220 °C, which were smaller than the cysCDs prepared at 200 °C. Typically, nanoparticle growth is governed by processes such as Ostwald ripening and oriented attachment that promote the growth of larger particle at the expense of smaller particles. At higher temperatures, the Brownian motion and the dissolution of small particles are increased. Therefore, they are readily dissolved in solution and collide more frequently favoring the growth of larger particles. These larger particles are further stabilized by the Gibbs–Thomson effect, which states that smaller particles are readily dissolved than larger particles. Hence, the trend of increasing particle size could be caused by the nanoparticle growth mechanism.

In comparison, the mean particle size seems to decrease with increasing reaction time from 5 mins to 15 mins. While the trends observed in Table 1 are supported by the theories of nucleation and growth, it is difficult to conclusively interpret due to the large polydispersity values measured. Interestingly, no significant change in particle size was observed following variation of the precursor ratio. The chiral nature of the precursor does not impact the particle size or the size statistics. In fact, the cysCDs from either enantiomer of cysteine show similar mean particle sizes and distributions determined to be 13.3 ± 4.1 nm and 14.0 ± 4.5 nm for the L- and D-cysteine, respectively.

Table 1. Summary of cysCD sizes measured following synthesis at different reaction parameters.

		Size (nm)
Temperature (All reactions were done at 5 mins)	**160 °C**	15.1 ± 3.7
	180 °C	18.5 ± 5.6
	200 °C	21.1 ± 5.1
	220 °C	17.1 ± 3.7
Time (All reactions were done at 160 °C)	**5 mins**	15.1 ± 3.7
	10 mins	13.3 ± 4.1
	15 mins	12.2 ± 3.3
Ratio (All reactions were done at 160 °C- 5 mins)	**1 L-CYS : 1 CA**	13.3 ± 4.1
	1 L- CYS : 2 CA	15.1 ± 3.7
	2 L-CYS : 1 CA	14.8 ± 2.7
	1 D-CYS : 1 CA	14.0 ± 4.5
	1 D-CYS : 2 CA	11.8 ± 3.0
	2 D-CYS : 1 CA	14.5 ± 4.9

3.2.2 Structural Characterization of Chiral Carbon Dots

From the TEM analysis, the cysCDs were observed to be primarily amorphous in structure. The structural parameters of samples were probed and confirmed using XRD. In XRD, an incident beam of monochromatic x-rays from a copper Kα radiation source interacts with the atoms in the material producing elastically scattered x-rays. The constructive interference of these diffracted x-rays generates

36

the observed XRD peaks corresponding to the exact location of atoms and their electrons in the sample through Bragg's law.[126] Bragg's law relates the wavelength of incident x-ray (λ), spacing of the sample's atomic plane (d) and the angle of the diffracted x-rays (θ).[126]

The diffraction pattern of the cysCDs is dominated by a broad amorphous halo centered at approximately ~17° 2θ. This speaks to the poor crystalline structure and the absence of significant long-range order in the cysCDs. However, some crystalline reflections on top of the halo indicate that some ordered regions do indeed exist in the nanoparticle at 21°, 30°, 31°, 33° and 35° 2θ. These reflections could not be ascribed to the precursors, citric acid and cysteine (Figure 18) indicating that that their origin is due to the formation of the cysCDs and not any residual or unreacted precursors. Comparing the chiral cysCDs studied in this thesis to the other CDs and carbon materials in the literature, the reflections centered at 21° 2θ can be assigned to the (002) plane of graphitic crystalline structures.[78,113,127–129] The high background intensity of the cysCD sample indicates the highly disordered structures are also present in the system.

These sharp crystalline reflections can be observed for the cysCDs synthesized at 160 °C, 180 °C and 200 °C; however, at 220 °C, the cysCDs only have an amorphous halo (Appendix Figure A 5). Similarly, these reflections can also be observed following synthesis at 160 °C at 5 and 10 mins, but only an amorphous halo can be noted after a 15-min reaction time (Appendix Figure A 6). Modifying the precursor ratio and specifically increasing the achiral citric acid concentration resulted in a loss of crystallinity (Appendix Figure A 7).
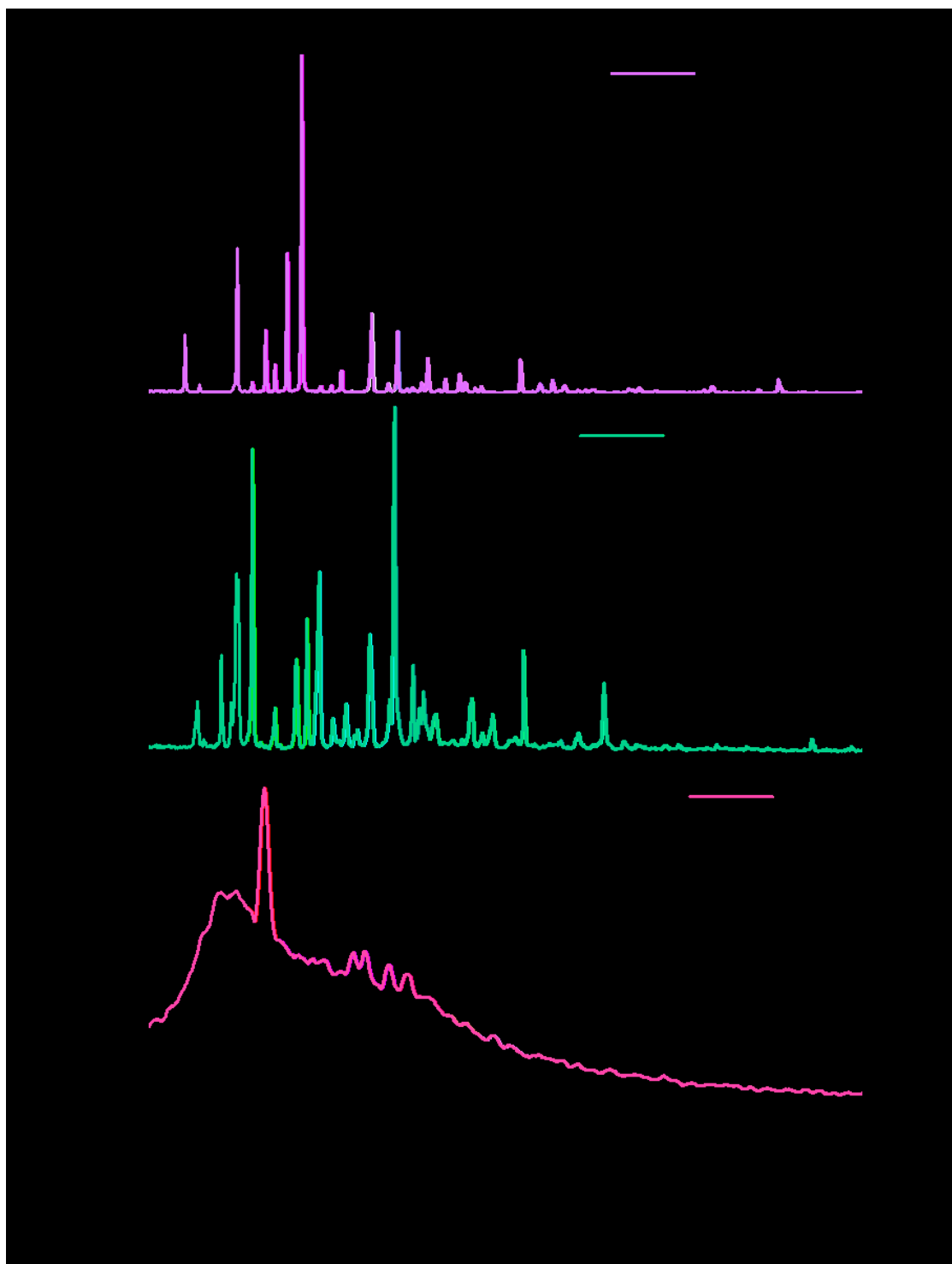
Figure 18. XRD analysis of precursors cysteine and citric acid, as well as the synthesized cysCDs. The precursors are crystalline in nature as evidenced by the sharp reflections in the spectra. The cysCDs show crystalline reflections on top of an amorphous halo at ~21° (2θ) corresponding to the (002) peak of graphene. Furthermore, the sharp peaks decorating the halo indicate some ordered crystalline features in the cysCDs.

3.3 Physical Characterizations of Chiral Carbon Dots at Various Reaction Parameters

3.3.1 Determination of Elemental Composition of Chiral Carbon Dots

Having introduced the importance of functional groups in dictating the physico-optical properties of the CDs, the composition of the cysCDs was studied using CHNSO analysis. This elemental analysis requires combustion of the CDs with oxygen, and the evolved gas species are then monitored using traps to determine the elements carbon, hydrogen, nitrogen and sulfur.

The percent compositions of the cysCDs are summarized in Table 2. The different cysCD systems indicate a high percentage of ~50% oxygen atoms and a proportionally high percentage of ~6% hydrogen atoms for a conjugated system. This elevated percentage of oxygen and hydrogen atoms is largely due to the hygroscopic nature of the cysCDs that can trap water molecules. Disregarding the percentages of oxygen and hydrogen, the cysCDs are primarily composed on carbon atoms followed by nitrogen and sulfur atoms.

From Table 2, an increasing ratio of hydrogen, nitrogen, sulfur and oxygen atoms and a decreasing ratio of carbon atoms was noted in the cysCDs as a function of increasing reaction temperature. This trend could be a result of cysteine moieties getting further incorporated into the nanoparticle at higher temperatures, as cysteine decomposes at a higher temperature than citric acid. With respect to reaction time, the ratios of nitrogen and sulfur increased with increasing time suggesting again a greater cysteine decomposition. Similarly, with an increasing reaction time, an increase was also noted for sulfur ratio and a decrease was noted for hydrogen and oxygen ratios. As expected, a greater ratio of sulfur and nitrogen is seen in the cysCDs with a doubled cysteine ratio as more cysteine is available for incorporation in the dots. A greater citric acid ratio during synthesis resulted in cysCDs with a greater ratio of carbon as more citric acid is available during synthesis.

Table 2. Summary of the elemental composition of cysCDs, determined by CHNSO analysis, following preparation using various reaction parameters.

		% C	% H	% N	% S	% O
Temperature **(**All reactions were done at 5 mins)	**160 °C**	36.7	5.65	9.66	1.37	46.6
	180 °C	35.4	6.09	10.6	0.68	47.3
	200 °C	32.2	6.21	11.4	1.28	48.9
	220 °C	31.8	6.27	11.4	1.47	49.0
Time (All reactions were done at 160 °C)	**5 mins**	36.7	5.65	9.66	1.37	46.6
	10 mins	36.7	5.62	10.2	2.96	44.5
	15 mins	37.0	5.27	9.88	5.38	42.5
Ratio (All reactions were done at 160 °C- 5mins)	**1 L-CYS : 1 CA**	36.7	5.62	10.2	2.96	44.5
	1 L-L- CYS : 2 CA	39.3	5.42	9.75	3.06	42.7
	2 L-CYS : 1 CA	37.1	5.85	11.2	5.05	40.8

3.3.2 Characterization of Surface Groups on the Chiral Carbon Dots

The surface of the chiral cysCDs was examined by FT-IR spectroscopy as a mean of understanding the surface chemical composition. FT-IR is a useful technique to identify the polar functionalities decorating the surface of the cysCDs. knowing the functional groups on the surface help gain a better understanding of how the cysCDs interact with their environment.

The functional groups present in the CDs mimic the functional groups present in the precursors, cysteine and citric acid (Figure 19). However, the transformation of the precursors to the nanoparticle is evident from the appearance of new functional groups that have resulted from the reactions between citric acid and cysteine, and by the position and shape of these bands. The features of the band are dependent on the vibrational energy that is determined by Hooke's Law which states a change in the mass, or the force constant will affect the vibrational frequency. According to the equation, a functional group attached to a higher mass object such as a dot will have a reduced vibrational frequency causing changes in the band appearance.[130] Similarly, an increase in the force constant which is directly proportional to bond strength will cause the bands to shift to higher frequencies.[130] A system that is conjugated, as seen in cysCDs, decreases the overall bond strength, and as such the position of the vibrational band shifts to lower frequencies.[130] In contrast to simple molecules, the cysCDs also have a broader appearance due to the complex environment and the intermolecular interactions felt by their chemical bond.

The FT-IR spectra of chiral precursor cysteine (Figure 19 a) have well-defined, and sharp stretching vibrations present at 3100 cm^{-1} and 2950 cm^{-1}, as well as bending vibrations at 1570 cm^{-1} and 1540 cm^{-1} indicative of N-H bonds and C-N stretching at 1060 cm^{-1} in primary amines. A small band at 2550 cm^{-1} is noted and is due to the S-H stretching frequency of thiols. The presence of carboxylic acids is evidenced by bands at 3200, 1613, 1423, and 1298 cm^{-1} corresponding to the broad O-H stretching, the C=O stretching, C-O-H bending and C-O stretching

vibrations, respectively. Moreover, sp^3 C-H stretching vibrations can be identified at 2800 cm^{-1} while the corresponding bending is noted at 1400 cm^{-1}. Similarly, citric acid (Figure 19 b) also has sharp bands characteristic of its distinct functional groups; the carboxylic acids can be identified by bands at 3200, 1700, 1427, and 1140 cm^{-1} corresponding to the broad O-H stretching, the C=O stretching, C-O-H bending and C-O stretching vibrations, respectively. The alcohol group can be seen at the stretching vibrations at 3500 cm^{-1} and out of plane bending at 700 cm^{-1}. The sp^3 C-H bending vibrations are observed at 1400 cm^{-1}.

Similar functional groups relative to the precursors are present in the cysCDs. (Figure 19 c,d). A possible primary amine or an amide group can be identified at stretching vibrations of 3170 cm^{-1} and 3065 cm^{-1} and bending vibrations at 1560 cm^{-1} due to the N-H bond. The C-N bond stretching can be observed at 1400 cm^{-1}. The peak at 1700 cm^{-1} is a C=O stretch that could arise from both an amide, or a conjugated carboxylic acid. The broad O-H stretch is seen at 3000 cm^{-1} and the C-O stretch is at 1200 cm^{-1} for a carboxylic acid. The bands at 2500 cm^{-1} and 1200 cm^{-1} correspond to the symmetric S-H stretch of thiols and an asymmetric S=O stretch. The dual vibrations at ~1000 cm^{-1} are ascribed to the symmetric S=O stretch of sulfone groups. The presence of a conjugated system can be identified by the C=C stretch at 1400 cm^{-1} and the corresponding sp^2 C-H stretch typically found at 3100 cm^{-1}, as well as the 1000 cm^{-1} bending vibration. The sp^3 C-H can be identified at 1300 cm^{-1} for bending and at 2700 cm^{-1} for stretching vibrations. As such, the cysCDs have a plethora of functional groups suggesting a complex system is present and they can dictate properties such as dispersibility in solvents, photoluminescence, stability *etc.*

The surface functional groups in the cysCDs were not significantly impacted by the variation in synthesis temperature (Figure 20). However, the sp^2 C-H stretches at ~3100 cm^{-1} became more defined at higher reaction temperatures possibly suggesting the formation of a more defined aromatic system in comparison to the CDs prepared at lower temperatures. Similar observations can be made following an in increase in reaction time (Figure 21). The stretches at 3100 cm^{-1} are better

defined in comparison to those of the CDs prepared at shorter reaction times. The precursor ratio has a greater effect on the IR frequencies absorbed by the bonds as evidenced by the broadening and shifting of the peaks (Figure 22). A significant increase is observed in the intensity of the C=O stretch at 1700 cm^{-1} in comparison to the C=C stretch at 1400 cm^{-1}. The N-H stretches have shifted to higher frequencies possibly due to a greater presence of sp^2 C-H than sp^{3}C-H. In addition, the sharp sp^3 C-H bending peaks at 1300 cm^{-1} have diminished further signifying the conversion of sp^3 C-H to sp^2 C-H as a result of the increased conjugation of the nanoparticle core.
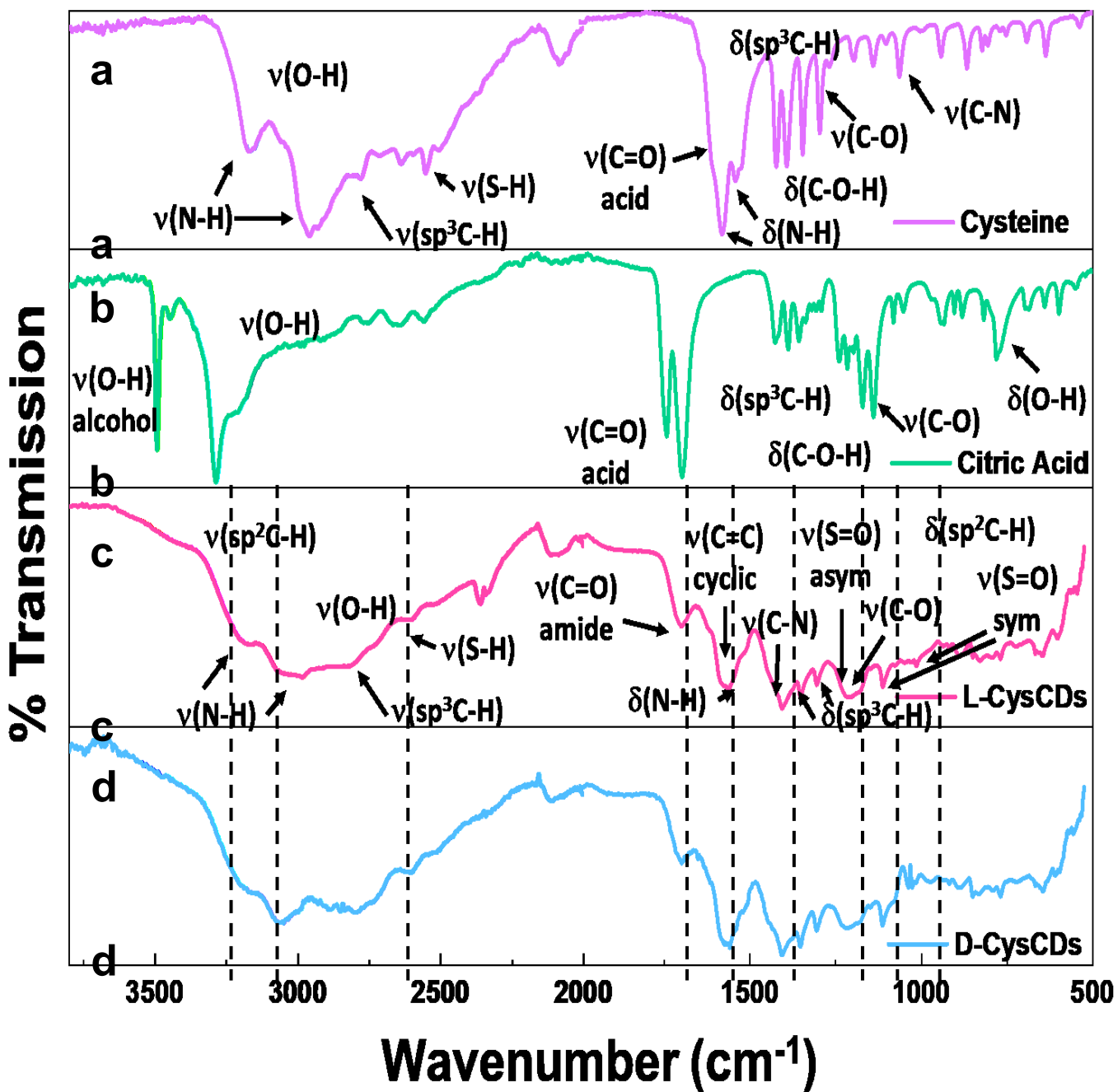
Figure 19. FTIR spectra of precursors cysteine and citric acid with the L-cysCDs and D-cysCDs. The functional groups present in the CDs are a mix of functional groups observed in the precursors. The cysCDs are primarily composed of functional groups such as carboxylic acids, amides, amines and sulfones. The cysCDs synthesized from enantiomers of cysteine have similar FTIR spectra indicating similar functionalities on the enantiomeric nanoparticles.

44
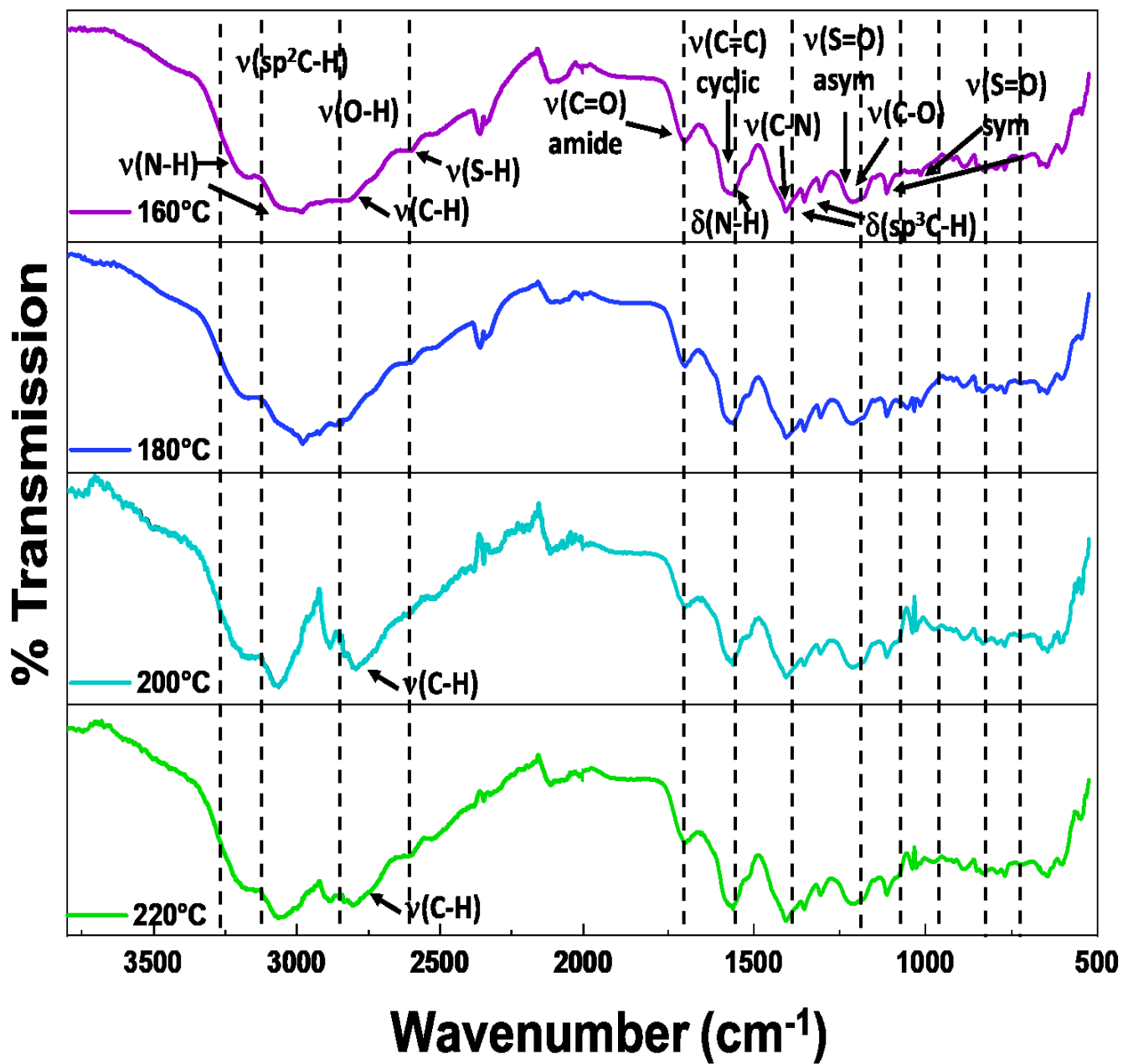
Figure 20. FTIR spectra of the cysCDs as a function of increasing reaction temperature. The overall functional groups on the cysCDs remain the same with the change in temperature as indicated by the spectra.
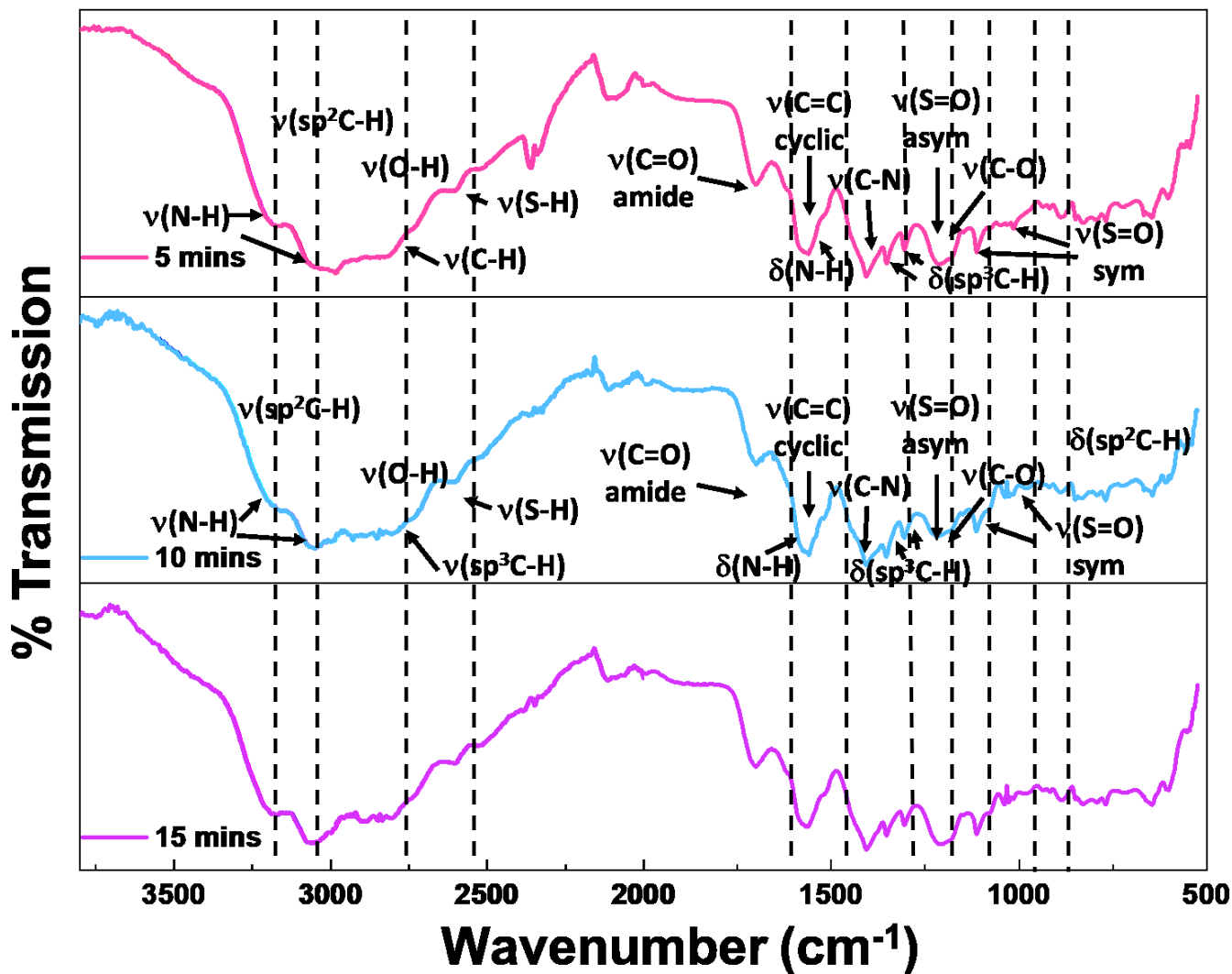
Figure 21. FTIR spectra of the CDs at various reaction times. Again, the functional groups remain similar with increasing reaction time.
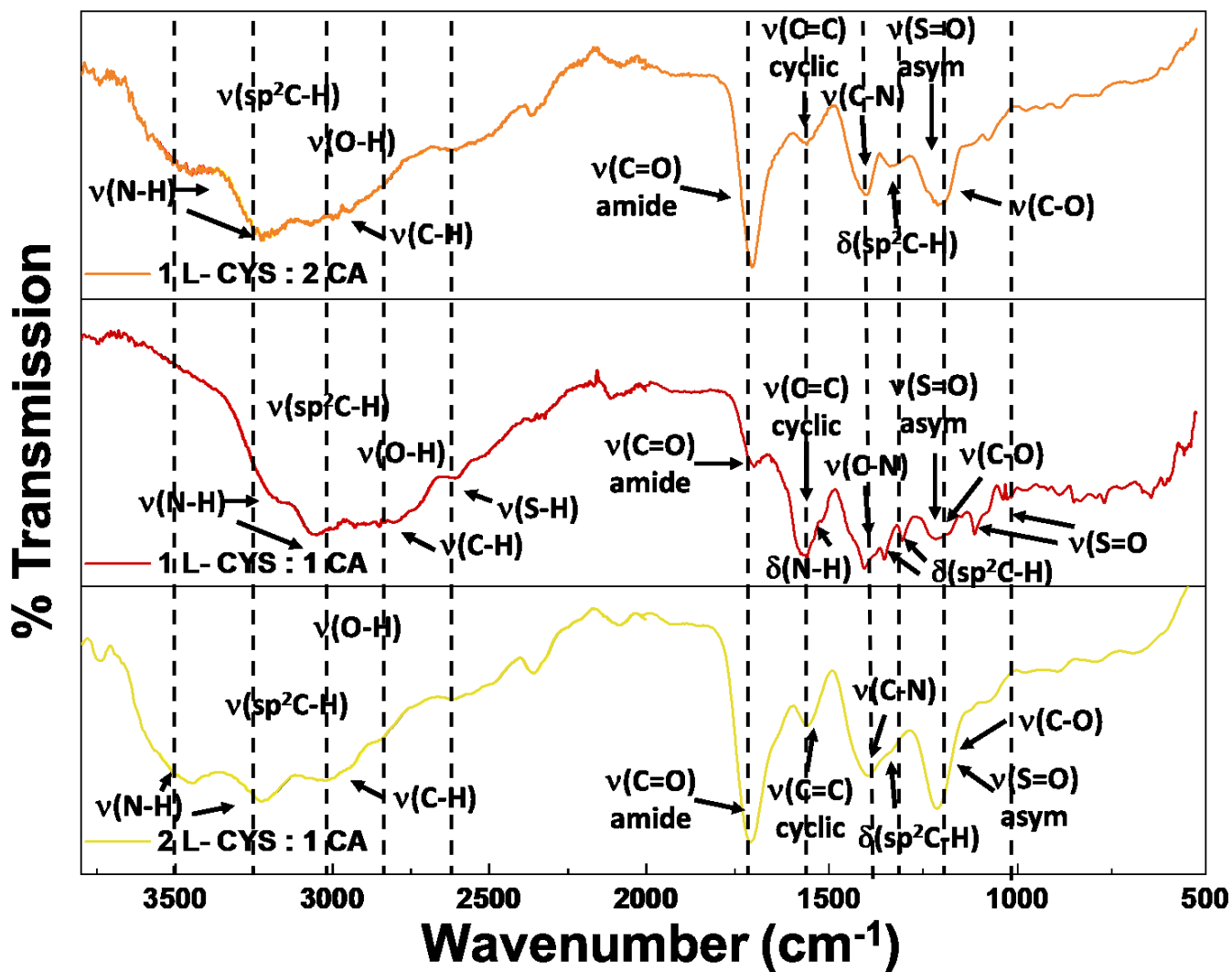
Figure 22. FTIR spectra of cysCDs prepared using different precursor ratios. The spectra change with the change in ratio, the peaks have become broader and the intensity of the peaks change.

3.3.3 Characterization of Chemical Bonds in Chiral Carbon Dots

The findings of the FT-IR were further validated by XPS through confirming the functional groups in cysCDs. In this technique, the samples are irradiated with x-rays causing the core electrons to be ejected according to the photoelectric effect.[131] The energy required to eject these electrons correspond to the binding energy of specific elements and their oxidation states.[131] XPS is often used to analyze the surface of the materials due to a penetration depth of approximately 10 nm. However, owing to the small size of the cysCDs, XPS can be used to probe further than the surface of the CDs and determine its chemical composition.

A representative survey scan of the cysCDs at 160°C and 10 min reaction time shows peaks at binding energies of 533.08 eV, 401.08 eV, 289.08 eV and 166.08 eV corresponding to oxygen (O 1s), nitrogen (N 1s), carbon (C 1s) and sulfur (S 2p), respectively (Figure 23). These elements were also previously indicated CHNSO of the cysCDs. Deconvoluted high-resolution scans of the O 1s spectrum indicate the presence of the functional groups C–OH/C–OC and C=O at binding energies of 533.48 eV and 532.12 eV (Figure 24 a). The nitrogen groups can be observed at binding energies of 402.04 eV and 400.48 eV, indicating functional groups of the pyrrolic N/NH$_2$ and graphitic N functionalities, respectively (Figure 24 b). The C 1s spectrum contained peaks with binding energies of 289.02 eV, 287.04 eV, and 285.28 eV that correspond to the C-C/C=C, C-N/C-S, and C=O functional groups present in the cysCDs (Figure 24 c). Lastly, the S=O and S-H groups can be identified in the high-resolution scan of S 2p spectrum at 164.66 eV and 163.58 eV, respectively (Figure 24 d). As such, the functionalities identified from XPS corroborate the functional groups from FT-IR analyses.
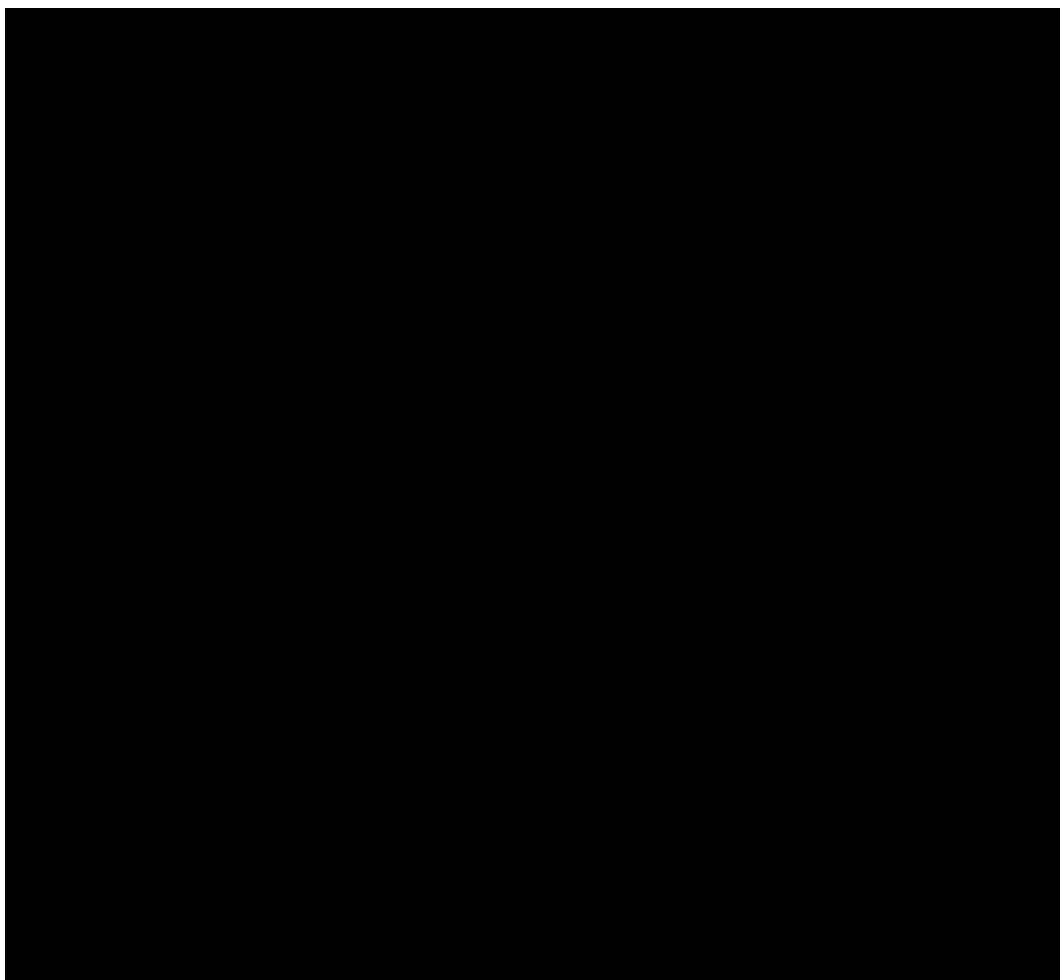
Figure 23. XPS survey scan of cysCDs. The binding energies at 533.08 eV, 401.08 eV, 289.08 eV and 166.08 eV correspond to elements nitrogen (oxygen (O 1s), N 1s), carbon (C 1s) and sulfur (S 2p), respectively.
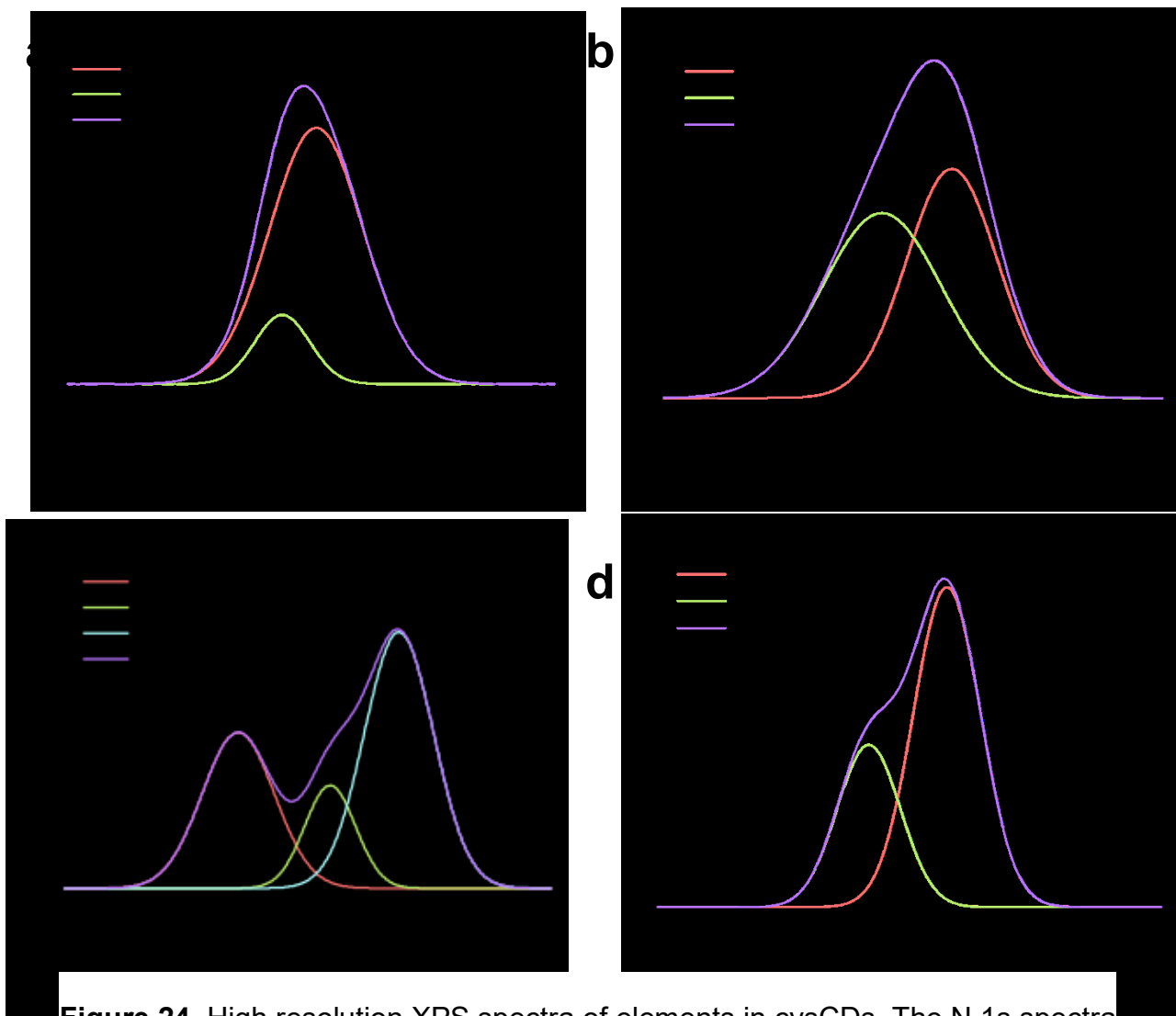
Figure 24. High resolution XPS spectra of elements in cysCDs. The N 1s spectra (a) indicates functionalities such as pyrrolic N/NH$_2$ and graphitic N; C–OH/C–OC and C=O groups can be seen in the O 1s spectra (b); C 1s spectra (c) indicates C/C=C, C-N/C-S, and C=O functional group and the S 2p spectra (d) shows S=O and S-H groups.

The effect of reaction time at 160 °C was further investigated by XPS and the results indicate similar functional groups present in the different cysCD systems (Figure 25). However, the quantity of the functional groups varies as function of reaction time. At longer reaction times, the primary oxygen-containing groups in the cysCDs change from C-OH/C-O-C groups to C=O groups suggesting an increase in carboxylic acid functionalities. The quantity of graphitic N and pyrrolic N/NH$_2$ groups remained relatively similar in the cysCDs. The longer reaction times increased the conjugation in the cysCDs evidenced by an increase of C-C/C=C
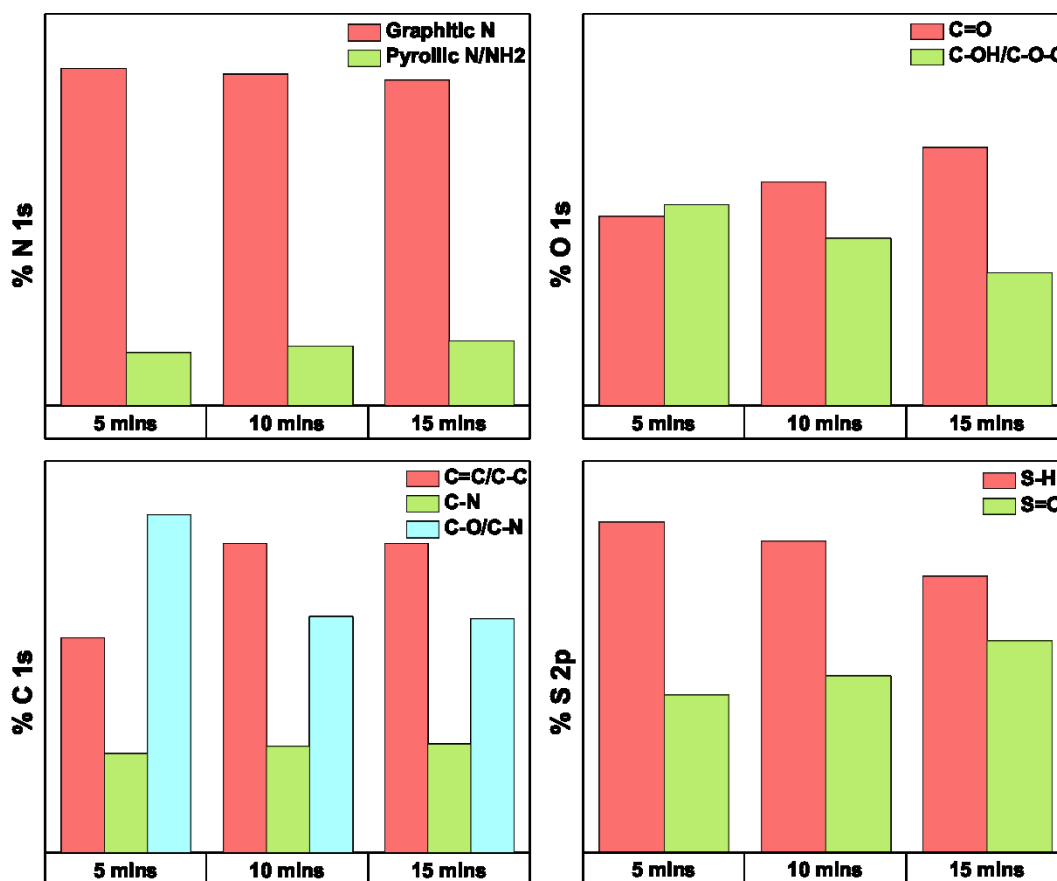
Figure 25. The effect of synthesis time on the functional group in cysCDs. The functional groups from N 1s spectra show no significant change. In O 1s, the C=O groups increased with increasing reaction time while C-OH/C-O-C groups decreased. An increase in C=C/C-C functionalities were also observed in C 1s with increasing time indicating hybridization. The S 2p spectra shows an increasing transformation towards S=O with increasing time.

and a decrease of C=O functional groups. The C-N/C-S groups remained unchanged in the CDs as the reaction time was increased. Furthermore, an increase in S=O groups and a corresponding decrease in S-H groups is observed suggesting that S-H from cysteine is transformed and incorporated as S=O in the CDs.

3.3.4 Determination of Thermal Stability in Chiral Carbon Dots

The thermal stability of the cysCDs is governed by the chemical composition of the cysCDs. Using thermogravimetric analysis (TGA), the presence of the various core and surface groups was once again probed. In such analysis, the mass of the sample is monitored as function of change in temperature. Typically, the mass decreases with an increase in temperature due to transformations in the sample, which may include evaporation, oxidation/reduction, or decomposition. The rate at which the sample decomposes sheds light on its composition as various structures and functional groups possess different thermal stability.

From the TGA analysis of the cysCDs, a decrease in the mass was observed as a function of increasing temperature. The weight loss occurred in a multi-step manner as indicated by the multiple plateaus and further implying that the chiral cysCDs are comprised of multiple functional groups and structures. The oxidation temperature of the chiral cysCDs, determined by the derivative curve, is approximately 260 °C and it is indicative of the overall thermal stability of the system. The stability and the TGA profile of the cysCD is similar to the CDs of similar composition reported in the literature.[132]

A primary loss of mass at the temperature range of 30-150 °C corresponds to the loss of residual moisture and solvent adsorbed on the surface following synthesis and purification.[78] Subsequent larger weight losses occurring between ~200-500 °C were ascribed to the decomposition of the various functional groups on the surface. Typically, oxygen, nitrogen and sulphur containing moieties undergo decomposition at such a temperature range. Oxygen containing functional groups such as carboxyls, lactones and anhydrides decompose at a lower temperature

range of 100-500 °C releasing CO_2.[78,133] At temperatures greater than 500 °C, phenols, ether and carbonyls begin to decompose releasing CO.

The thermal stability of nitrogen in carbon nanomaterials varies depending on its character. For example, graphitic nitrogens are thermally stable up to 700 °C in comparison to pyridinic nitrogen.[78,129,134] Moreover, while sulfur functional groups have been shown to decompose at temperature ranges of 300-400 °C in the form of H_2S, sulfur that has been incorporated into the carbon backbone can remain in the sample at temperatures as high as 800 °C.[135,136] Lastly, the thermal stability of carbonaceous materials depends on the degree of order in its structure. Amorphous or disordered carbon structures decompose around 350 °C, whereas non-defective and higher ordered structures decompose at temperatures near 650 °C[134]. As such, TGA profiles of the cysCDs do not always reach a 100% mass of loss due to the ordered structures and incorporation of sulfur in the carbon backbone.[136] These findings are supported by the previous analysis of the cysCDs with CHNSO, XPS and FT-IR.

The analysis of the cysCDs at different reaction temperatures by TGA suggests that the composition of the cysCDs is very similar to each other in terms of the functional groups and structure (Figure 26).The cysCDs synthesized at 220°C exhibit a weight loss at 330 °C that is not observed in the other cysCDs prepared at lower synthesis temperatures. Similarly, with an increase in reaction time, the cysCDs also exhibit a sharper weight loss at 330 °C and a decrease at 200 °C suggesting a change in the functional groups and structure of the CDs (Figure 27). Lastly, upon variation of the precursor ratio, subtle changes of the weight loss occurring over the 200 °C indicates minor changes to the composition of the cysCDs (Figure 28).
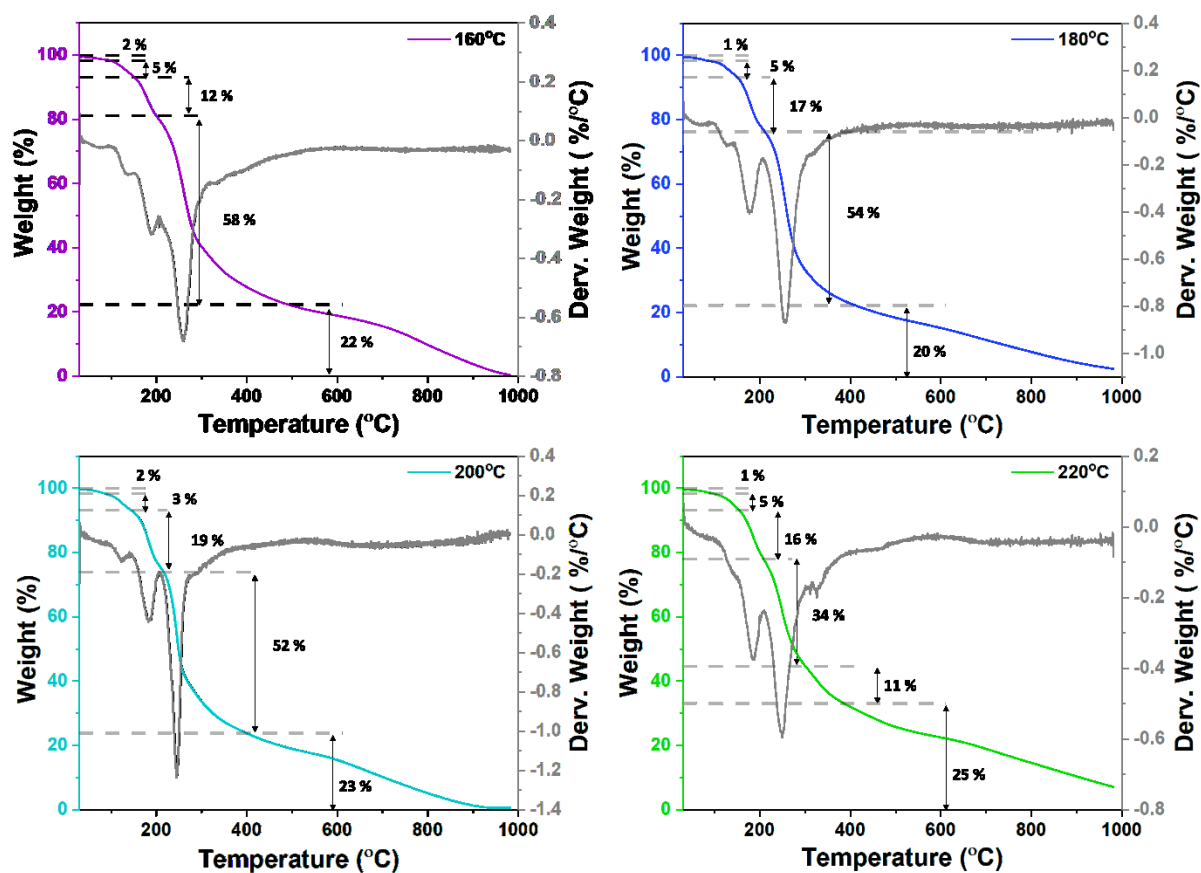
Figure 26. TGA of cysCDs prepared at different reaction temperatures. It is evident that there are some changes in the TGA profiles with increasing synthesis temperature suggesting changes in the nanoparticle composition. The multiple weight loss events signify multiple evaporation and decomposition steps associated with the loss of functional groups on the surface.
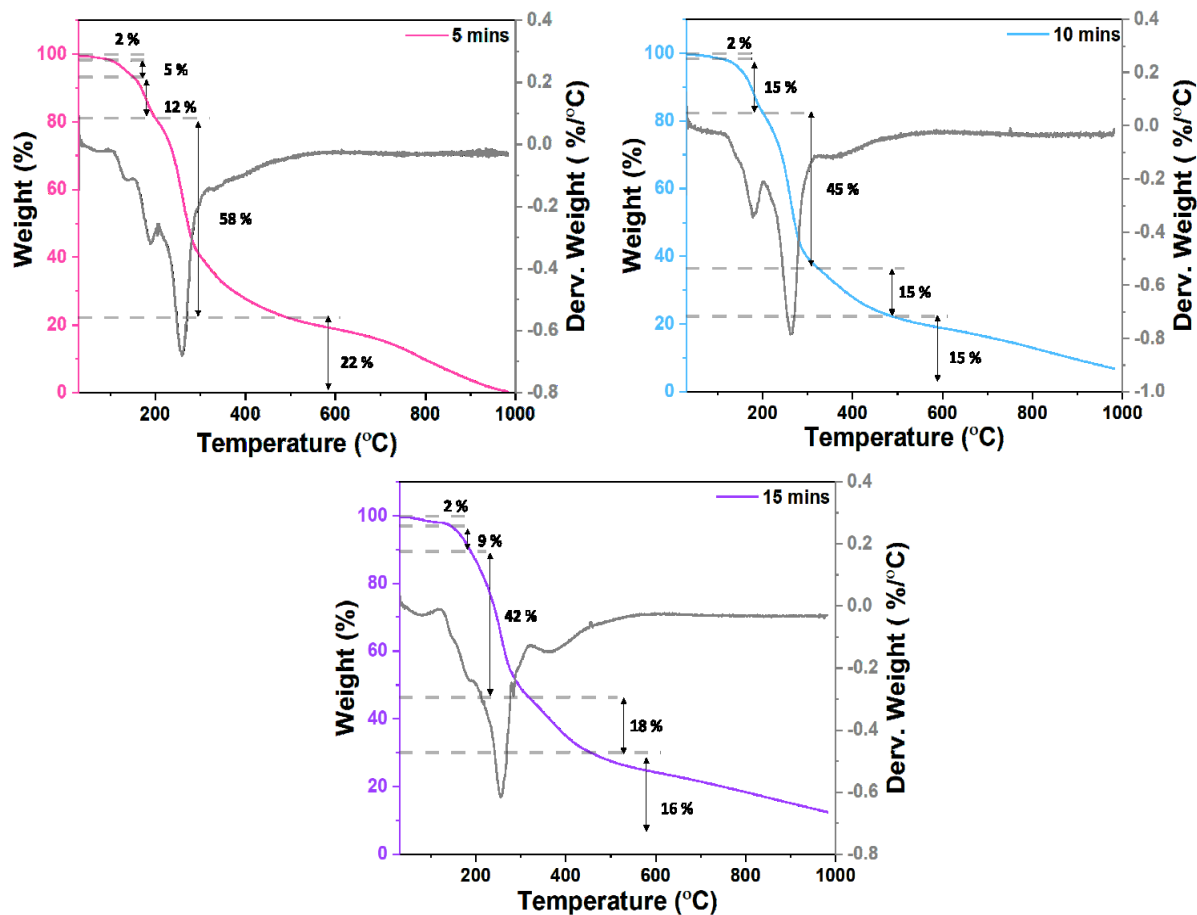
Figure 27. TGA of cysCDs prepared at different reaction times. The small changes in the weight loss profiles is an indication of changes in the nanoparticle composition as a function of increasing reaction time.
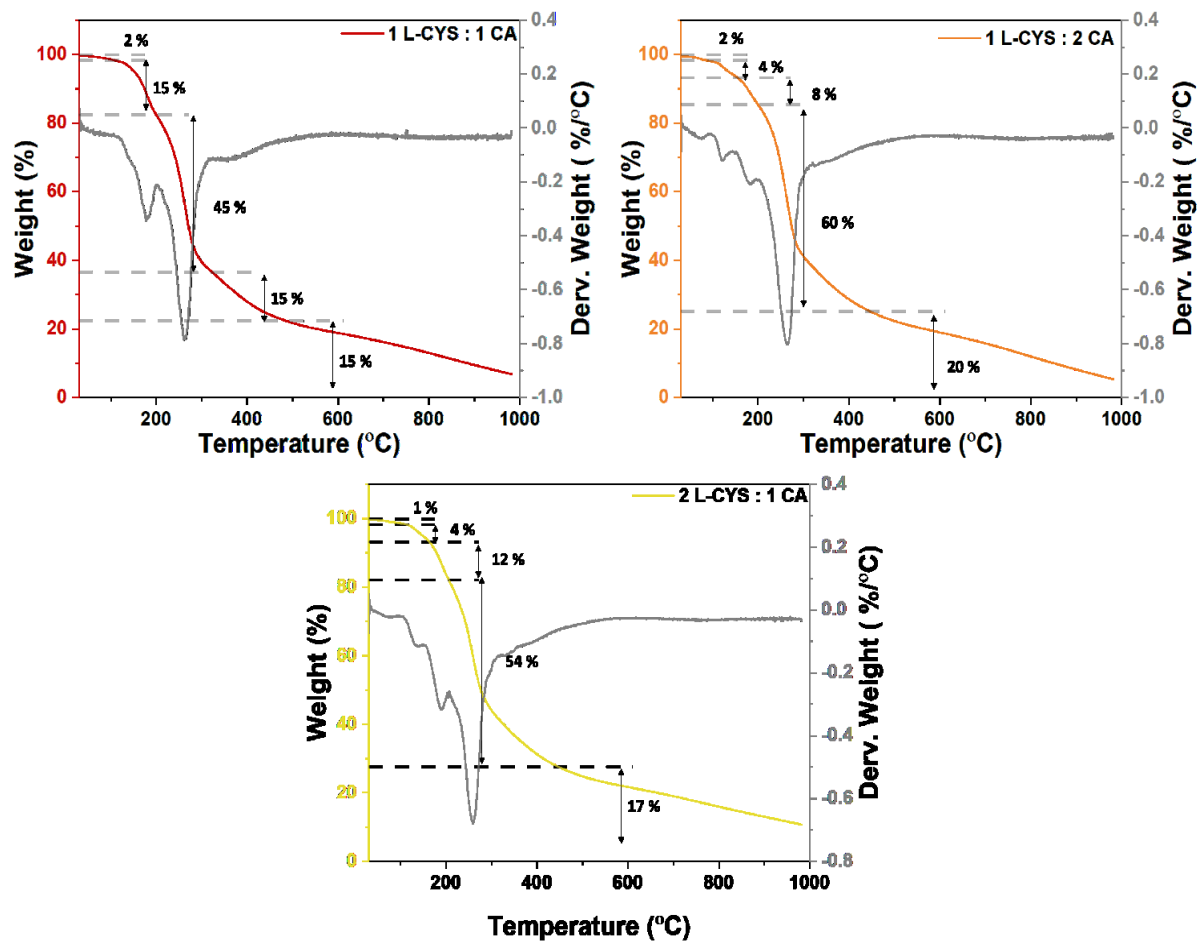
Figure 28. TGA of cysCDs prepared at different precursor ratios. The small changes in the weight loss profile is an indication of changes in nanoparticle composition.

3.4 Optical Characterizations of cysCDs at Various Reaction Parameters

3.4.1 UV-Vis Characterization of Chiral Carbon Dots

With a deeper understanding of the physical and chemical characteristics of cysCDs, the optical properties were studied to investigate the effects of reaction parameters. The optical properties of the cysCDs were first analyzed using UV-Vis spectroscopy. In this technique, the samples were subjected to electromagnetic radiation in the ultraviolet and visible regions. The absorbance of light by the sample is indicative of the electronic transitions that occur from the ground state to the excited state. Furthermore, these electronic transitions could be assigned to specific functional groups within the CD.

The UV-Vis spectra of the purified chiral cysCDs were analyzed as a colloidal aqueous dispersion. The cysCDs are brown powders, in solid form, and a dispersion in water produces nearly transparent to yellow coloured samples depending on the concentration. The samples showed two distinct absorption bands centred at ~250 nm and ~350 nm. The ~250 nm band is characteristic of the $\pi \rightarrow \pi^*$ transition of the aromatic sp^2 domains that are indicative of the conjugated network. The $n \rightarrow \pi^*$ transition is assigned to the band at ~350 nm associated with functional groups such as C=O, as well as the C=N/C=S.

The different reaction parameters such as temperature, time and precursor ratios did not have any significant effect on the UV-Vis spectra of the cysCDs (Figure 29). The lack of change in the absorption spectra is due to the fact that the CD structure and its functional groups remain similar within the constraints of the different reaction parameters used. Moreover, as expected, the cysCDs synthesized using the different enantiomers of L- and D- cysteine denoted as L- and D-cysCDs, respectively, show similar absorbance profiles (Figure 29 d), since the chemical composition of enantiomeric precursors is identical.
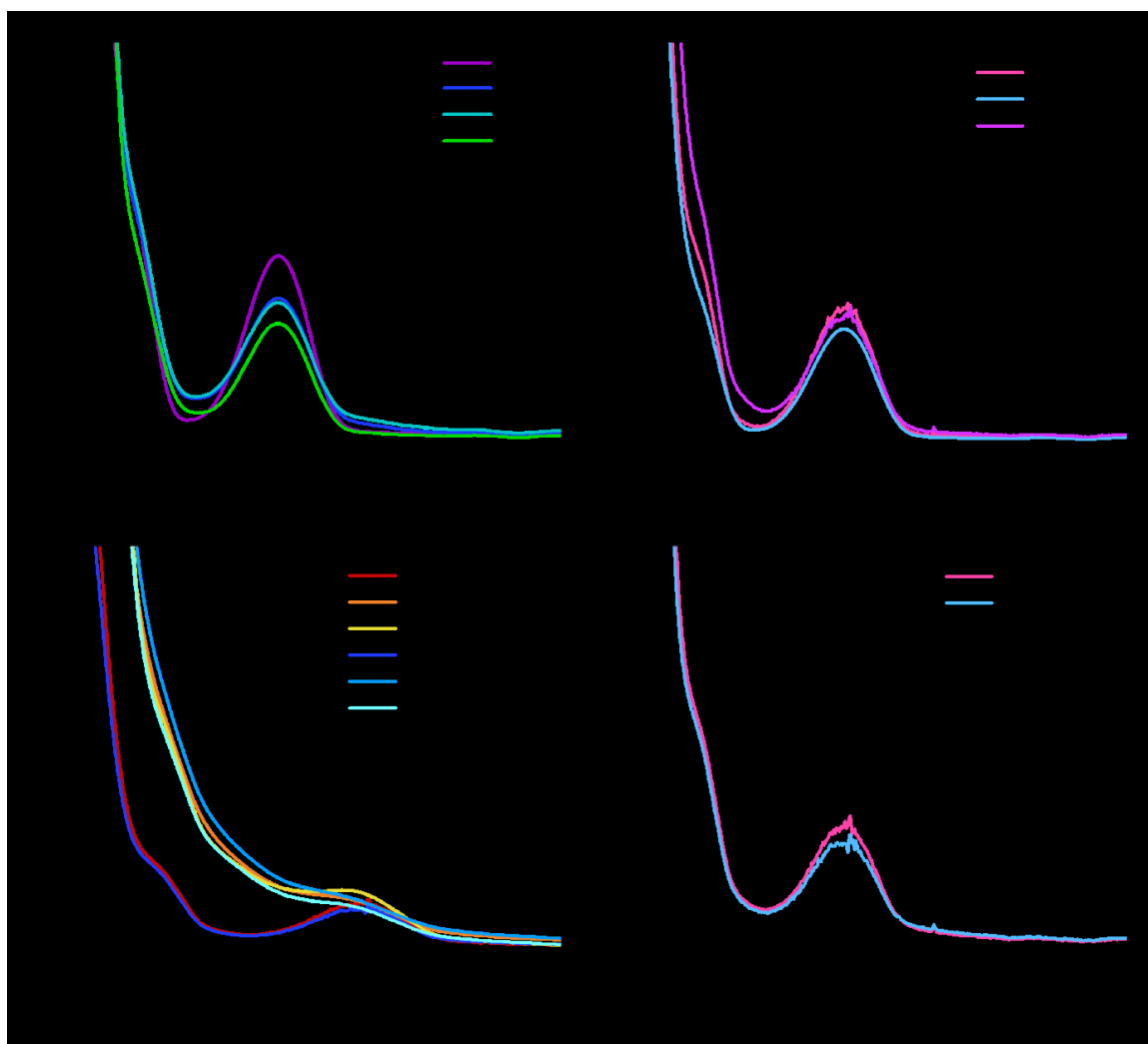
Figure 29. Absorbance spectra of the cysCDs at various temperature (a), time (b) and precursor ratios (c), as well as absorbance spectra for the enantiomeric cysCDs (d). The CDs have an absorbance at ~250 nm and ~350 nm corresponding to $\pi \to \pi^*$ transition of the aromatic sp^2 domains and $n \to \pi^*$ transitions of C=O and C=N/C=S functionalities, respectively.

3.4.2 Fluorescent Properties of Chiral Carbon Dots

Following the UV-Vis characterizations, the fascinating fluorescent properties of the cysCDs were examined using fluorescence spectroscopy. To probe the fluorescence properties, photons from an excitation source are used to excite the sample from the ground state to a higher lying excited electronic state with multiple vibrational levels. The sample undergoes a non-radiative relaxation to the lowest vibrational level in that excited electronic state. The fluorescence of the sample is observed when a photon of longer wavelength and lower energy is emitted, and the excited sample relaxes back to its ground state.

The chiral cysCDs aqueous dispersions exhibited an intense blue emission easily visualized by the naked eye, upon excitation by a hand-held UV light (365 nm). Using a spectrophotometer, the emission maximum of the cysCDs was observed at 420 nm following a 350 nm excitation wavelength. In addition, the cysCDs display an excitation independent emission profile, such that a change in excitation wavelength does not change the fluorescence wavelength of the cysCDs. The observed profile is owing to the surface passivation of the cysCDs by electron donating functional groups, such as amines, amides, hydroxy groups, among others, that reduce surface defects and traps and increase radiative recombination.[82]

At higher reaction temperatures and longer reaction times, the luminescent profile of the cysCDs remains the same. However, the emission intensity of the cysCDs increases with increasing synthesis temperature from 160 °C to 220 °C (Figure 30 a), as well as when reaction time is increased from 5 to 15 min (Figure 30 b). At elevated reaction temperatures and longer synthesis times, the conditions afford significant decomposition of the precursors and their incorporation into a conjugated CD system with multiple surface functionalities. This process is thought to decrease the non-radiative pathways through a reduction of surface traps and surface defects, hence the increased intensities in emission.
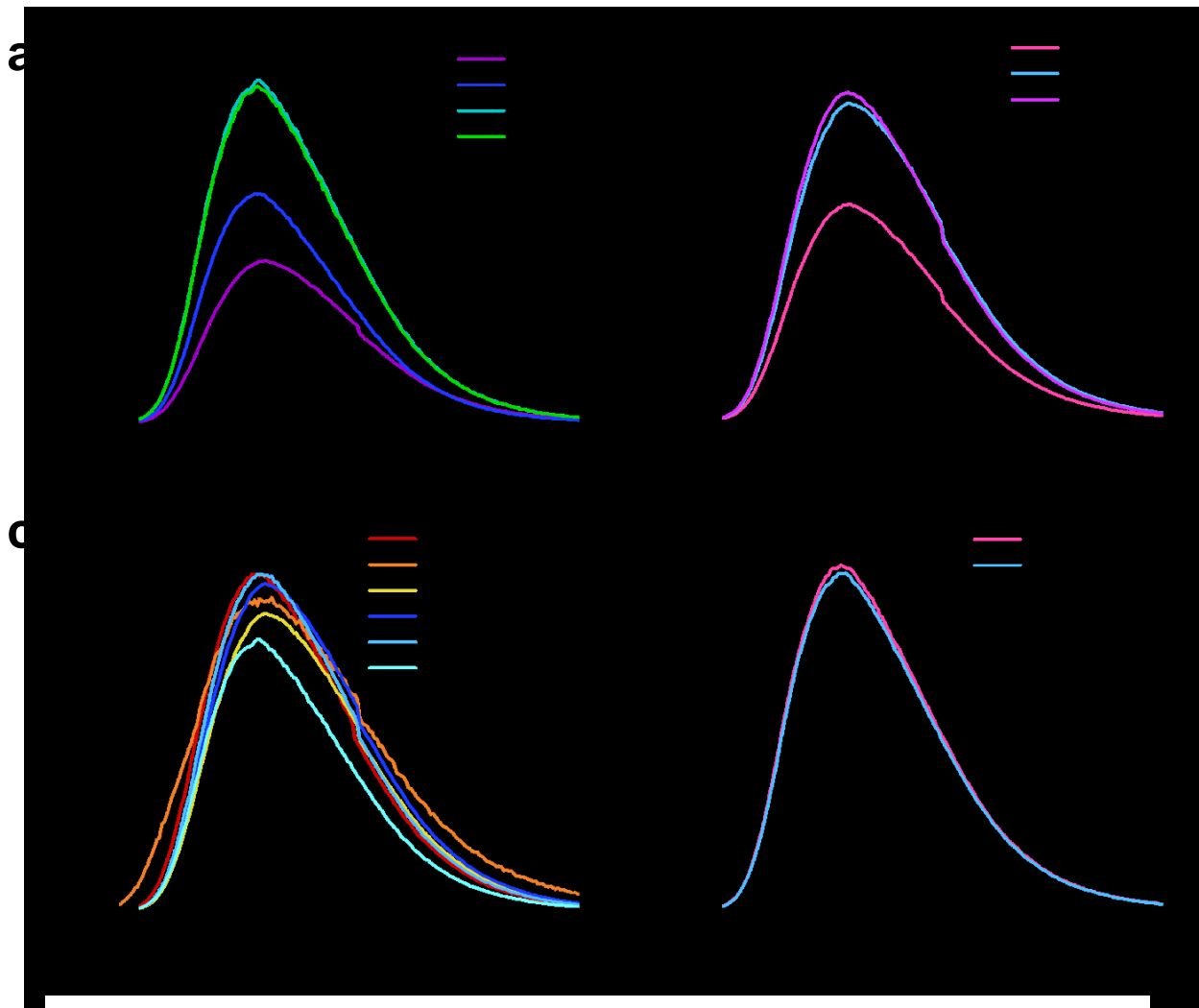
Figure 30. Fluorescence profiles of the CDs at various temperature (a), time (b), precursor ratios (c), and enantiomeric CDs (d). The CDs have an excitation maximum at 350nm following an emission maximum at 420 nm. The CDs exhibit an excitation independent profile indicating surface passivation. The fluorescence intensity increases as function of increasing reaction temperature, time and cysteine ratio.

Furthermore, a decrease in the ratio of the cysteine precursor also results in a decrease in the fluorescence intensity, yet conversely, no significant changes are observed with an increased ratio (Figure 30 c). As such, the cysteine plays a major role in surface passivation of the CDs by introducing heteroatoms such as sulfur and nitrogen that could enhance the electron donation mechanism. It could also be postulated that the surface of the cysCDs is saturated with the functional groups, hence, the emission intensity of the nanoparticles did not change as

cysteine ratio was doubled. Moreover, the chiral cysCDs synthesized from L- and D-cysteine showed no significant differences in the fluorescence spectra (Figure 30 d). The CDs from the enantiomers do contain identical functional groups as determined by the physical properties and as such, they also display similar optical properties.

3.4.3 Circular Polarization Properties of Chiral Carbon Dots

In order to investigate the chiral properties of the dots, circular dichroism spectroscopy was used to analyze the cysCDs prepared from the chiral L- or D-cysteine precursors. The principle behind circular dichroism is similar to that of absorbance spectroscopy. In circular dichroism, the light absorbed is circularly polarized in both left and right-handed directions, using a polarizer and photoelastic modulator. When a sample is chiral, it is optically active; therefore, it interacts with left and right-handed circularly polarized light differently.

The circular dichroism spectra of cysCDs show prominent absorbance bands at 250 nm and 350 nm as observed in the absorbance spectra. In contrast, the cysteine precursor shows a single absorbance at approximately 210 nm signifying the transformation of the chiral precursor into a new system of chiral cysCD (Figure 31 a). As the reaction temperature is progressively increased from 160 to 220 °C, the residual chirality of the cysCDs decreases (Figure 31 b). Similarly, a prolonged reaction time from 5 to 15 min also decreases the residual chirality observed in the cysCDs (Figure 31 c). Once again, we reason these findings in that a greater decomposition of the chiral precursor arises at higher reaction temperatures and longer reaction times. Thus, the chiral moieties in the CDs are diminished.

The residual chirality of the cysCDs was also tuned according to the ratio of cysteine precursor (Figure 31 d). As the ratio of cysteine was increased relative to the achiral citric acid, a greater chiral signature was noted for the cysCDs. Conversely, following a decrease in this ratio, the cysCDs displayed a corresponding decrease in chirality. The ratio of chiral precursors strongly dictates the chirality observed in the nanoparticle. The presence of a larger concentration

of the chiral precursor during the synthesis produces cysCDs with higher residual chirality.

Following optimization efforts carried out on L-cysteine using various reaction parameters, the chiral cysCDs were synthesized using the more expensive D-cysteine and gave rise to D-cysCDs. The D-cysCDs exhibited the same absorbance bands at 250 nm and 350 nm as observed for the L-cysCDs from L-cysteine in the circular dichroism spectra. However, the optical activity of the D-cysCDs is a mirror image to the L-cysCDs demonstrating that the cysCDs are indeed chiral. The effect of the ratio is also observed in the D-cysCDs, as the ratio of D-cysteine is increased with respect to citric acid, an increased residual chiral signal is noted. Furthermore, cysCDs synthesized from a racemic mixture of the L-cysteine and D-cysteine does not show any optical activity as expected indicating an achiral nanoparticle.
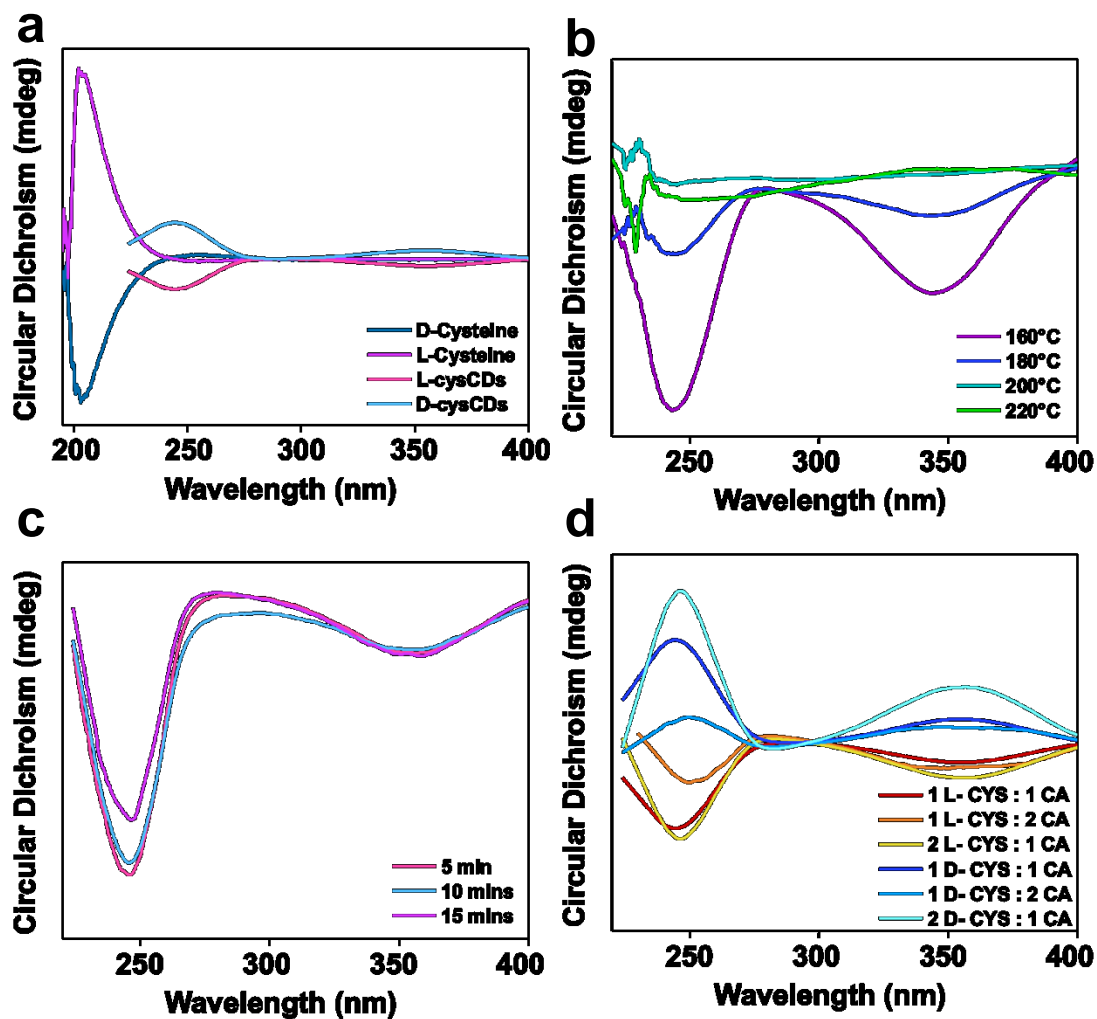
Figure 31. Circular dichroism of the CDs. The enantiomeric L-/D-cysCDs with the chiral precursors(a). The effect of synthesis temperature (b), time (c) and precursor ratios (d) on chirality of the cysCDs. The CDs show a decrease in chirality as temperature and time are increased suggesting a greater breakdown of the chiral precursor and chiral moieties during synthesis. An increase in chirality is observed with an increasing ratio of cysteine to citric acid. Furthermore, enantiomeric CDs were observed when synthesized from L and D-cysteine as reflected by the mirror images. The CDs are truly different from the precursor cysteine, which shows an absorbance at 210 nm.

3.5 Anti-microbial Properties of Chiral Carbon Dots

3.5.1 The Need for Novel Anti-bacterial Agents

As the chiral cysCDs retain stereochemistry form the chiral precursors, we also investigated their effect on biological systems. The biological world has evolved in an asymmetric manner and consequently, it interacts differently with chiral molecules. A proof of concept application was investigated using the chiral cysCDs as a potential anti-microbial agent.

Over the recent years, there has been growing concern of antibiotic resistance due to an increasing overuse and misuse of these medications. Antibiotic medications are used to treat bacterial infections and they prevent the spread of the disease through inhibition or termination of the bacterial growth. However, the gross overuse and misuse of the treatment has led to the development of antibiotic resistant bacteria. These bacteria become resistant to potent drugs by adaptation of their outer receptors, or structure such that they become unidentifiable. Furthermore, these bacteria can also develop mutations in their genetic make-up that enables them to resist multiple antibiotic treatments and pass on these mutations to future strains. As such, there is a rapidly emerging need to discover new antibiotics to tackle these resistant super bacteria.

3.5.2 Minimal Inhibitory Concentration Determination of Chiral Carbon Dots

Chiral L- and D-cysCDs were investigated as potential for antimicrobial agents in Gram-positive and Gram-negative bacteria. Gram-positive bacteria are single celled living organisms that are composed of a thick peptidoglycan layer and no outer lipid membrane. The gram-positive strains tested were *Bacillus subtilis* DSM10, *Burkholderia thailandensis* E264, and *Micrococcus luteus* DSM20030.

In contrast, Gram-negative bacteria is composed of a thin peptidoglycan layer and an outer lipid membrane with lipopolysaccharide molecules; these molecules are endotoxins that protect the bacteria from its environment. Therefore, Gram-negative bacteria is typically more resistant to antibiotics. The gram-negative

strains tested were *E. coli* ATCC25922 and MG1655, as well as *Klebsiella aerogenes* ATCC13048.

The inhibition of bacterial growth by the chiral L-cysCDs and D-cysCDs displayed stereoselectivity (Figure 32). Varying by both the bacterial strain tested and the chirality of the cysCDs, a concentration range of 0.25-4 mgmL^{-1} chiral CysCDs was tested for the inhibition of bacterial growth. The MIC findings are summarized in Table 3 for the various strains of bacteria. The MIC of L-cysCDs on gram positive bacteria, *B. subtilis*, *M. luteus* and *B. thailandensis*, was determined to be 4 mgmL^{-1}, 2 mgmL^{-1} and 1 mgmL^{-1} respectively. The MIC of D-cysCDs was determined to be 1 mgmL^{-1} for all gram-positive strains except *M. luteus*, where a MIC of 0.5 mgmL^{-1} was observed. In gram negative bacteria, the MIC was determined to be 0.25 mgmL^{-1} for *K. aerogenes* and 4 mgmL^{-1} for *E.coli* in both liquid culture and solid agar plates. The D-cysCDs had a MIC of 1 mgmL^{-1} for *K. aerogenes* and 2 mgmL^{-1} in *E.coli* strains. The gram-negative strains did require a larger concentration of chiral cysCDs for bacterial inhibition in comparison to gram-positive bacteria due to the additional outer cell wall.
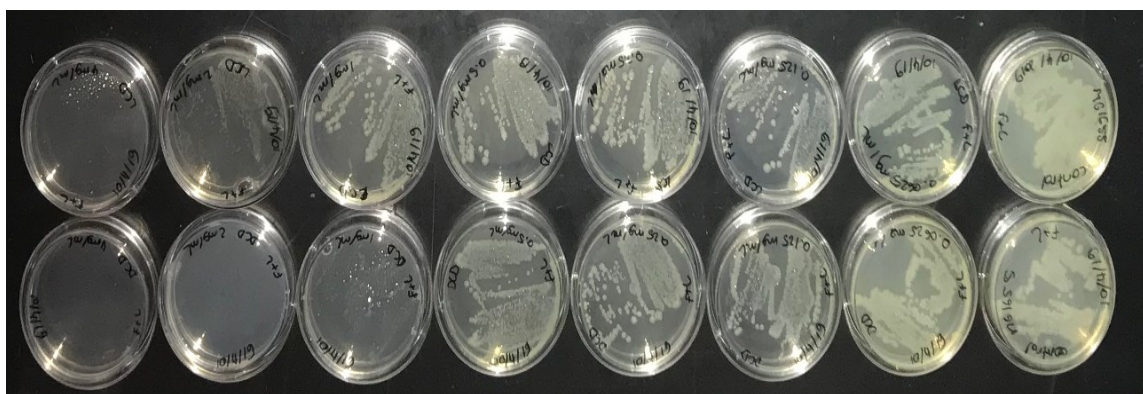
Figure 32. The anti-microbial properties of chiral cysCDs. The top row (from left to right) exhibits the antibacterial property of D-cysCDs at decreasing concentrations inhibiting E.Coli (MG 1655) growth at an optimal concentration of 2 mgmL^{-1}. The bottom row (from left to right) exhibits the antibacterial property of L-cysCDs at decreasing concentration inhibiting E.Coli growth at an optimal concentration of 4 mgmL^{-1}.

Table 3. MIC data of exposure of 1:1 L-cysCD and 1:1 D-cysCD on 6 bacterial strains.

Bacterial Strain	MIC L-CysCD (mg/mL)	MIC D-CysCD (mg/mL)
M. luteus DSM20030	2	0.5
B. subtilis DSM10	4	1
B. thailandensis E264	1	1
K. aerogenes ATCC13048	0.25	1
E. coli ATCC25922	4	2
E. coli MG1655	4	2

3.5.3 Postulated Mechanism of Inhibition

There is clear evidence that the stereochemistry of the CDs influences the anti-microbial properties. Generally, the D-cysCDs required a lower concentration for MIC except for *M. luteus*. While these findings are very interesting and promising, the exact mechanism of anti-microbial activity of the chiral cysCDs requires further investigations. Several studies in the literature point towards production of reactive oxygen species (ROS) causing DNA damage and oxidation of proteins in bacterial cells; however, a peroxide- strip test gave negative results suggesting a different inhibition mechanism.

It could be postulated that the interaction of the cysCDs with the exterior surfaces of the bacteria could result in such variations of MIC. Moreover, L-amino acid is typically a naturally occurring in living systems and as L-cysCDs are synthesized from L-cysteine, it could be that the bacteria was capable of breaking down the CDs. In contrast, the D-cysCDs are synthesized from the unnatural D-cysteine that bacteria are not equipped to digest. Further experiments are needed to confirm the

mechanism of anti-microbial activity in the nanoparticle. A study exploring the interaction of the nanoparticles with the bacteria would provide some of the answers required to understand the mechanism. There is a plethora of functional groups on the surface of the cysCDs that could instigate the bacterial inhibition.

3.6   Investigation into Carbon Dot Formation Mechanism

3.6.1   Determination of Intermediate Species

To glean a deeper understanding of the residual chirality in the nanoparticle and its stereoselective antimicrobial effects, we decided to investigate the formation of the chiral cysCDs using liquid chromatography-mass spectrometry (LC-MS).

In the literature, CDs are suggested to form through a series of condensation, polymerization and carbonization reactions. The reaction of cysteine and citric acid has been previously studied in the literature and is known to form the intermediates like 5-oxo-3,5-dihydro-2H-thiazolo [3,2-a] pyridine-3,7-dicarboxylic acid (TPDCA). But given the conditions of the CD synthesis, multiple reactions can occur, and this results in the formation of many monomer-like species that can combine and cross-link with each other to form polymers.

Our investigation of the origins of chirality in the cysCDs started by analysis of the dialysis waters where unreacted species and intermediates were released outside the dialysis membrane walls. A reverse-phase LC using C8 stationary column and isocratic 90% methanol mobile phase was used to fractionate dialysis water from the cysCD. In such analysis, the polarity of the species decreases with increasing retention time. The LC of the dialysis water of the cysCDs showed prominent peaks at 1.3,3.6, 6.2 and 9.0 mins. The species in the dialysis water could give an indication of the monomeric intermediates that form during the synthesis of the cysCDs. Examining the positions of the peak, cysCDs are composed of mixture of polar and non-polar species.

The MS spectra of dialysis water shows a complex mass fragmentation at each peak. The m/z value of the peaks are approximately around 200-900 and as well as some fragments at an m/z value of 1600 can also be found. The fragments at the large m/z could originate from the CDs that are still intact and the largest fragment was found in the most polar peak of the LC. The smaller m/z population indicates the fragments of the small molecular species that generate the cysCDs and its various properties.
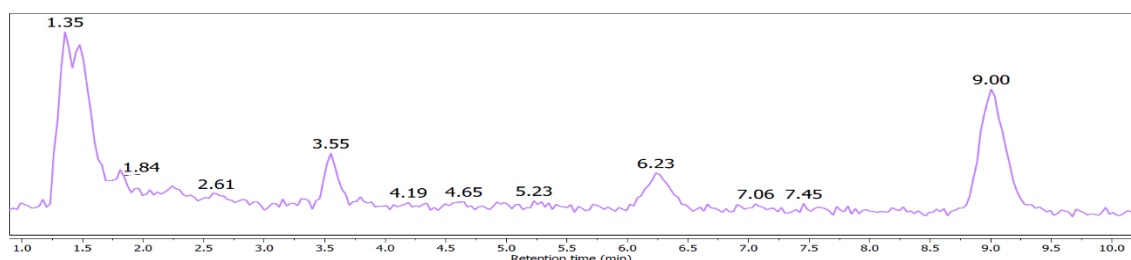
Figure 33. LC spectra of dialysis water of cysCDs using a C8 stationary column and isocratic 90% methanol mobile phase.

By examining the mass fragmentations and the various functional groups present in the cysCDs, an endless range of possible small molecules can be hypothesized. Therefore, also taking into consideration the structure of traditional antibiotics and the various functional groups, the prominent m/z peaks at 215 from the first LC peak could be speculated to be the M^+ ion of 4-Acetamidobenzenesulfonamide, which has a molecular mass of 214.24 gmol^{-1}. 4-Acetamidobenzenesulfonamide is a commercial synthetic antimicrobial that is associated with, sulfonamide or sulfa- drug family. Typically, this class of antibiotics are known to inhibit the bacterial growth and multiplication by competitively inhibiting the enzyme dihydropteroate synthase (DHPS), an enzyme involved in folate synthesis.[137,138]

Therefore, the cysCDs could be composed of moieties similar to antibiotics that belong in the sulfonamide groups. But given the reaction conditions and the CD formation mechanism, the antibiotic properties could also stem from structures in the cysCDs that resemble tetracyclines, cyclic hydrocarbon rings or glycopeptides, amino acids linked to carbohydrate structures.[139–141]

68
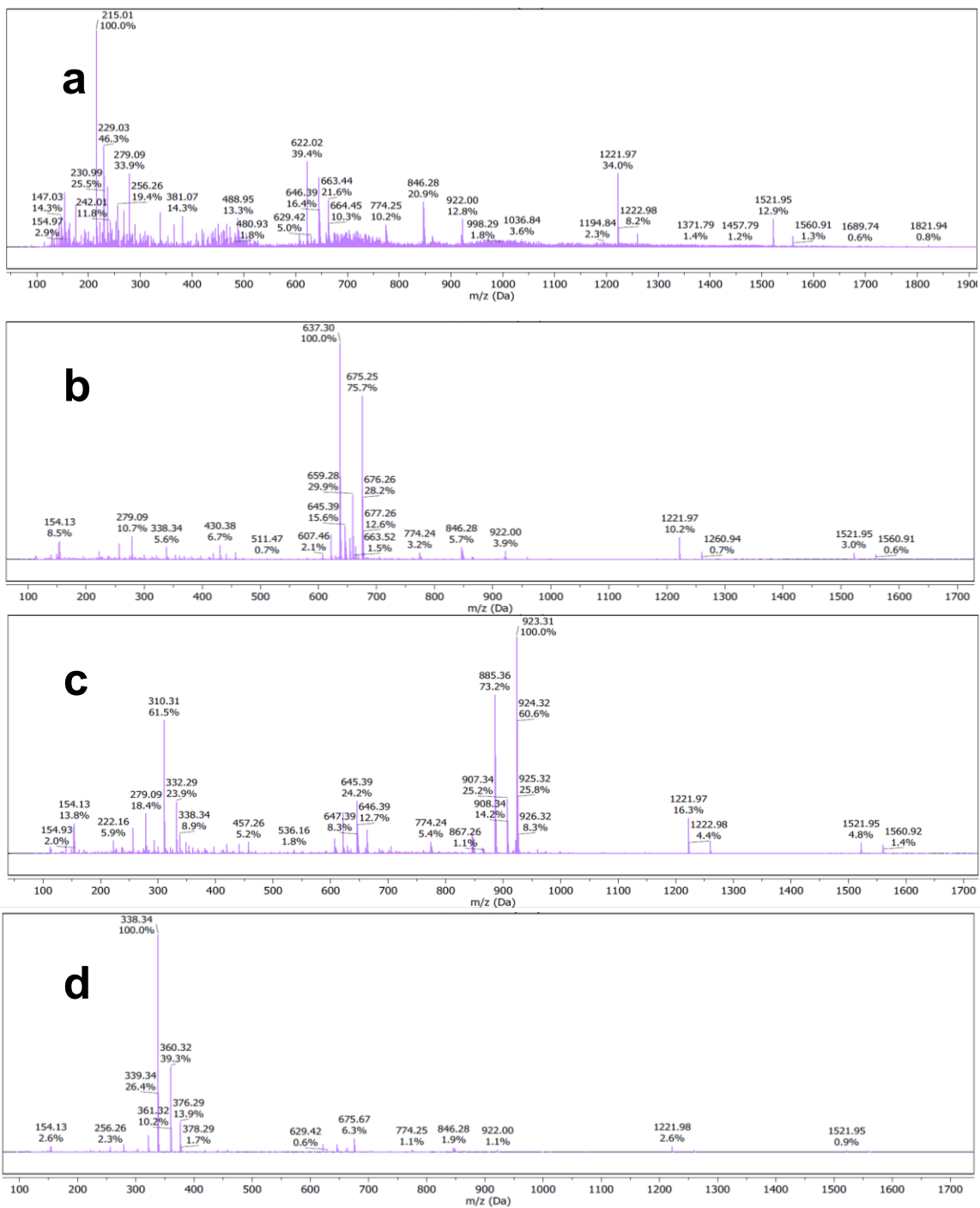
Figure 34. The MS spectra of the LC peaks. The MS of prominent peaks at 1.3(a),3.6(b), 6.2(c) and 9.0(d) mins. The prominent m/z at 215 from the first LC peak (a) could be speculated to be the M⁺ ion of 4-Acetamidobenzenesulfonamide

Chapter 4: Conclusion

4.1   Conclusion

In conclusion, chiral cysCDs were successfully synthesized via a one-step microwave reaction without the need for post synthesis modifications. The cysCDs were synthesized form enantiomers of cysteine and citric acid to induce chirality in the nanoparticle. Through manipulation of reaction parameters such as synthesis temperature, time and precursor ratio, the physical, optical and chiral properties of the cysCDs were tailored.

Reaction temperature had the greatest effect observed on the cysCD properties. With increasing temperature, the cysCDs remained similar in size; however, became more amorphous in nature. The cysCDs also became more conjugated with increasing temperature as reflected by the increasing fluorescence intensity of the cysCDs. Furthermore, the cysCDs showed decrease in chirality as a function of increasing reaction temperature suggesting a greater decomposition of chiral moieties in the CDs to form a more conjugated network in the core of the nanoparticle.

In comparison, minimal changes were observed as a function of reaction time in the cysCD properties. The physical properties and cysCD composition remained similar with changes in the reaction time. The cysCDs increased in fluorescence intensity and decreased in chirality as expected. It could again be postulated that the surface groups and chiral moieties on the cysCDs are decomposed to form a thermodynamically stable and conjugated system.

Furthermore, the cysCD properties were tuned using precursor ratios. The physical properties of the cysCDs remained somewhat stagnant with a change in precursor ratio. Increasing crystallinity was observed as an increase in cysteine ratio to citric acid and as well as increasing fluorescence intensity. The increased doping of heteroatoms available through cysteine helped passivate the surface of the nanoparticle thus enhancing the fluorescence. Furthermore, an increase in the

70

cysteine ratio corresponded to an increase in residual chirality and a decrease in ratio corresponded to a decreased chiral signal as expected. The enantiomers of cysteine produced enantiomeric cysCDs where L-cysteine produced L-cysCDs and D-cysteine produced D-cysCDs as observed by their mirror-image circular dichroism spectra.

A proof of concept application of cysCDs as anti-microbials were also investigated. The cysCDs displayed anti-microbial properties towards an array of gram- positive and gram-negative bacteria. The inhibition of bacterial growth was stereospecific. Typically, the D-cysCDs were able to inhibit growth at a lower concentration in comparison to the L-cysCDs. Further investigation is necessary to identify the mechanism of inhibition. It could be that since the L-cysCDs are made up of L-cysteine which is a naturally occurring amino acid, it is easier to be degraded by the microbials. However, the microbials might be lacking the necessary enzymes and mechanism to degrade the D-cysCDs and as such the stereospecific inhibition of growth.

4.2   Future Works

In order to investigate the origin of chirality, as well as the anti-microbial properties, future studies should focus on understanding the cysCD formation through LC-MS-NMR studies. Studies isolating and characterizing of intermediate species could be essential in understanding the anti-microbial properties of the cysCDs. Isolation of these peaks and analysis by NMR would be needed to elucidate the structures of these fragments. Physical and chemical characterizations on the isolated species such as FT-IR, XPS, circular dichroism and fluorescence spectroscopy would help determine chirality in the system and further verify structural findings. Moreover, circular dichroism studies of the isolated species can also provide insights into stereochemistry of the nanoparticle, how it forms and how it effects the anti-microbial mechanism and whether these factors originate from one or multiple species.

Furthermore, a systematic study of CDs synthesized from all twenty chiral amino acids could also help understand the CD formation mechanism and provide additional insights into their properties. As the twenty amino acids are composed of amine and carboxyl functional groups, only differing in the side chain specific to each amino acid, this study can also provide further insight into the antimicrobial properties of the cysCDs.

Works Cited

1   S. Bayda, M. Adeel, T. Tuccinardi, M. Cordani and F. Rizzolio, *Molecules*, 2019, **25**, 112.

2   National Nanotechnology Initiative, Nano, https://www.nano.gov/.

3   D. Schaming and H. Remita, *Found. Chem.*, 2015, **17**, 187–205.

4   P. I. Dolez, *Nanoengineering*, Elsevier, St-Hyacinthe, QC, Canada, 2015th edn., 2015.

5   R. P. Feynman, *Eng. Sci.*, 1960, **23**, 22–36.

6   N. Taniguchi, *Proc. Int. Conf. Prod. Eng.*, 1974, 18–23.

7   G. Binnig and H. Rohrer, *Surf. Sci.*, 1983, **126**, 236–244.

8   G. Binnig, C. F. Quate and C. Gerber, *Phys. Rev. Lett.*, 1986, **56**, 930–933.

9   N. T. K. Thanh and L. A. W. Green, *Nano Today*, 2010, **5**, 213–230.

10   K. McNamara and S. A. M. Tofail, *Adv. Phys. X*, 2017, **2**, 54–88.

11   K. Kerman, M. Saito, E. Tamiya, S. Yamamura and Y. Takamura, *TrAC Trends Anal. Chem.*, 2008, **27**, 585–592.

12   W.-T. Liu, *J. Biosci. Bioeng.*, 2006, **102**, 1–7.

13   A.-F. Ngomsik, A. Bee, M. Draye, G. Cote and V. Cabuil, *Comptes Rendus Chim.*, 2005, **8**, 963–970.

14   B. F. G. Johnson, *Coord. Chem. Rev.*, 1999, **190–192**, 1269–1285.

15   A. Z. Moshfegh, *J. Phys. D. Appl. Phys.*, 2009, **42**, 233001.

16   B. H. Nguyen and V. H. Nguyen, *Adv. Nat. Sci. Nanosci. Nanotechnol.*, 2016, **7**, 013002.

17   A. Moliton and R. C. Hiorns, *Polym. Int.*, 2004, **53**, 1397–1412.

18   I. Khan, K. Saeed and I. Khan, *Arab. J. Chem.*, 2019, **12**, 908–931.

19   J. Jeevanandam, A. Barhoum, Y. S. Chan, A. Dufresne and M. K. Danquah, *Beilstein J. Nanotechnol.*, 2018, **9**, 1050–1074.

20   M. Loos, in *Carbon Nanotube Reinforced Composites*, Elsevier, 1st edn., 2015, pp. 1–36.

21   X. Huang and M. A. El-Sayed, *J. Adv. Res.*, 2010, **1**, 13–28.

22   M. Shah, *Front. Biosci.*, 2014, **19**, 1320.

23   M. Bloemen, Katholieke Universiteit Leuven, 2015.

24   B. Chertok, B. A. Moffat, A. E. David, F. Yu, C. Bergemann, B. D. Ross and V. C. Yang, *Biomaterials*, 2008, **29**, 487–496.

25   C. Sun, J. Lee and M. Zhang, *Adv. Drug Deliv. Rev.*, 2008, **60**, 1252–1265.

26   B. R. Smith, J. Heverhagen, M. Knopp, P. Schmalbrock, J. Shapiro, M. Shiomi, N. I. Moldovan, M. Ferrari and S. C. Lee, *Biomed. Microdevices*, 2007, **9**, 719–727.

27   K. Hola, Z. Markova, G. Zoppellaro, J. Tucek and R. Zboril, *Biotechnol. Adv.*, 2015, **33**, 1162–1176.

28   T. Neuberger, B. Schöpf, H. Hofmann, M. Hofmann and B. von Rechenberg, *J. Magn. Magn. Mater.*, 2005, **293**, 483–496.

29   L. D. Barron, *Space Sci. Rev.*, 2008, **135**, 187–201.

30   S. Mason, *Trends Pharmacol. Sci.*, 1986, **7**, 20–23.

31   D. Burke and D. J. Henderson, *Br. J. Anaesth.*, 2002, **88**, 563–576.

32   N. Sadgrove and G. Jones, *Agriculture*, 2015, **5**, 48–102.

33   J. Gal, *Nat. Chem.*, 2017, **9**, 604–605.

34   A. W. Schwartz, *Curr. Biol.*, 1994, **4**, 758–760.

35   L. Pasteur, *Ann. Chim. Phys. 3rd Ser.*, 1848, **24**, 442–459.

36   EFSA Scientific Committee, *EFSA J.*, 2014, **12**, 3806.

37   L. A. Nguyen, H. He and C. Pham-Huy, *Int. J. Biomed. Sci.*, 2006, **2**, 85–100.

38   R. Crossley, *Chirality and Biological Activity of Drugs*, Taylor & Francis Inc, Bosa Roca, 1st edn., 1995, vol. 7.

39   Y. Wang, J. Xu, Y. Wang and H. Chen, *Chem. Soc. Rev.*, 2013, **42**, 2930–2962.

40   J. Kumar, K. G. Thomas and L. M. Liz-Marzán, *Chem. Commun.*, 2016, **52**, 12555–12569.

41   Z. Li, L. Shi and Z. Tang, in *Chiral Nanomaterials: Preparation, Properties and Applications*, Wiley-VCH Verlag GmbH & Co. KGaA, Weinheim, Germany, 2017, pp. 1–28.

42   A. J. Mastroianni, S. A. Claridge and A. P. Alivisatos, *J. Am. Chem. Soc.*, 2009, **131**, 8455–8459.

43   A. Kuzyk, R. Schreiber, Z. Fan, G. Pardatscher, E. M. Roller, A. Högele, F. C. Simmel, A. O. Govorov and T. Liedl, *Nature*, 2012, **483**, 311–314.

44   E. D. Sone, E. R. Zubarev and S. I. Stupp, *Angew. Chemie Int. Ed.*, 2002, **41**, 1705–1709.

45   E. D. Sone, E. R. Zubarev and S. I. Stupp, *Small*, 2005, **1**, 694–697.

46   Y. Qiao, Y. Lin, Y. Wang, Z. Yang, J. Liu, J. Zhou, Y. Yan and J. Huang, *Nano Lett.*, 2009, **9**, 4500–4504.

47   F. Gao, S. Ma, X. Xiao, Y. Hu, D. Zhao and Z. He, *Talanta*, 2017, **163**, 102–110.

48   F. P. Milton, J. Govan, M. V. Mukhina and Y. K. Gun'ko, *Nanoscale Horizons*, 2016, **1**, 14–26.

49   M. P. Moloney, J. Govan, A. Loudon, M. Mukhina and Y. K. Gun'ko, *Nat. Protoc.*, 2015, **10**, 558–573.

50   K. Varga, S. Tannir, B. E. Haynie, B. M. Leonard, S. V. Dzyuba, J. Kubelka and M. Balaz, *ACS Nano*, 2017, **11**, 9846–9853.

51   I. Lieberman, G. Shemer, T. Fried, E. M. Kosower and G. Markovich, *Angew. Chemie Int. Ed.*, 2008, **47**, 4855–4857.

52   N. Saifuddin, A. Z. Raziah and A. R. Junizah, *J. Chem.*, 2013, **2013**, 1–18.

53   M. Vázquez-Nakagawa, L. Rodríguez-Pérez, M. A. Herranz and N. Martín, *Chem. Commun.*, 2016, **52**, 665–668.

54   N. Suzuki, Y. Wang, P. Elvati, Z. B. Qu, K. Kim, S. Jiang, E. Baumeister, J. Lee, B. Yeom, J. H. Bahng, J. Lee, A. Violi and N. A. Kotov, *ACS Nano*, 2016, **10**, 1744–1755.

55   F. Askari, A. Rahdar and J. F. Trant, *Sens. Bio-Sensing Res.*, 2019, **22**, 100251.

56   Y. Yu, W. Liu, J. Ma, Y. Tao, Y. Qin and Y. Kong, *RSC Adv.*, 2016, **6**, 84127–84132.

57   Y. Wei, L. Chen, J. Wang, X. Liu, Y. Yang and S. Yu, *RSC Adv.*, 2019, **9**, 3208–3214.

58   L. Đorđević, F. Arcudi, A. D'Urso, M. Cacioppo, N. Micali, T. Bürgi, R. Purrello and M. Prato, *Nat. Commun.*, 2018, **9**, 3442.

59   A. Ghosh, B. Parasar, T. Bhattacharyya and J. Dash, *Chem. Commun.*, 2016, **52**, 11159–11162.

60   F. Li, Y. Li, X. Yang, X. Han, Y. Jiao, T. Wei, D. Yang, H. Xu and G. Nie, *Angew. Chemie - Int. Ed.*, 2018, **57**, 2377–2382.

61   Y. Zhang, L. Hu, Y. Sun, C. Zhu, R. Li, N. Liu, H. Huang, Y. Liu, C. Huang and Z. Kang, *RSC Adv.*, 2016, **6**, 59956–59960.

62   M. J. Deka and D. Chowdhury, *RSC Adv.*, 2017, **7**, 53057–53063.

63   L. Hu, H. Li, C. Liu, Y. Song, M. Zhang, H. Huang, Y. Liu and Z. Kang, *Nanoscale*, 2018, **10**, 2333–2340.

64   M. Zhang, L. Hu, H. Wang, Y. Song, Y. Liu, H. Li, M. Shao, H. Huang and Z.

Kang, *Nanoscale*, 2018, **10**, 12734–12742.

65   X. Xu, R. Ray, Y. Gu, H. J. Ploehn, L. Gearheart, K. Raker and W. A. Scrivens, *J. Am. Chem. Soc.*, 2004, **126**, 12736–12737.

66   Y. P. Sun, B. Zhou, Y. Lin, W. Wang, K. A. S. Fernando, P. Pathak, M. J. Meziani, B. A. Harruff, X. Wang, H. Wang, P. G. Luo, H. Yang, M. E. Kose, B. Chen, L. M. Veca and S. Y. Xie, *J. Am. Chem. Soc.*, 2006, **128**, 7756–7757.

67   B. Zhi, X. X. Yao, Y. Cui, G. Orr and C. L. Haynes, *Nanoscale*, 2019, **11**, 20411–20428.

68   T. V. De Medeiros, J. Manioudakis, F. Noun, J. R. Macairan, F. Victoria and R. Naccache, *J. Mater. Chem. C*, 2019, **7**, 7175–7195.

69   S. Y. Lim, W. Shen and Z. Gao, *Chem. Soc. Rev.*, 2015, **44**, 362–381.

70   F. Yan, Z. Sun, H. Zhang, X. Sun, Y. Jiang and Z. Bai, *Microchim. Acta*, 2019, **186**, 1–37.

71   H. Xu, L. Xie and M. Hakkarainen, *ACS Sustain. Chem. Eng.*, 2017, **5**, 5360–5367.

72   P. Roy, P. C. Chen, A. P. Periasamy, Y. N. Chen and H. T. Chang, *Mater. Today*, 2015, **18**, 447–458.

73   V. A. Ansi and N. K. Renuka, *Sensors Actuators, B Chem.*, 2018, **264**, 67–75.

74   S. Cailotto, E. Amadio, M. Facchin, M. Selva, E. Pontoglio, F. Rizzolio, P. Riello, G. Toffoli, A. Benedetti and A. Perosa, *ACS Med. Chem. Lett.*, 2018, **9**, 832–837.

75   S. Paikaray and P. Moharana, National Institute of Technology, 2013.

76   S. S. Monte-Filho, S. I. E. Andrade, M. B. Lima and M. C. U. Araujo, *J. Pharm. Anal.*, 2019, **9**, 209–216.

77   S. Sahu, B. Behera, T. K. Maiti and S. Mohapatra, *Chem. Commun.*, 2012, **48**, 8835.

78   A. Kumar and M. Khandelwal, *New J. Chem.*, 2014, **38**, 3457–3467.

79   P. Karfa, E. Roy, S. Patra, S. Kumar, A. Tarafdar, R. Madhuri and P. K. Sharma, *RSC Adv.*, 2015, **5**, 58141–58153.

80   W. Kwon, S. Do and S.-W. Rhee, *RSC Adv.*, 2012, **2**, 11223.

81   H. Peng and J. Travas-Sejdic, *Chem. Mater.*, 2009, **21**, 5563–5565.

82   J. Manioudakis, F. Victoria, C. A. Thompson, L. Brown, M. Movsum, R. Lucifero and R. Naccache, *J. Mater. Chem. C*, 2019, **7**, 853–862.

83   A. Sciortino, A. Cannizzo and F. Messina, *C*, 2018, **4**, 67.

84   X. Sun and Y. Lei, *TrAC - Trends Anal. Chem.*, 2017, **89**, 163–180.

85   R. Das, R. Bandyopadhyay and P. Pramanik, *Mater. Today Chem.*, 2018, **8**, 96–109.

86   R. K. Singh, R. Kumar, D. P. Singh, R. Savu and S. A. Moshkalev, *Mater. Today Chem.*, 2019, **12**, 282–314.

87   S. Y. Lim, W. Shen and Z. Gao, *Chem. Soc. Rev.*, 2015, **44**, 362–381.

88   J. A. Jaleel and K. Pramod, *J. Control. Release*, 2018, **269**, 302–321.

89   A. Zhao, Z. Chen, C. Zhao, N. Gao, J. Ren and X. Qu, *Carbon N. Y.*, 2015, **85**, 309–327.

90   V. Mishra, A. Patil, S. Thakur and P. Kesharwani, *Drug Discov. Today*, 2018, **23**, 1219–1232.

91   M. Thakur, S. Pandey, A. Mewada, V. Patil, M. Khade, E. Goshi and M. Sharon, *J. Drug Deliv.*, 2014, **2014**, 1–9.

92   J.-R. Macairan, D. B. Jaunky, A. Piekny and R. Naccache, *Nanoscale Adv.*, 2019, **1**, 105–113.

93   L. Li, R. Zhang, C. Lu, J. Sun, L. Wang, B. Qu, T. Li, Y. Liu and S. Li, *J. Mater. Chem. B*, 2017, **5**, 7328–7334.

94   Y. Li, G. Bai, S. Zeng and J. Hao, *ACS Appl. Mater. Interfaces*, 2019, **11**,

4737–4744.

95   T. Kong, L. Hao, Y. Wei, X. Cai and B. Zhu, *Cell Prolif.*, 2018, **51**, e12488.

96   J. Zhang, H. Zhang, J. Jiang, N. Cui, X. Xue, T. Wang, X. Wang, Y. He and D. Wang, *Int. J. Nanomedicine*, 2020, **Volume 15**, 433–444.

97   Q. Zeng, D. Shao, X. He, Z. Ren, W. Ji, C. Shan, S. Qu, J. Li, L. Chen and Q. Li, *J. Mater. Chem. B*, 2016, **4**, 5119–5126.

98   S. Zhu, Y. Song, X. Zhao, J. Shao, J. Zhang and B. Yang, *Nano Res.*, 2015, **8**, 355–381.

99   C. Xia, S. Zhu, T. Feng, M. Yang and B. Yang, *Adv. Sci.*, 2019, **6**, 1901316.

100   Z. Liu, H. Zou, N. Wang, T. Yang, Z. Peng, J. Wang, N. Li and C. Huang, *Sci. China Chem.*, 2018, **61**, 490–496.

101   X. Li, S. Zhang, S. A. Kulinich, Y. Liu and H. Zeng, *Sci. Rep.*, 2015, **4**, 4976.

102   Edinburgh Instruments, Edinburgh Instruments, https://www.edinst.com/blog/colloidal-quantum-dots/.

103   Z.-H. Wen and X.-B. Yin, *RSC Adv.*, 2016, **6**, 27829–27835.

104   Z. C. Jiang, T. N. Lin, H. T. Lin, M. J. Talite, T. T. Tzeng, C. L. Hsu, K. P. Chiu, C. A. J. Lin, J. L. Shen and C. T. Yuan, *Sci. Rep.*, 2016, **6**, 19991.

105   J. Yu, C. Liu, K. Yuan, Z. Lu, Y. Cheng, L. Li, X. Zhang, P. Jin, F. Meng and H. Liu, *Nanomaterials*, 2018, **8**, 233.

106   Y.-P. Sun, B. Zhou, Y. Lin, W. Wang, K. A. S. Fernando, P. Pathak, M. J. Meziani, B. A. Harruff, X. Wang, H. Wang, P. G. Luo, H. Yang, M. E. Kose, B. Chen, L. M. Veca and S.-Y. Xie, *J. Am. Chem. Soc.*, 2006, **128**, 7756–7757.

107   Y. Suda, T. Ono, M. Akazawa, Y. Sakai, J. Tsujino and N. Homma, *Thin Solid Films*, 2002, **415**, 15–20.

108   S. Hu, J. Liu, J. Yang, Y. Wang and S. Cao, *J. Nanoparticle Res.*, 2011, **13**, 7247–7252.

109 L. Bao, Z.-L. Zhang, Z.-Q. Tian, L. Zhang, C. Liu, Y. Lin, B. Qi and D.-W. Pang, *Adv. Mater.*, 2011, **23**, 5801–5806.

110 H. Li, X. He, Z. Kang, H. Huang, Y. Liu, J. Liu, S. Lian, C. H. A. Tsang, X. Yang and S. T. Lee, *Angew. Chemie - Int. Ed.*, 2010, **49**, 4430–4434.

111 Q. Liang, W. Ma, Y. Shi, Z. Li and X. Yang, *Carbon N. Y.*, 2013, **60**, 421–428.

112 H. He, X. Wang, Z. Feng, T. Cheng, X. Sun, Y. Sun, Y. Xia, S. Wang, J. Wang and X. Zhang, *J. Mater. Chem. B*, 2015, **3**, 4786–4789.

113 T. N. J. I. Edison, R. Atchudan, M. G. Sethuraman, J. J. Shim and Y. R. Lee, *J. Photochem. Photobiol. B Biol.*, 2016, **161**, 154–161.

114 Z. Ma, H. Ming, H. Huang, Y. Liu and Z. Kang, *New J. Chem.*, 2012, **36**, 861.

115 Y. Wu, Y. Liu, J. Yin, H. Li and J. Huang, *Talanta*, 2019, **205**, 120121.

116 L. Shi, J. H. Yang, H. B. Zeng, Y. M. Chen, S. C. Yang, C. Wu, H. Zeng, O. Yoshihito and Q. Zhang, *Nanoscale*, 2016, **8**, 14374–14378.

117 Y. Song, S. Zhu, S. Zhang, Y. Fu, L. Wang, X. Zhao and B. Yang, *J. Mater. Chem. C*, 2015, **3**, 5976–5984.

118 M. J. Krysmann, A. Kelarakis, P. Dallas and E. P. Giannelis, *J. Am. Chem. Soc.*, 2012, **134**, 747–750.

119 D. Qu and Z. Sun, *Mater. Chem. Front.*, 2020, **4**, 400–420.

120 CLSI, in *Performance Standards for Antimicrobial Susceptibility Testin*, Clinical and Laboratory Standard Institute, Wayne, PA, 29th edn., 2019.

121 CLSI, in *Methods for Dilution Antimicrobial Susceptibility Tests for Bacteria That Grow Aerobically.*, Clinical and Laboratory Standard Institute, Wayne, PA, 11th edn., 2018.

122 HSDB, *Int. Progr. Chem. Safety/Commission Eur. Union*.

123 V. A. Yablokov, Y. A. Vasina, I. A. Zelyaev and S. V. Mitrofanova, *Russ. J. Gen. Chem.*, 2009, **79**, 1141–1145.

124 J. Wang, S. Su, J. Wei, R. Bahgi, L. Hope-Weeks, J. Qiu and S. Wang, *Phys. E Low-dimensional Syst. Nanostructures*, 2015, **72**, 17–24.

125 Q. Fang, Y. Dong, Y. Chen, C.-H. Lu, Y. Chi, H.-H. Yang and T. Yu, *Carbon N. Y.*, 2017, **118**, 319–326.

126 C. G. Pope, *J. Chem. Educ.*, 1997, **74**, 129.

127 J. Dore, A. Burian and S. Tomita, *Acta Phys. Pol. A*, 2000, **98**, 495–504.

128 T. Wang, L. Wang, D. Wu, W. Xia, H. Zhao and D. Jia, *J. Mater. Chem. A*, 2014, **2**, 8352–8361.

129 N. Li, Z. Wang and Z. Shi, in *Physics and Applications of Graphene - Experiments*, ed. S. Mikhailov, InTech, Peking, 2011, pp. 1–540.

130 C. Merlic and B. Fam, Introduction to IR Spectra, https://webspectra.chem.ucla.edu//irintro.html.

131 H. Konno, in *Materials Science and Engineering of Carbon*, Elsevier, 2016, pp. 153–171.

132 N. Sahiner, S. S. Suner, M. Sahiner and C. Silan, *J. Fluoresc.*, 2019, **29**, 1191–1200.

133 L. Li, X. Yao, H. Li, Z. Liu, W. Ma and X. Liang, *J. Chem. Eng. JAPAN*, 2014, **47**, 21–27.

134 Z. Lin, M. K. Song, Y. Ding, Y. Liu, M. Liu and C. P. Wong, *Phys. Chem. Chem. Phys.*, 2012, **14**, 3381–3387.

135 S. S. Zhang, *Energies*, 2014, **7**, 4588–4600.

136 X. Wang, Y. Qian, L. Wang, H. Yang, H. Li, Y. Zhao and T. Liu, *Adv. Funct. Mater.*, 2019, **29**, 1902929.

137 M. Madigan, J. Martinko, D. Stahl and D. Clark, *Brock Biology of Microorganisms*, Pearson Education, 13th edn., 2012.

138 R. J. Henry, *Bacteriol. Rev.*, 1943, **7**, 175–262.

139 S. M. Reeve, M. N. Lombardo and A. C. Anderson, *Future Microbiol.*, 2015,

10, 1727–33.

140   K. Bush, *Curr. Opin. Pharmacol.*, 2012, **12**, 527–534.

141   A. H. A. M. van Hoek, D. Mevius, B. Guerra, P. Mullany, A. P. Roberts and
       H. J. M. Aarts, *Front. Microbiol.*, 2011, **2**, 1–27.
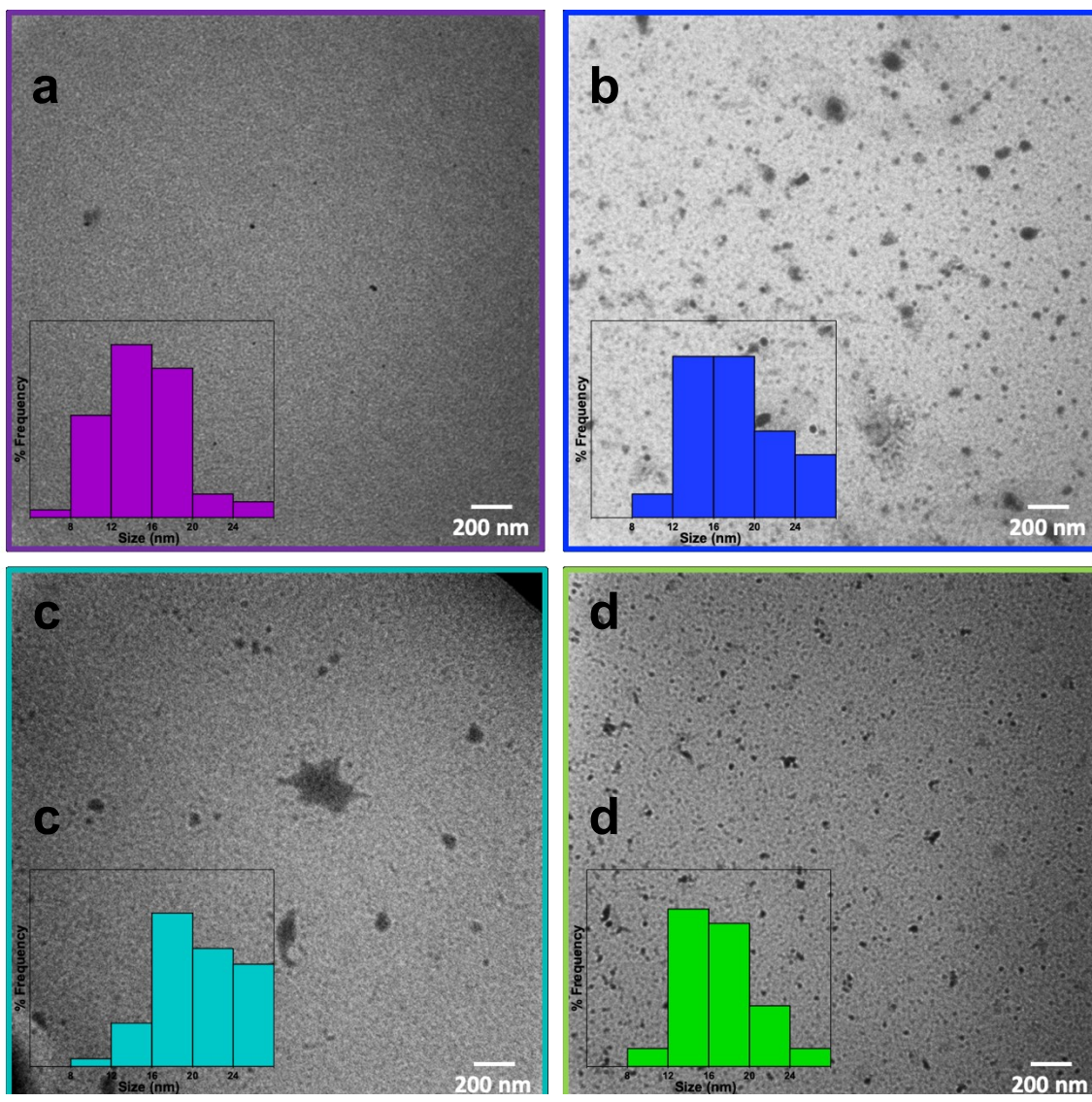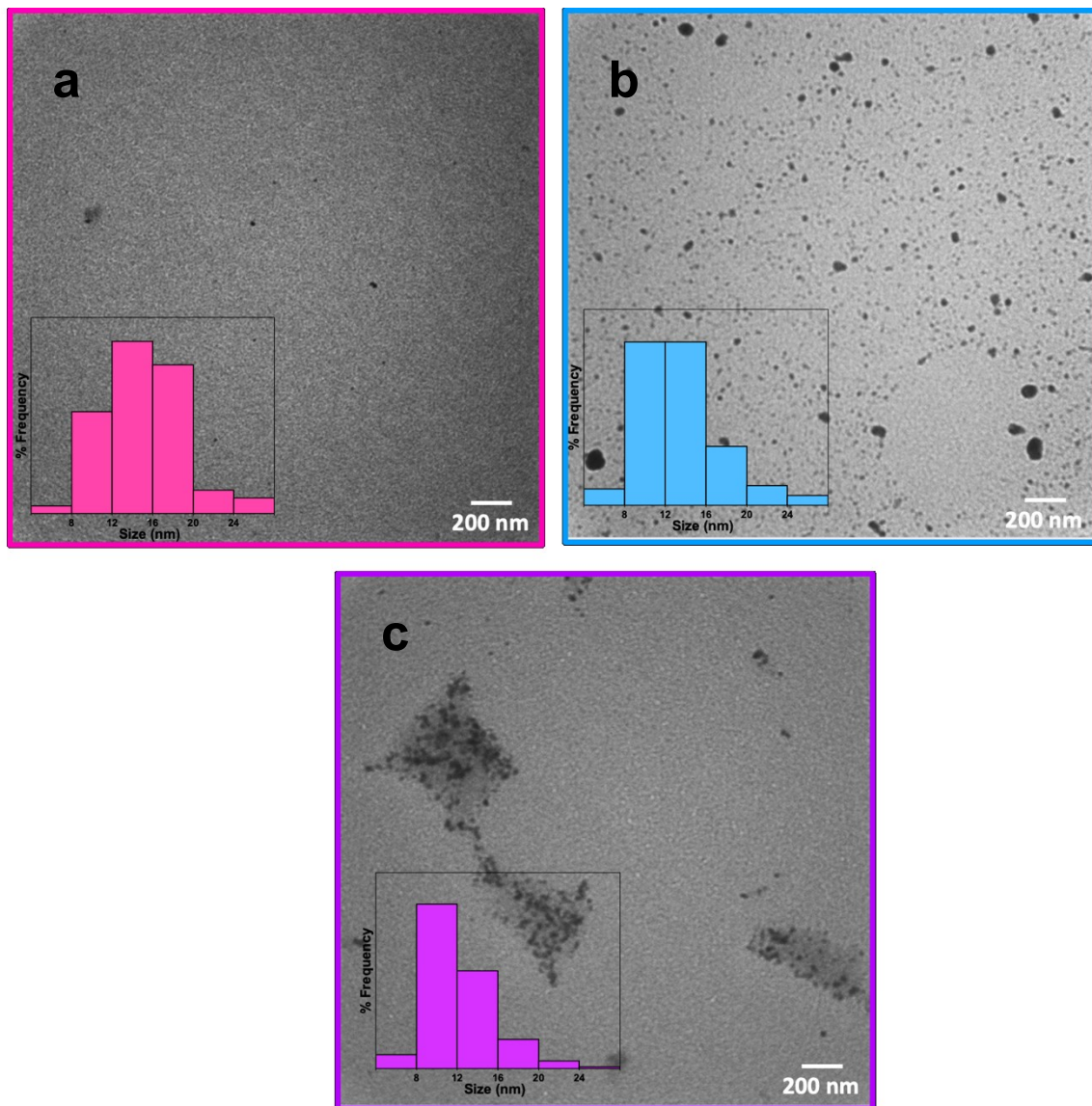
Appendix

Figure A 1. TEM images of cysCDs at different reaction temperatures. TEM images of cysCDs synthesized at 5mins and different reaction temperature at 160 °C (a), 180 °C (b), 200 °C (c),and 220 °C (d). The cysCDs seem to slightly increase in size as a function of synthesis temperature.

Figure A 2. TEM images of cysCDs at different reaction times. TEM images of cysCDs synthesized at 160 °C and different reaction times at 5 mins (a), 10 mins (b),and 15 mins (c).The cysCDs seem to slightly increase in size as a function of synthesis time.
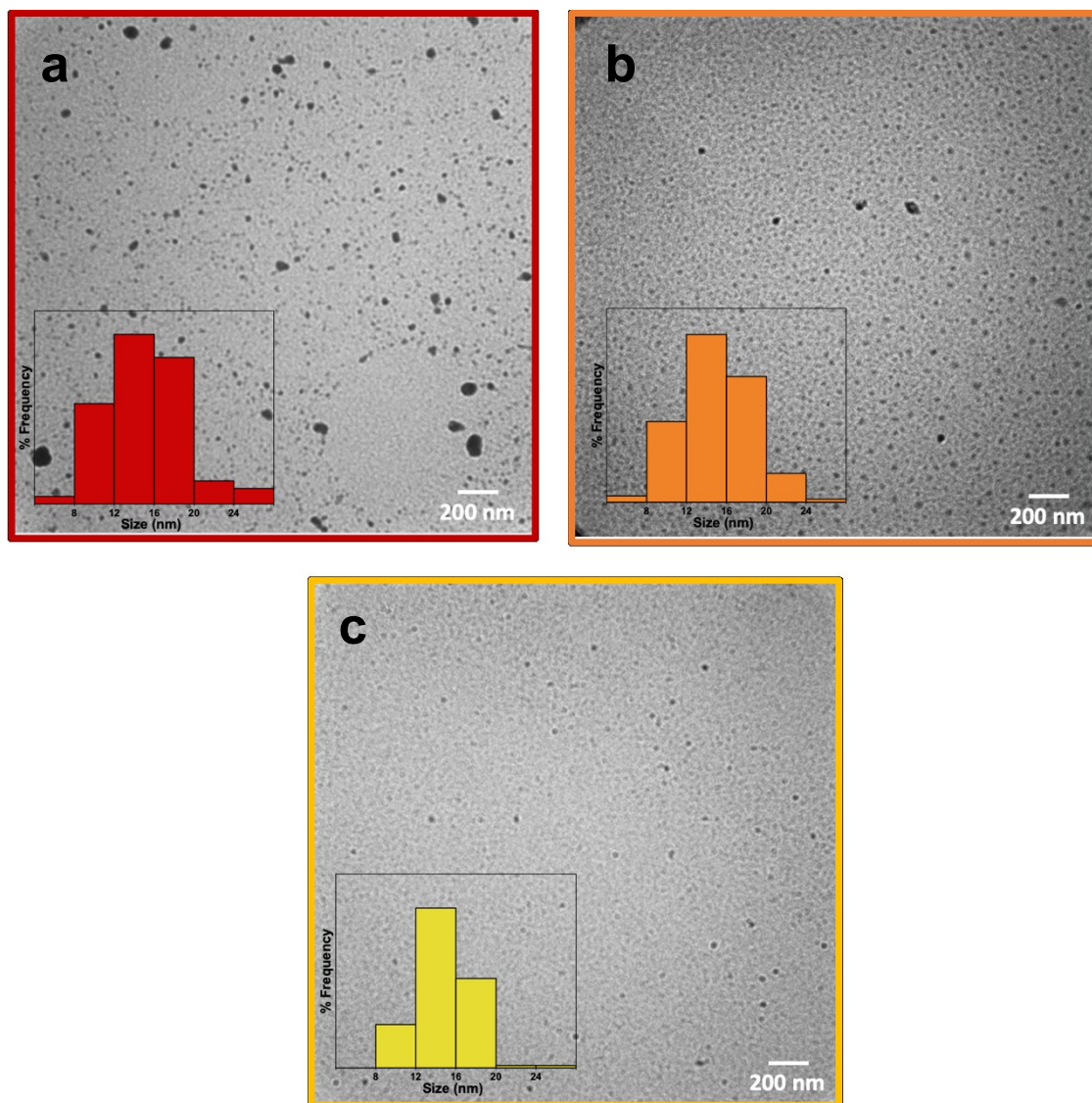
Figure A 3. TEM images of L-cysCDs at different precursor ratios. TEM images of cysCDs synthesized at 160 °C and 5 mins with 1 L-CYS : 1 CA ratio(a), 1 L-CYS : 2 CA ratio (b),and 2 L-CYS : 1 CA ratio (c).The cysCDs seem to be stagnant in size as a function of reaction precursor.
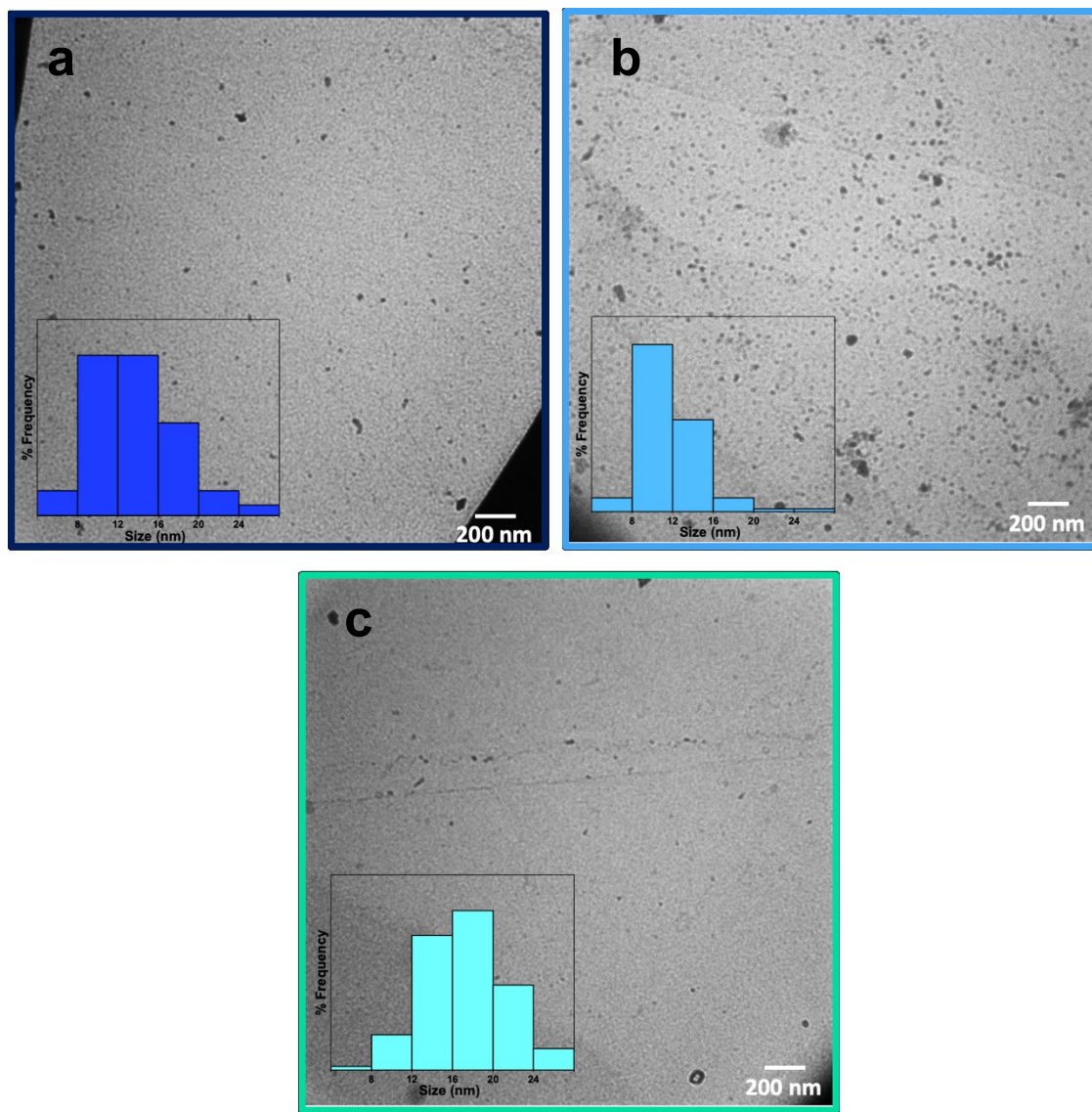
Figure A 4. TEM images of D-cysCDs at different precursor ratios. TEM images of cysCDs synthesized at 160 °C and 5 mins with 1 D-CYS : 1 CA ratio(a), 1 D-CYS : 2 CA ratio (b),and 2 D-CYS : 1 CA ratio (c).The cysCDs seem to be stagnant in size as a function of reaction precursor.
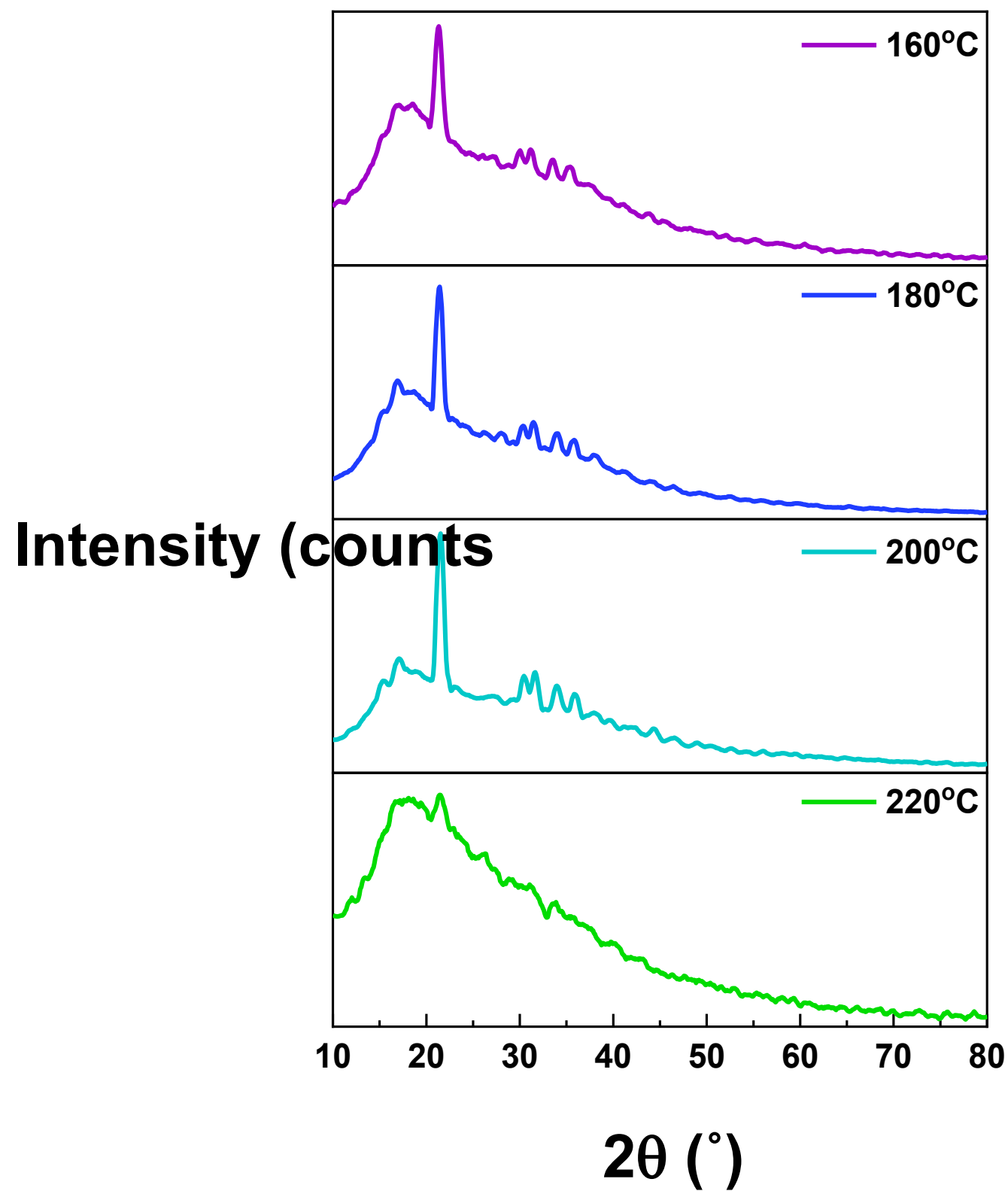
Figure A 5. XRD spectra of the cysCDs as a function of synthesis temperature. An increasing temperature results in a decrease in crystallinity of the nanoparticle as observed by the loss of the sharp peaks.
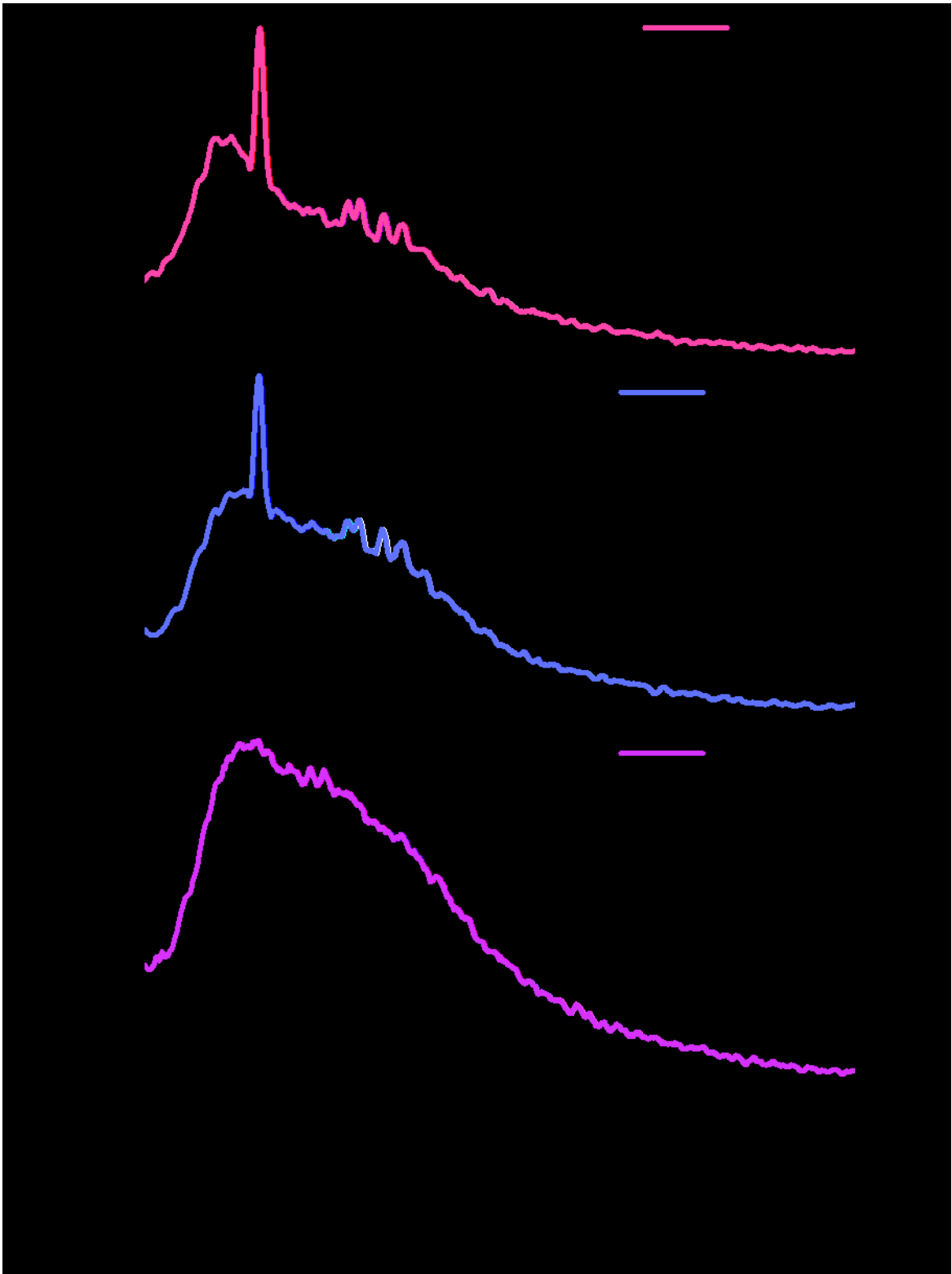
Figure A 6. XRD spectra of the cysCDs as a function of synthesis time. An increasing reaction time results in a decrease in crystallinity of the nanoparticle.
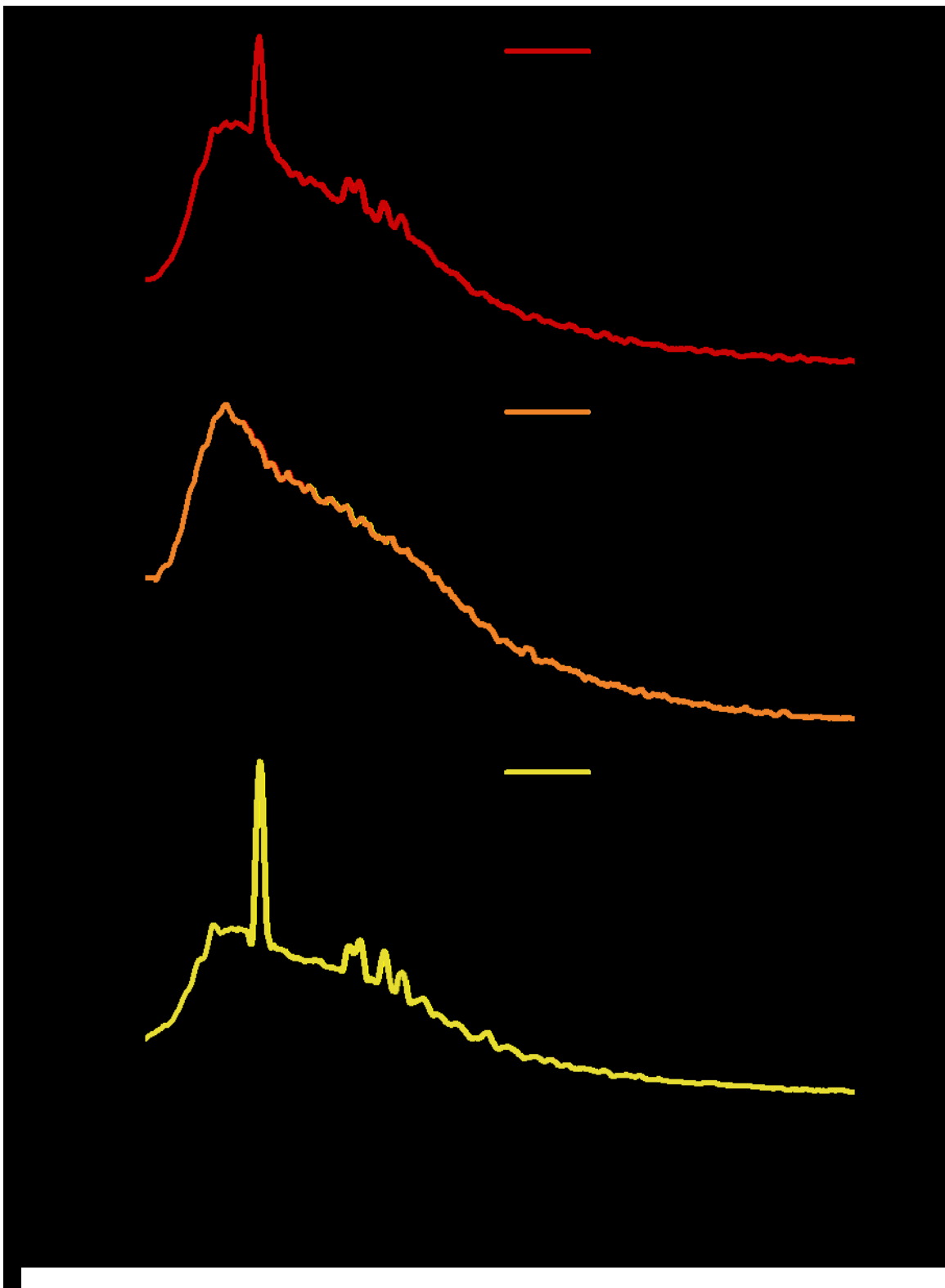
.

Figure A 7. XRD spectra of the cysCDs as a function of precursor ratios. An increasing cysteine to citric acid ratio results in an increase in crystallinity of the nanoparticle. The greater concentration of cysteine enhances the formation of ordered structure in the cysCDs.